Université de Liège
Faculté des Sciences Appliquées

von Karman Institute for Fluid Dynamics
Aeronautics/Aerospace Department

Sensitivity Analysis and Uncertainty Quantification of Plasma Jet Instabilities in the VKI Plasmatron

---

Master thesis presented by Joffrey Coheur
in order to obtain the degree of master in *Ingénieur Civil Physicien*,
Université de Liège (ULg), academic year 2014-2015.

Supervisors:

Prof. T. Magin (VKI)
Prof. M. Arnst (ULg)

Acknowledgements

First of all, I would like to express my gratitude to my advisors, who always have supported me during this project. I would like to thanks Prof. T. Magin for giving me the opportunity of working on this fascinating topic and without who all this work would not have been possible. Thank you for your wise advices during the elaboration of this thesis. Your work is a great source of inspiration for me. I would like to thanks Prof. M. Arnst for his great advices on all aspects of this project and for his continuous follow-up. I'm very grateful for the numerous hours he spent for me from the very beginning of this project.

I would like to thanks Dr. Fabio Pinna for always being present, who always accepted to receive me at any time in VKI and for his help for mastering all the tools necessary for this project. Your interest in the project has always gave me the motivation for going further.

I would like to thanks all the people who contributed to this thesis and who helped me in the achievement of this work. There are too many people to mention here but I would like to thanks particularly Zuheyr Alsalihi for his help on the CFD part and the time he spent for me.

This master thesis is an achievement for the five years I spent at the *Université de Liège*. I would like to thanks all my friends that have been present during these years. In particular, I would like to thanks F. Renzoni and G. Simonis for their thorough re-reading of the present work.

Of course, all my gratitude is addressed to my family, for always supporting me in every moments.

Contents

List of Figures

List of Tables

List of Symbols

Acronyms

CLT	Central Limit Theorem
CPG	Calorically Perfect Gas
CRG	Chemically Reacting mixture of perfect Gas
HSC	High-Speed Camera
ICP	Inductively-Coupled Plasma
LHTS	Local Heat Transfer Simulation
LLN	Law of Large Number
LST	Linear Stability Theory
LTE	Local Thermodynamic Equilibrium
MC	Monte Carlo
QoI	Quantity of Interest
SC	Stochastic Collocation
TPM	Thermal Protection Material
TPS	Thermal Protection System
UQ	Uncertainty Quantification
VESTA	VKI Extensible Stability and Transition Analysis
VKI	von Karman Institute

Roman Symbols

c_p	Specific heat at constant pressure	J kg^{-1} K^{-1}
c_v	Specific heat at constant volume	J kg^{-1} K^{-1}
f	Wave frequency	Hz
f_i	Velocity distribution function of species i	m^6 s^{-3}
f_i^M	Maxwellian velocity distribution function of species i	m^6 s^{-3}
k	Thermal conductivity	W m^{-1} K^{-1}
k_B	Boltzmann's constant	J K^{-1}
m	Radial mode number	-
$\dot{m}$	Injected gas mass flow rate	g s^{-1}
M	Mach number	
M^r_{cl}	Relative Mach number for the centerline jet value	-
M^r_{cl}	Relative Mach number for the ambient stream	-
$\mathscr{M}$	Mixture molar weight	kg
N_A	Avogadro's number	-
n^S	Number of species in the mixture	-
p_{tc}	Static pressure in the test chamber	Pa
P_{el}	Power provided by the high-frequency generator	W
P_{fl}	Power transmitted to the plasma flow	W
q	Azimuthal wavenumber	-
$\mathcal{R}$	Universal gas constant	J K^{-1}
S	Sutherland's temperature	K

T	LTE temperature	K
$\boldsymbol{u}$	Hydrodynamic velocity	m s^{1}
u	Radial velocity component	m s^{-1}
v	Azimuthal velocity component	m s^{-1}
w	Streamwise velocity component	m s^{-1}

Greek Symbols

α	Complex streamwise wavenumber	-
$\alpha_{\mathcal{I}}$	Growth rate	-
$\alpha_{\mathcal{R}}$	Real streamwise wavenumber	-
$\alpha_{\mathcal{I}}^{\hat{\varphi}}$	Growth rate of the flow model $\hat{\varphi}$	-
γ	Specific heat ratio	-
ζ	Compressibility factor	-
η	Power efficiency parameter	-
λ	Second viscosity coefficient	kg m^{-1} s^{-1}
μ	Dynamic viscosity	kg m^{-1} s^{-1}
ρ	Density	kg m^{-3}
ψ_i^l	Boltzmann's collisional invariant l of species i	
ω	Adimensional angular frequency	-

Mathematical Notation and Operators

$\mathcal{D}_i(\cdot)$	Boltzmann's streaming operator of species i
$\mathcal{J}_i$	Boltzmann's scattering collision operator of species i
$\hat{\varphi}$	Model considering one set of flow properties
$\hat{\chi}$	Set of the basic model considering different flow properties

Subscripts

cl	Centerline value
$\mathcal{I}$	Imaginary part
$\mathcal{R}$	Real part
0	Sea-level reference value
∞	Freestream value

Table of Physical Constants

Quantity	Symbol	Value	Unit
Air specific gas constant at sea-level	R_0	287	[J / (kg $\cdot$ K)]
Avogadro's number	N_A	$6.022\ 10^{23}$	[part. / mol]
Boltzmann's constant	k_B	$1.38\ 10^{-23}$	[J / K]
Universal gas constant	$\mathcal{R}$	8.314	[J / (mol $\cdot$ K)]

Table 2: Table of useful physical constants.

Chapter 1

Introduction

1.1 Motivation

During the atmospheric reentry phase, space vehicles enter the atmosphere at hypersonic speeds and a strong bow shock wave is formed in front of the vehicle (Fig. 1.1a). At the interface of the shock, the air is strongly compressed and the massive amount of the flow kinetic energy is converted into internal energy of the gas. Very high temperatures are reached in the shock layer and causing molecules to reach excited states and for sufficiently high temperatures, gas to be ionized. At the nose of the vehicle, a stagnation point exists with a surrounding subsonic region. The heat flux from this subsonic boundary layer to the space vehicle reaches a maximum, and efficient Thermal Protection Systems (TPS) need to be developed for the integrity of the space vehicle and the crew survival. For this reason, the design of TPS is one of the most important challenge in the conception of spacecraft. In Fig. 1.1 an example of a real flight test on thermal protection systems, recently conducted by the ESA[1] is shown. This test was representative of low Earth orbit atmosphere.

(a) Representation of the reentry phase.

(b) IXV after reentry phase.

Figure 1.1: ESA Intermediate eXperimental Vehicle.

1.2 Ground-based facilities

However, real flight tests are seldom feasible and ground-based facilities are needed in order to reproduce the thermal conditions characterizing reentries. Ground-based facilities are therefore well-suited for the reproducibility of real flight experiments and allow the Thermal Protection Materials (TPMs) to be tested at a lower cost. In particular, the

---

[1] European Space Agency

properties of TPMs are determined in plasma wind tunnels, based on a Local Heat Transfer Simulation (LHTS) methodology [18]. Experimental reproducibility of the heat transfer to the stagnation point is achieved, ensuring similarity between enthalpy (or temperature), pressure and velocity gradient along the body wall at the outer edge of the boundary layer. Plasma wind tunnels reproduce such high subsonic enthalpy flows.

In the past, more interest was given to arc-jet and induction-type plasma wind tunnels. Arc jets were usually preferred for qualification testing of large-scale samples at very high heat flux, thanks to their high-power capabilities. However, all arc-driven facilities are polluted by electrode erosion which results in a flow slightly seeded with electrode particles (usually copper). These particles are then deposited in the sample being tested and the catalytic properties of the TPMs are modified in the process.

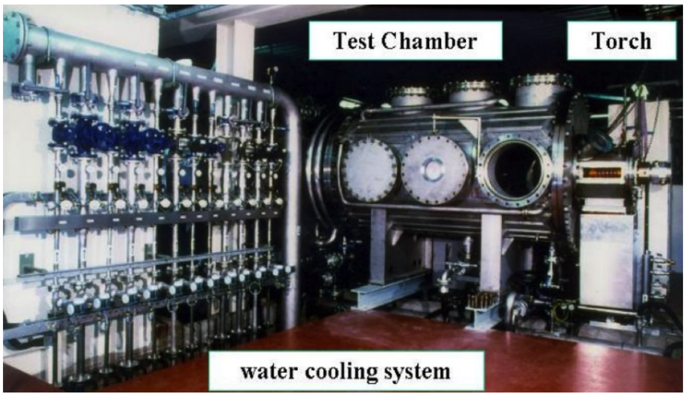

Figure 1.2: Plasmatron 1.2 [MW] facility.

In contrast, plasma facilities using electrodeless technology for the plasma discharge generation ensure a superior flow purity. Therefore, they are usually more dedicated to the study of aerothermochemistry and gas-surface interaction phenomena. In the end of the 20th century, no ICP (Inductively-Coupled Plasma) facility of high power was available in Europe to satisfy those needs. This fact led towards the end of 1994 to the fabrication and assembly of the 1.2 [MW] Plasmatron at the VKI[2] (Fig. 1.2). This facility is, at the present time, the most powerful of its kind in the world. The VKI Plasmatron is usually operated at the subsonic regime, from which the complete reproducibility of the actual flight conditions is achieved locally, at the stagnation point [8].

1.3 Instabilities Phenomena Experienced in Ground-Based Facilities

Although the plasma generated in the Plasmatron appears temporally stable and axisymmetric for naked-eye observations, it is known that jets usually undergo instability phenomena. In the case of the plasma jet, these unstable features must be investigated for a correct characterization of the testing thermal protection material.

In the past, it was possible to investigate the fluctuation features of the plasma jet by means of High-Speed Camera (HSC) imaging (Fig. 1.3). Experimental results from Benito *et al.* highlighted that the supplied electrical power P_{el} and the test chamber static pressure p_{tc} were the main driving parameters of the unsteady phenomena occurring in the flow [4]. Following this, Cipullo *et al.* went further in the analysis and investigated the results provided from the HSC device in the frequency domain and related them in the spatial domain [8]. In this work, a large test campaign in the VKI Plasmatron was performed, with parameters P_{el} and p_{tc} respectively varying from 120 to 300 [kW] and from 1500 to 20000 [Pa], and mass flow rate $\dot{m}$ fixed to 16 [g/s]. It appeared that the

---

[2] It was inaugurated on December 8, 1997.

instabilities were attributed to the supplied voltage at 600 [Hz] (network power supply after being rectified by a 12-pulses bridge rectifier) and its strongest harmonics. They were not observable when p_{tc} was increased. However, instabilities at 50 [Hz] (the network power supply) and its harmonics were also observed. Conversely, as p_{tc} was increased, the 50 [Hz] component significantly increased. Finally, one large component at 900 [Hz] was also observed. The power stored in this mode was mainly located in the freestream of the jet.

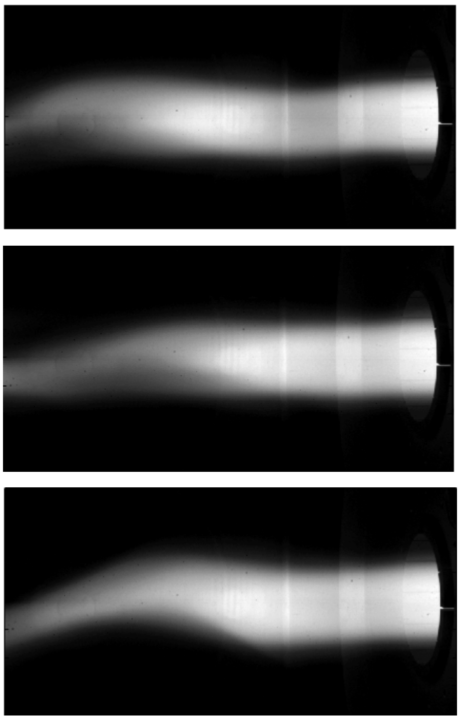

Figure 1.3: Unsteady features of the plasma jet measured by the high-speed camera. The high frequency acquisition by the HSC of light emission allows to get a qualitative picture of the unsteady heat and mass transfers occurring in the plasma flow [8]. The streamwise direction of the jet is from right to left.

1.4 Numerical Study of Plasma Jet Instabilities

Following the design of the Plasmatron, a numerical approach for the characterisation of thermal protection materials was developed as well. A numerical model for inductive plasma wind tunnels was implemented and integrated to a numerical solver CooLFluiD[3] both developed in the VKI [25]. The numerical model is used to provide the mean flow of the plasma jet corresponding to several operating conditions of the Plasmatron and the heat flux at stagnation point can be computed. Due to the unstable features of the jet that are not predicted by the code, differences between numerical and experimental results can sometimes be observed. Therefore, for a correct interpretation of the experimental results, the instabilities that occur in the jet must be understood and quantified.

More recently, a numerical code for the investigation of the stability, developed at the VKI, was developed [29]. Vesta toolkit[4] was first developed for the study of the linear stability of high speed flow, but it was extended to the stability of the high temperature plasma jet [12][7]. It was possible in some cases to identify the unstable features that were observed experimentally. In other cases, no link could be made with the experiments.

---

[3] Computational Object-Oriented Libraries for Fluid Dynamics.

[4] VKI Extensible Stability and Transition Analysis toolkit

By combining both the numerical simulations of the jet and the numerical study of the stability, it would be therefore possible to predict the complete experimental tests. However, a strong link between the results obtained from the numerical stability study and the experimental results needs still to be done.

1.5 Objectives and Overview of the Work

In this work, a numerical approach for the investigation of the plasma jet instabilities occurring in the Plasmatron is used. **Two main research objectives are addressed in this work:**

- **The first objective consists in the identification of the main parameters that are responsible for the instabilities in the plasma jet.** For this purpose, a sensitivity analysis on the influence of the thermodynamic and transport properties on the instability of a plasma jet, when local thermodynamic equilibrium is assumed, is made. Different levels of approximation can be obtained for the expression of the thermodynamic and transport properties that are used in stability analysis calculations. The properties will modified one by one, choosing either the accurate or the less accurate approximation, and relevant quantity of interests translating the unstable features of the jet will be computed. A measure of the change in these quantities of interest will be needed in order to determine the relative importance of each parameter.

- **The second question consists of implementing a methodology for the uncertainty quantification of the instability of the jet, when one of its input parameters is uncertain.** The uncertain input considered here is the electric power that is transferred from the generator of the Plasmatron to the plasma flow.

In order to achieved these objectives, the work is divided in four parts (the first part being the current introduction).

Modelling gas dissociation behind bow shocks around space vehicles requires to take into account complex chemistry mechanisms and detailed transport phenomena. Short review of kinetic theory is made in Chap. 2. Thermodynamic and transport properties for the simple case of Calorically Perfect Gas (CPG) are derived. More elaborated models based on statistical mechanics and the Chapman-Enskog perturbative method for transport properties are then introduced. In the view of their use in the VESTA code, gas properties for plasma flow in Local Thermodynamic Equilibrium (LTE) are also emphasized. A comparison of the flow properties obtained for a calorically perfect gas and for the chemically reacting mixture of perfect gas, is made. Finally, these properties are applied to a practical example of plasma jet obtained from the ICP COOLFLUID solver an this case will be used as the reference case through this work.

Chap. 3 is concerned with the stability analysis of the plasma flow using the VESTA toolkit. First, the Linear Stability Theory is addressed. LST is the base of all computations that will be made in this work, as only linear stability is investigated. Then, a short review of the state-of-the-art on jet instabilities is made in order to get global comprehension of the instability phenomena that can happen in jet flows. Results with the LTE solver of VESTA applied to the reference case for the plasma flow are presented and the main features of the instabilities are analysed.

In Chap. 4 the two main research questions of the project are addressed. Thus, the sensistivity analysis is investigated in Sec. 4.1. The influence of the flow parameters is investigated on two main quantities of interest: the growth rate of an unstable mode and its most amplified frequency. This analysis is performed for different types of instabilities encountered in the plasma jet. Then, in Sec. 4.2 a methodology for quantifying the uncertainty on the instability of the plasma jet is presented. A stochastic collocation method is used. As many simulations may be required for uncertainty quantification, two cases will be considered. On the one hand, the analysis will be made on approximated numerical solutions, obtained from a limited set of simulations. On the other hand, new simulations are computed in order to improve accuracy of the analysis and the two results are compared. In Sec. 4.3, the sensitivity analysis made in Sec. 4 is investigated with an uncertain input using the methodology developed in Sec. 4.2.

Finally, in Chap. 5.1 some conclusions are provided, reviewing the main results obtained in this work. Recommendations for future work are also suggested.

Several appendices are also added for readers who would be interested in more technical notes. In Appendix A, a typical example for the manipulation of the Maxwellian species distribution function for computing macroscopic properties is shown. Appendix B is devoted to the linearization of the gas state equation for the mixture, as parameters appearing in this expression are of utmost importance for the stability of the jet. In Appendix C, the new simulations ran for the uncertainty quantification are presented and their dependence on electric power is shown.

Chapter 2

Transport and Thermodynamic Properties of Plasma Flow

Study of plasma flow, and more generally the study of high-temperature or high-enthalpy gas, is of great interest in the field of hypersonic atmospheric reentry. The physics of these kinds of flow is however completely different than low-temperature flows encountered every day. This chapter is mainly concerned with the physics of high-temperature gas.

The VKI Plasmatron is used to generate high-enthalpy plasma flows that reproduce the real flight conditions at the nose of a spacecraft. The main characteristics of this facility and its operating conditions are first presented in this chapter.

Then, the study of high-temperature gas dynamic, particularized to the plasma flow generated in the Plasmatron is addressed. A simple kinetic model is first described for the representation of transport properties. This model is useful for understanding the basic of kinetic theory and allows us to derived the classical Sutherland's law that can be used to describe the thermal variation of the dynamic viscosity and thermal conductivity for simple gases [35]. Following this, a more rigorous theory based on statistical mechanics is presented: Boltzmann equation and Maxwell transfer equations are derived. Assuming a Maxwellian velocity distribution function leads to the expression of the classical Euler equations and the gas state equation can be retrieved. The Chapman-Enskog perturbative method is developed and Navier-Stokes equations are derived for a plasma jet. Methodology used for deriving rigorous transport properties is presented.

Thermodynamics properties of high-enthalpy flow are then introduced. In classical studies of thermodynamics and compressible flows, the gas is assumed to be calorically perfect and non reacting. The ratio of specific heat $\gamma = c_p/c_v$ is assumed to be constant. These assumptions lead however to unrealistic values of the temperature in the shock layer of hypersonic reentry. Thermodynamics properties of a chemically reacting mixture of perfect gases, under the assumption of local thermodynamic equilibrium are therefore presented.

Finally, a short resume of free jet flows is presented and the Navier-Stokes equations for the plasma jet that will be used for the stability analysis are derived. Thermodynamic and transport properties for the nominal case of plasma jet analysed in this work are finally presented.

2.1 The Plasmatron Facility

The VKI plasmatron facility is the biggest and the most powerful Iductively-Coupled Plasma (ICP) toch in the world. It is used to reproduce actual flight conditions locally, at the stagnation point boundary layer, of a spacecraft during atmospheric reentry phase and to test Thermal Protection Materials (TPMs) that can be used as shields against the heat on spacecraft [5].

The Plasmatron is based on an Inductively-Coupled Plasma (ICP) torch that preserves the heated plasma from pollutants, that were present within former combustion-heated facilities and arc-heaters. Combustion-heated facilities added heavy pollutants from combustion products while arc-heaters produced the electrodes to erode and both were not well-suited for TPS tests. Therefore, Plasmatron facilities using electrodeless technology for the plasma discharge ensure a superior flow purity and are usually more dedicated to the study of aerothermochemistry and gas-surface interaction phenomena.

2.1.1 The plasma torch

In the case of the ICP torch, a tube of quartz is surrounded by a coil that is connected to a high-voltage and high-frequency generator: a few thousand volts and frequencies ranging from 400 [kHz] to several megahertz. When operating, the alternative current is flowing through the coil and creates a magnetic field inside the tube, with magnetic field lines parallel to the axis. According to Faraday's law of induction, this varying magnetic field creates itself an electromotive force that can moves the free electrons existing in the gas, and thus generated and eddy currents (also *Foucault currents*) that heat the gas by Joule effect. The process is sketched on Fig. 2.1.

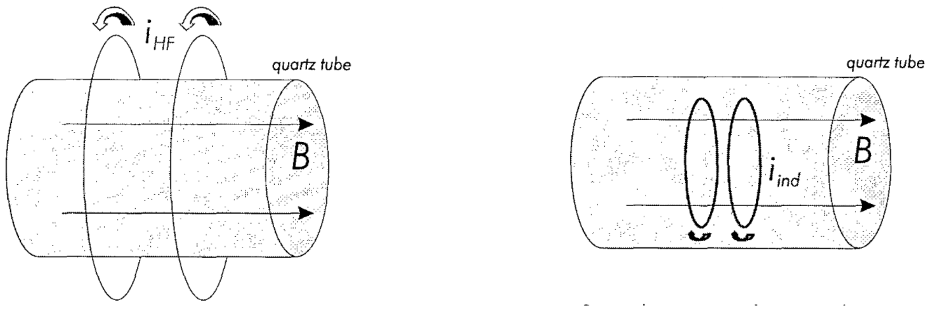

(a) High-frequency current through coil. (b) Induced current loops in the plasma.

Figure 2.1: Electric and magnetic field lines inside de ICP torch. The cold gas is heated by the current loops i_{ind} by Joule effect.

The concept of the ICP torch is sketched on Fig. 2.2. An interior quartz tube is added in order to prevent the exterior tube from melting and confine the plasma in the centre of the tube. A thin layer of cold air is flowing between the two tubes. The cold cage serves as an additional protection for the quartz tube. The gas is injected inside the torch through an annular section and flows around a translational block. The translational block causes a recirculation region behind it that forces the gas to increase its residence time and thus the power received.

A word should be given concerning the translational block. The recirculation region behind it is ideally axisymmetric, but due to manufacturing errors or unbalancing of the test gas injection, it is usually not the case. Vortex shedding can therefore be triggered and the vortices are transported downstream generating instabilities in the jet (this is a second potential source of instability; the first one was already presented in the introduction).

Finally, the heated plasma exits the nozzle in the form of a subsonic jet.

2.1.2 The facility

The Plasmatron facility is equipped with two interchangeable torches, one of 80 [mm] diameter for the test of small samples and one of 160 [mm]. The whole plasmatron facility is sketched on Fig. 2.3. At the exit of the torch, the subsonic plasma enters the test chamber, where the test article is placed. The chamber is usually kept at a pressure between 1200 and 25000 [Pa], depending on the testing conditions. The plasma exists through a diffuser, and it is cooled down by a water-cooled heat exchanger (H/X). The vacuum system is based on a roots pump and a set of three rotating vanes pumps. After

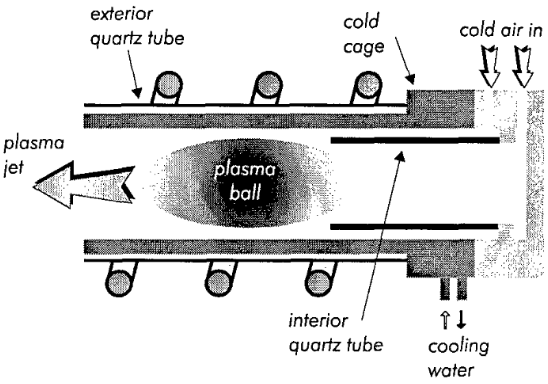

Figure 2.2: Concept of the ICP torch

proper dilution, the products are finally released to the atmosphere through an exhaust. The overall facility is equipped with a cooling system using a closed loop deionized water circuit coupled to fan coolers.

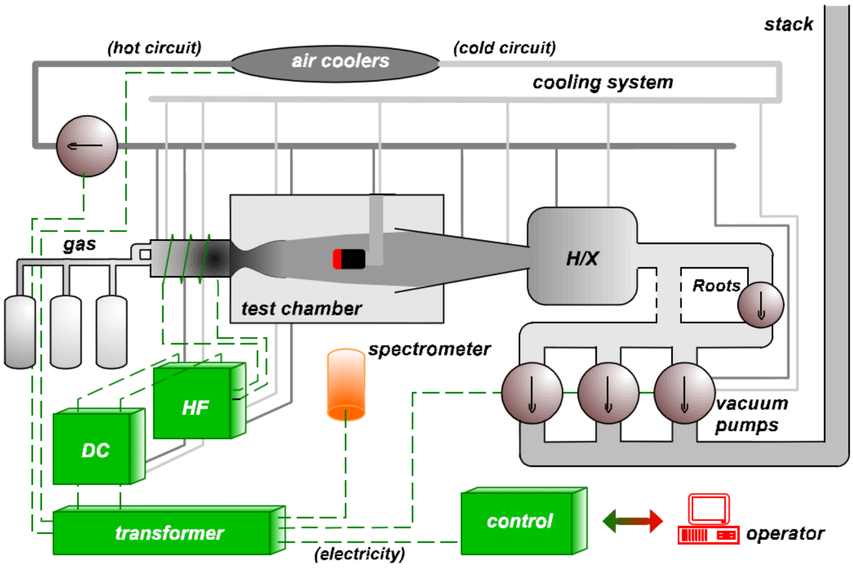

Figure 2.3: Plasmatron facility schematics

2.1.3 Electric system

The plasmatron facility uses a 1.2 MW RF power supply to ignite and sustain the plasma discharge. First, the 11 [kV], 50 [Hz] voltage level coming from the network is adapted using a 1.7 mega volt ampere ([MVA]) transformer (Fig. 2.4). The output signal is then rectified using a 12-pulses bridge and smoothed using chokes. The nominal values of DC voltage and current are 250 [V] and 5000 [A], respectively. A 1.2 [MW], 400 [kHz] metal-oxide-semiconductor (MOS) inverter is then used to feed a single turn flat coil inductor.

Three parameters fully defined operating conditions of the Plasmatron during TPMs testing: the electric power supply P_{el} ([kW]), the pressure in the test chamber p_{tc} ([Pa]) and the mass flow rate of fluid $\dot{m}$ ([g/s]). These parameters are well-defined during a test and typical operating condition ranges are P_{el} between 120 and 300 [kW], p_{tc} between 1500 and 20000 [Pa] and the mass flow rate is often fixed to 16 [g/s][1] [5].

Plasma jet generated in the VKI Plasmatron can be numerically simulated using the

---

[1] But it can be modified as well.

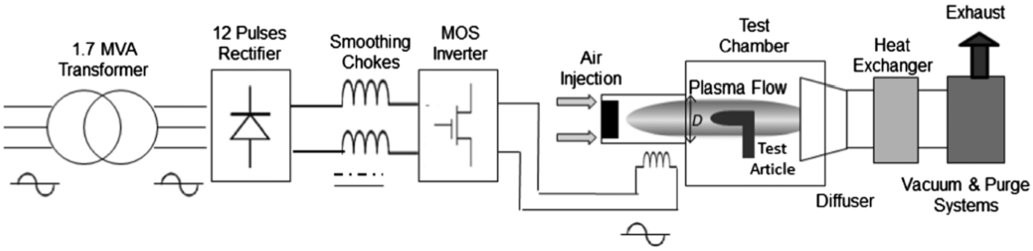

Figure 2.4: Simplified scheme of the VKI Plasmatron system [8]).

VKI solver CooLFluiD[2]. For a numerical simulation, p_{tc} and $\dot{m}$ need to be specified but also the electric power that is effectively transmitted to the flow. While the electric power supplying the Plasmatron facility is well-known as it comes from the network, the power transmitted to the plasma that is actually heating it is not well defined. It is only a fraction of the initial power supply and it can be expressed as

$$P_{fl} = \eta P_{el} \ , \tag{2.1}$$

where P_{fl} is the electric power transmitted to the plasma flow and η an uncertain parameter. We will come to this relation later when uncertainty quantification on the input electric power will be addressed.

2.1.4 Thermal plasma

A plasma is a gas that have the property to conduct an electric current when subjected to an electromagnetic field. Plasma are generally assumed to be the fourth state of matter.

At high temperature, the energy exchange between particles during a collision is sufficiently large for electrons to be extracted and molecules to dissociate: the gas becomes ionized. A gas composed of electrons and ions has the capability of conducting an electric current. The global charge of the gas remains neutral. Therefore, plasma are partially ionized gas and the charge is globally neutral. The plasma investigated for reentry is restricted to unmagnetized plasma, which are plasma for which the effect of the magnetic field on transport properties is assumed to be negligible.

When subjected to an electromagnetic field, the plasma allows a flow of charged particles (either electrons or ions), but they do not allow a separation of the constituent of the gas to be physically separated.

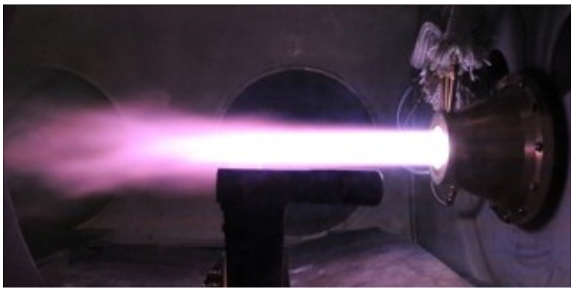

Figure 2.5: Subsonic plasma jet generated inside the Plasmatron with ICP toch of 80 [mm] diameter.

Plasma can be classified in different categories. Plasma jet generated by the Plasmatron facility belong to the field of the thermal plasma. Compared to other fields, like fusion plasma, thermal plasma are of relatively low temperature, and their temperature range is usually assumed to vary between 5000 and 25000 [K]. Inductive plasma generated inside the Plasmatron facility have a typical temperature about 10000 [K].

---

[2] Computational Object-Oriented Libraries for Fluid Dynamics.

It becomes then obvious that classical laws that described the thermodynamic and transport properties of a gas at low temperature will be completely different for such plasma flow and more generally for any high-temperature gas.

2.2 Kinetic Theory of Gases

While thermodynamics deals with phenomenological law for describing macroscopic systems at equilibrium and the transition between them, kinetic theory is a description of the microscopic world based on collisions amongst molecules and atoms. Statistical mechanics allows a bridge to be made between the two descriptions.

Description of the thermodynamics and transport properties is necessary in this work as the stability of the plasma jet will be studied for two different gas model. Correct physical interpretation of the properties based on kinetic theory is exposed in the following sections. Most mathematical development are omitted and the results are assumed to be given.

2.2.1 Simple kinetic model for the transport properties

Transport properties are the results of the spatial non-uniformity of some macroscopic quantity of the gas (as flow velocity, temperature, concentration).

Consider a situation where all the molecules in the gas are assumed to be of one species. These molecules follow a hard sphere model and they all have the same diameter d moving at a relative mean velocity $\bar{C}$ which is the thermal speed, with respect to an immobile particle. The hard sphere model implies that any colliding molecule whose center comes within a distance d of the given molecule is going to cause a collision. We thus define $\sigma = \pi d^2$ to be the *collision cross-section.* During a time Δt, the particle will have travelled a volume $V_I = \sigma \bar{C} \Delta t$. Introducing the particle density $n = N/V$, the number of particle N per unit volume, then the mean number of collisions occurring in the volume of influence V_I is $N_c = n\sigma\bar{C}\Delta t$. Finally, defining the mean free path l as the mean distance between two collisions, we have

$$l = \frac{\bar{C}\Delta t}{N_c} = \frac{1}{n\sigma} \tag{2.2}$$

From the discussion on transport properties at the beginning of the section, we expect that the transport properties will be expressed as a function of the mean free path.

Consider a local stream of particles moving in the x coordinate carrying the same quantity Q, which can be either momentum or energy[3]. We assume that there exists a gradient of the macroscopic property P of the flow in the y coordinate, that is, $\partial P/\partial y \neq 0$. The quantity carrying by the local particles thus depend on their location on the y coordinate, that is, $Q = Q(y)$. It is also assumed that quantity Q did not change of value on a distance equal to the mean free path l, corresponding to the latest collision between two particles. The flux of particles in the y-direction is $n\bar{C}/6$; on average $1/6$ of the particles travel in one direction in the 3D space. The flux of the quantity Q is therefore proportional to $nQ\bar{C}/6$ and the net flux through some surface located at y is therefore

$$\begin{aligned} F_y &\propto \frac{n}{6}Q(y+l)\bar{C} - \frac{n}{6}Q(y-l)\bar{C} \\ &\approx \frac{n}{6}\bar{C}\left(Q(y) + \frac{\partial Q}{\partial y}l - Q(y) + \frac{\partial Q}{\partial y}l\right) \\ &\approx \frac{n}{3}\bar{C}\frac{\partial Q}{\partial y}l \end{aligned} \tag{2.3}$$

---

[3] Transport of mass could also be considered when there is a gradient of concentration

Classical macroscopic theory assumes that momentum and heat fluxes are something proportional to the gradient of velocity and temperature respectively

$$\tau = \mu \frac{\partial u}{\partial y}, \tag{2.4}$$

$$q = -k \frac{\partial T}{\partial y}, \tag{2.5}$$

where μ is the dynamic viscosity and k the thermal conductivity. Considering $Q = mu$ and $Q = c_v T$ respectively for momentum and heat transport, the coefficients can be identified

$$\mu = \beta_\mu \, n\bar{C}l, \tag{2.6}$$

$$k = \beta_k \, n\bar{C}c_v l, \tag{2.7}$$

where β_μ and β_k are new constants of proportionality. Finally, it can be shown from statistical mechanics (see Appendix A) that

$$\bar{C} = \left(\frac{8k_B T}{\pi m} \right)^{\frac{1}{2}}, \tag{2.8}$$

where k_B is the Boltzmann constant (see Tab. 2). Therefore, from these simple kinetic considerations, we can say that the viscosity μ and the thermal conductivity k are at first approximation proportional to $T^{1/2}$. These results also suggest that transport properties are independent from pressure. However it will be shown later that they are not exactly independent from pressure, but the importance of pressure compared to the thermal variation is almost negligible.

Sutherland's law

Consider now the hard sphere model with a weak attractive field in its surrounding. The attractive force will cause more molecules to collide and a greater collision cross-section than the simple πd^2 used previously can be considered. An effective diameter can be used instead (Vincenti & Kruger)

$$d_{\text{eff}}^2 = d^2 \left(1 + \frac{S}{T} \right), \tag{2.9}$$

where S is a constant that is positive for attractive force and is sometimes called the Sutherland's temperature. Replacing d in the expression of the mean free path Eq. 2.2 by this effective diameter and together with Eq. 2.6, we obtain

$$\mu = \beta_\mu \frac{T^{\frac{1}{2}}}{1 + \frac{S}{T}}, \tag{2.10}$$

where $\beta_m u$ denotes again a constant of proportionality for the viscosity. Eq. 2.10 is known as the Sutherland's law and this one predicts a more rapid variation of μ with temperature than the previous simple law in $T^{1/2}$. In fact, at low temperature, attractive intermolecular force is enough for causing a molecule to collide, that would have continued its way if there were no attractive field. At higher temperature, thermal agitation becomes predominant and the weak field is not felt any more by the incoming molecule. In this case, the two models predict a growth of viscosity proportional to $T^{1/2}$.

Defining a reference viscosity $\mu = \mu_{\text{ref}}$ at $T = T_{\text{ref}}$, we can identify the constant $\beta_\mu = \mu_{\text{ref}} / T_{\text{ref}}^{1/2} (1 + S/T_{\text{ref}})$. After some manipulation, this can be rewritten in the more familiar form of the Sutherland's law

$$\mu = \mu_{\text{ref}} \left(\frac{T}{T_{\text{ref}}} \right)^{\frac{3}{2}} \frac{T_{\text{ref}} + S}{T + S}, \tag{2.11}$$

where the reference values and the Sutherland's temperature S can be determined empirically. For air, we have $\mu_{\text{ref}} = 1.7894\ 10^{-5}$ [kg/(m · s)], $T_{\text{ref}} = 288.16$ [K] and $S = 110.4$ [K]. Using these values, the Sutherland's law often gives fairly accurate results for gas such as N_2, O_2, and therefore for air, at low or moderate temperature.

Same considerations can be made for the thermal conductivity and a similar Sutherland's law can be derived:

$$k = k_{\text{ref}} \left(\frac{T}{T_{\text{ref}}} \right)^{\frac{3}{2}} \frac{T_{\text{ref}} + S}{T + S}, \tag{2.12}$$

In this last formula, $k_{\text{ref}} = 2.428\ 10^{-5}$ [kW/(m · K)].

2.2.2 Boltzmann equation

A more rigorous treatment of the kinetic theory by means of statistical mechanics is now addressed. Through the following sections, the basic mathematical treatments of the microscopic description of gases is presented. The aim is to give an idea of the methodology used in order to obtain an accurate description of transport properties necessary for high temperature flow modelling as in the case of plasma jet. In particular, description of the plasma flow in terms on mixture species quantities must be introduced.

A gas is composed of a huge amount of particles. If we were able to know exactly the position $\boldsymbol{x}$ and the velocity of every individual species $\boldsymbol{c_i}$ (*i.e.* by knowing exactly the *microstate* of the gas at a particular instant of time), the evolution of the system could be exactly predicted. This is however a completely hopeless task and a statistical description of the problem must be investigated. Going in this direction, each particles of species i is described in the one-particle phase space $(\boldsymbol{x}, \boldsymbol{c_i})$ by f_i, the so-called velocity distribution function. It gives the probability of finding one particle species i at position $\boldsymbol{x}$ and time t with a velocity $\boldsymbol{c_i}$ [24].

The temporal evolution of the species velocity distribution function f_i is governed by the nonlinear integro-differential Boltzmann equation. This equation can be obtained by expressing the conservation of particles in the phase space. The general form of the equation with no reactive or chemistry source term is

$$\partial_t f_i + \boldsymbol{c_i} \cdot \boldsymbol{\partial_x} f_i + \boldsymbol{b_i} \cdot \boldsymbol{\partial_{c_i}} f_i = \sum_{j \in S} \mathcal{J}_{ij} \left(f_i, f_j \right), \quad i \in S, \tag{2.13}$$

where $\boldsymbol{c_i}$, m_i are the particle velocity and mass and $\boldsymbol{b_i}$ are the specific external force acting on the i^{th} species. This equation can be rewritten more compactly as

$$\mathcal{D}_i(f_i) = \mathcal{J}_i, \tag{2.14}$$

where the streaming differential operator $\mathcal{D}_i(\cdot)$ and the scattering collision operator $\mathcal{J}_i$ has respectively been introduced as

$$\mathcal{D}_i(f_i) = \partial_t f_i + \boldsymbol{c_i} \cdot \partial_{\boldsymbol{x}} f_i + \boldsymbol{b_i} \cdot \partial_{\boldsymbol{c_i}} f_i, \tag{2.15}$$

$$\mathcal{J}_i = \sum_{j \in S} \mathcal{J}_{ij}(f_i, f_j). \tag{2.16}$$

In the case of the plasma jet, the only external force considered acting on the particle is the Lorentz force $m_i \boldsymbol{b_i} = q_i \left(\boldsymbol{E} + \boldsymbol{c}_i \wedge \boldsymbol{B} \right)$, with the electric field $\boldsymbol{E}$, magnetic field $\boldsymbol{B}$ and species charge q_i. The electric and magnetic fields can be obtained from Maxwell's equations but they are not described in this work. Their expression and the derivation of the electromagnetic field in order to model the inductively coupled plasma can be found in [25].

The introduction of the species velocity distribution functions allows for the following mixture and species properties to be defined ($i \in S$):

- species number density

$$n_i = \int f_i d\boldsymbol{c_i}, \tag{2.17}$$

- mixture number density

$$n = \sum_{j \in S} n_j, \tag{2.18}$$

- species mass density

$$\begin{aligned} \rho_i &= \int m_i f_i d\boldsymbol{c_i} \\ &= n_i m_i, \end{aligned} \tag{2.19}$$

- mass density

$$\rho = \sum_{j \in S} \rho_j, \tag{2.20}$$

- hydrodynamic velocity

$$\rho \boldsymbol{u} = \sum_{j \in S} \int m_j \boldsymbol{c_j} f_j d\boldsymbol{c_j}, \tag{2.21}$$

2.2.3 Maxwell-Boltzmann velocity distribution function

The Maxwell-Boltzmann velocity distribution function f_i^M is introduced:

$$f_i^M = n_i \left(\frac{m_i}{2\pi k_B T} \right)^{3/2} \exp\left(\frac{-m_i \left(\boldsymbol{c_i} - \boldsymbol{u} \right)^2}{2 k_B T} \right). \tag{2.22}$$

It corresponds to the velocity distribution for a gas in an equilibrium state.

2.2.4 Maxwell transfer equations

Maxwell transfer equations express conservation of the microscopic properties at the macroscopic level of the flow. There are used to make the link between the two descriptions and the well-know equations of classical fluid mechanics can be retrieved.

First, collisional invariants are introduced. They are microscopic quantity that are globally conserved during a collision between two particles i, $j \in S$ such as the mass, momentum and energy. The conserved quantity are

$$\psi^l = (m_i \delta_{il})_{i \in S}, \qquad l \in S \tag{2.23a}$$

$$\psi^{n^S + \nu} = (m_i c_{i\nu})_{i \in S}, \qquad \nu \in \{1, 2, 3\} \tag{2.23b}$$

$$\psi^{n^S + 4} = \left(\frac{1}{2} m_i \boldsymbol{c_i} \cdot \boldsymbol{c_i} \right)_{i \in S}, \tag{2.23c}$$

where δ_{il} is the Kronecker symbol and n^S denotes the number of species in the mixture. Collisional invariance is then expressed as

$$\psi_i^l + \psi_j^l = \psi_i^{l'} + \psi_j^{l'}, \quad l \in \left\{1, \ldots, n^S + 4\right\}. \tag{2.24}$$

Note that ψ_i^l is a species quantity (mass, momentum or energy), while ψ^l is a species vector. In the same order of idea, ψ can be seen as the species tensor for which the $n^s \times n^s$ first block is diagonal and contains the mass species.

Global conservation equations are then obtained by multiplying the Boltzmann equation by the collisional invariants, integrating over the velocity and summing over the species in the mixture. For that purpose, the following scalar product is introduced

$$\langle\langle \xi, \zeta \rangle\rangle = \sum_{j \in S} \int \xi_j \odot \zeta_j d\boldsymbol{c_j}, \tag{2.25}$$

Projecting the Boltzmann relation 2.13 onto the collisional invariants defined in Eqs. 2.23 and using the scalar product 2.25, we obtain

$$\langle\langle \partial_t, \psi^l \rangle\rangle + \langle\langle \boldsymbol{c} \cdot \boldsymbol{\partial_x} f, \psi^l \rangle\rangle + \langle\langle \frac{q}{m}(\boldsymbol{E} + \boldsymbol{c} \wedge \boldsymbol{B}) \cdot \boldsymbol{\partial_c} f, \psi^l \rangle\rangle = 0, \tag{2.26}$$

with $l \in \{1, \ldots, n^4 + 4\}$. After some algera, conservation equations of mass, momentum and energy are obtained

$$\partial_t \rho_i + \boldsymbol{\partial_x} \cdot (\rho_i \boldsymbol{u}) + \boldsymbol{\partial_x} \cdot (\rho_i \boldsymbol{V_i}) = 0, \quad i \in S, \tag{2.27a}$$

$$\partial_t (\rho \boldsymbol{u}) + \boldsymbol{\partial_x} \cdot (\rho \boldsymbol{u} \otimes \boldsymbol{u}) + \boldsymbol{\partial_x} \cdot \boldsymbol{\Pi} = nq\boldsymbol{E} + j \wedge \boldsymbol{B} \tag{2.27b}$$

$$\partial_t E + \boldsymbol{\partial_x} \cdot (\boldsymbol{u}E) + \boldsymbol{\partial_x} \cdot \boldsymbol{q} + \boldsymbol{\partial_x} \cdot (\boldsymbol{\Pi} \cdot \boldsymbol{u}) = \boldsymbol{j} \cdot \boldsymbol{E}, \tag{2.27c}$$

The following species and mixture properties have been introduced:

- diffusion mass flux of species l

$$\rho_l \boldsymbol{V_l} = \int m_l f_l (\boldsymbol{c_l} - \boldsymbol{u}) d\boldsymbol{c_l}, \quad l \in S, \tag{2.28}$$

- mixture stress tensor

$$\boldsymbol{\Pi} = \sum_{j \in S} \int m_j f_j (\boldsymbol{c_j} - \boldsymbol{u}) \otimes (\boldsymbol{c_j} - \boldsymbol{u}) d\boldsymbol{c_j}, \tag{2.29}$$

- mixture heat flux

$$\boldsymbol{q} = \sum_{j \in S} \int \frac{1}{2} m_j f_j (\boldsymbol{c_j} - \boldsymbol{u})(\boldsymbol{c_j} - \boldsymbol{u})^2 d\boldsymbol{c_j}, \tag{2.30}$$

- mixture charge

$$nq = \sum_{j \in S} n_j q_j \tag{2.31}$$

- total electric current density

$$\boldsymbol{j} = nq\boldsymbol{u} + \sum_{j \in S} n_j q_j \boldsymbol{V_j} \tag{2.32}$$

Gas in equilibrium state

At thermodynamic equilibrium, species diffusion mass flux $\rho_l \boldsymbol{V_l}, l \in S$ and heat flux $\boldsymbol{q}$ vanish. The total electric current density is only due to convection. Mixture stress tensor can be derived explicitly using the Maxwellian distribution velocity f_i^M from Eq. 2.22 and using the change of variable $\boldsymbol{C_j} = \boldsymbol{c_j} - \boldsymbol{u}$, where the $\boldsymbol{C_i}$ are referred as to the peculiar diffusion velocity

$$\begin{aligned} \boldsymbol{\Pi} &= \sum_{j \in S} \int m_j f_j^M (\boldsymbol{c_j} - \boldsymbol{u}) \otimes (\boldsymbol{c_j} - \boldsymbol{u}) d\boldsymbol{c_j} \\ &= nk_B T\, \mathbb{I}, \end{aligned} \tag{2.33}$$

where $\mathbb{I}$ stands for the 3D identity matrix. By identifying this deviatoric shear stress tensor to the hydrostatic pressure, perfect gas law is obtained

$$p = nk_B T. \tag{2.34}$$

Thus, kinetic theory allows the perfect gas equation to be established. It can also be shown for the gas in equilibrium state that the Euler equations are retrieved.

Review

From Eqs. 2.28, 2.29 and 2.30, we saw that for evaluating the transport coefficients, the expressions for the species velocity distribution functions is required. The Maxwell-Boltzmann distribution function, which corresponds to the velocity distribution for a gas in an equilibrium state, led to the Euler equations and allowed the gas state equation to be derived. However, in order to describe the system out of equilibrium and account for dissipative effects in the transport fluxes due to macroscopic forces, we need an evaluation of the velocity distribution function that diverts from the equilibrium. This can be achieved using the Chapman-Enskog perturbative method which is briefly described below.

2.2.5 Chapman-Enskog perturbative method

In order to derive an approximate solution to the Boltzmann equation, species distribution functions are developed in the Enskog expansion

$$f_i = f_i^0(1 + \epsilon\phi_i) + \mathcal{O}(\epsilon^2), \quad i \in S. \tag{2.35}$$

The parameter ϵ can be seen as a measure of the degree of departure from local equilibrium. When the zero-order term of the Enskog expansion is injected to the Boltzmann equation, the solution lead to the Maxwellian distribution and Euler equations can be derived from Maxwell transfer equations. Considering the first order expansion, the linearized Boltzmann equation can be found and lead to the Navier-Stokes equations. Expressions for the transport coefficients can then be derived. Complete mathematical development of the first order solution and the mathematical treatments of the transport coefficient can be found in [35][14].

What should be retained from this section is that there exists no closed solution for the Boltzmann equation (as it is for the Navier-Stokes equations; Boltzmann equation contains however much more information than NS as it this derived from microscopic considerations). An approximation of this equation is thus sought using the Chapman-Enskog series expansion. This theory is the base on which transport property calculations are made.

2.3 Local Thermodynamic Equilibrium Properties

The flow is assumed to be in the state of local chemical and thermal equilibrium, defined as the Local Thermodynamic Equilibrium (LTE) state. The LTE description is only valid for the last portion of a flight trajectoty, where the pressure is large enough such that thermal and chemical relaxation occur rapidly at the characteristic time of the flow.

In the Plasmatron, the thermodynamic state of the plasma has been investigated by Cipullo using optical emission spectroscopy [8]. The results showed that the plasma could be considered at the LTE condition for all the testing conditions.

The thermodynamic and transport properties of air in LTE are presented in this section. The library MUTATION, developed at the VKI is used to compute the different properties.

2.3.1 Mixture composition

When the temperature is increased, the gas must be considered in a "non perfect" fashion as several physico-chemical processes happen: Internal energy as well as chemical reactions must be taken into account.

1) When temperature increased, vibrational energy of molecules becomes excited. Specific heats also becomes a function of temperature and γ is no longer a constant. In this case of variable c_p and c_v, the gas is defined as Thermally Perfect Gas (as opposition to the classical calorically perfect gas). For air, this effect becomes important above 800 [K].

2) Increasing further the temperature, the gas starts to dissociate and chemical reaction occur. For air, oxygen molecules begin to dissociate when temperature is about 2500 [K] while nitrogen begins dissociate at about 4000 [K].

3) Finally, when temperature reaches the 9000 [K], ionization process begins and becomes more and more significant as temperature increases further.

In the two last cases, the gas can be classified in a third categories, namely the Chemically Reacting Mixture of Perfect Gases (CRG). These phenomena are illustrated in Fig. 2.6, reproduced from Anderson [2]. The simplified model of air composed of 5 elements (O_2, N_2, O, N, e^-) is considered in this example.

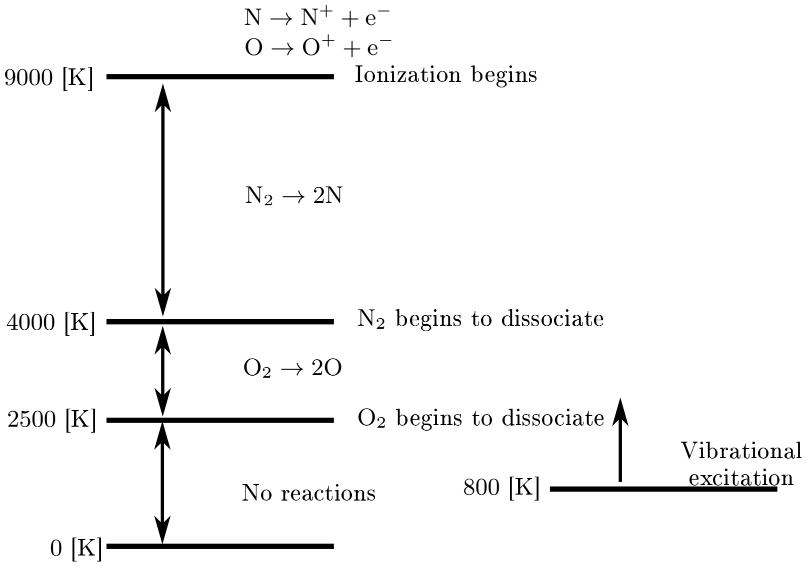

Figure 2.6: Ranges of vibrational excitation, dissociation and ionization for a 5-species air mixture at 1 [atm].

This simple example for the Earth atmosphere composed of five elements illustrates the different phenomena that can happen when the temperature of a gas is increased. A more elaborated model for air is used here as described below. On Earth, the sea-level composition of (dry) air, that is, at a temperature of 288.15 [K] and 101325 [Pa], is taken to be 78.08% N_2, 20, 95% O_2, 0.93% Ar, 0.03% CO_2 and small amounts of other gases [21]. In this work, we consider the simplified model of an 11-species air mixture composed of N_2, NO, O_2, N, O, N_2^+, NO^+, N^+, O_2^+, O^+ and e^-, with 79% of nitrogen and 21% of oxygen.

In the LTE framework, given the elemental molar composition and for a thermodynamic state of pressure p and temperature T, the mixture composition can be computed. The thermal variation of the molar composition for the 11-species air mixture at a pressure of 17143 [Pa][4] is computed in the MUTATION library and the result is presented in Fig. 2.7

At low temperature, the elemental composition is retrieved. When temperature increases, O_2 dissociate first and then N_2. Note that there is a peak of NO near 2500 [K]. The ionization starts near 7500 [K] and becomes noticeable at 8000 [K].

2.3.2 Thermodynamic properties

In the preceding section 2.2 on kinetic theory, the particles were assumed to have only a translational energy. This model corresponds in fact to a mixture of perfect gas where no chemical reactions and no internal structure are taken into account. However, we have just seen that molecules dissociate and react with each other and can even ionize.

---

[4] This value is typical of what is encountered in the Plasmatron. We chose to represent thermodynamic and transport properties at this value as it will be used as the nominal pressure through this work.

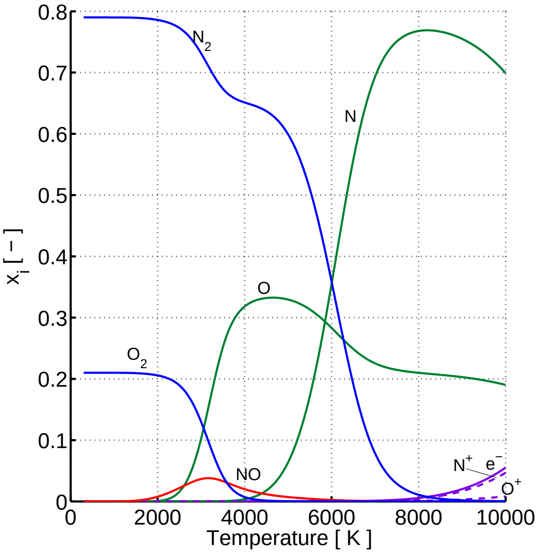

Figure 2.7: LTE composition of major components of air (Air_{11}) at $p = 17143$ [Pa].

The following decoupling of the enthalpy[5] modes is generally assumed

$$h_i(T) = h_i^T(T) + h_i^E(T) + h_i^F(T), \quad i \in H_a, \tag{2.36}$$

$$h_i(T) = h_i^T(T) + h_i^E(T) + +h_i^R(T) + h_i^V(T) + h_i^F(T), \quad i \in H_p, \tag{2.37}$$

$$h_e(T) = h_e^T + h_e^F, \tag{2.38}$$

where H_a is the symbol for the set of indices for atoms, H_p is the symbol for the set of indices for molecules, e denotes electrons and $i \in \mathcal{S}$. For molecules, all modes of energy are possible, namely translational, electronic, rotational vibrational and formation. Formation enthalpy account for the energy realised in the gas by chemical reactions between species. Translational, rotational and vibrational account for the different degree of freedoms in the movement of molecules. For atoms, only translational, electronic and formation modes are possible. For electrons, there are only translational and formation.

The expression of these different energy modes can be obtained from quantum mechanics and statistical mechanics. Quantum mechanics is used for deriving the expressions of fundamental energy states. For instance, translational energies can be obtained from the solution of the Schrödinger equation for a particle confined in a box. Rotational and vibrational energies can be obtained considering the solution for the rigid rotator and the harmonic oscillator. Statistical mechanics is used to derive thermodynamics properties from the fundamental energy equations enumerating the number of different states and their degeneracy. Expressions for the different enthalpy (as well as energy and entropy) modes are not recall here but can be found in standard textbooks [35]. Only physical interpretation of the relations obtained is made here.

The mixture enthalpy is finally obtained by weighting the species properties by the mass densities. The mixture enthalpy reads as

$$h = \sum_{j \in \mathcal{S}} c_j h_j, \tag{2.39}$$

where c_j is the mass fraction ρ_j/ρ of the species j, which can also be expressed in terms of molar fractions as $c_j = x_j \mathscr{M}_j / \mathscr{M}$, where $\mathscr{M}$ is the mixture molar weight and $\mathscr{M}_j$ the species mixture molar weight.

---

[5] The same can be made for energy and entropy modes. Only the relations for the enthalpy are presented as the energy conservation in the Navier-Stokes equations will be expressed in its enthalpy form.

Enthalpy of air at $p = 17143$ [Pa] computed by means of the MUTATION library is represented in Fig. 2.8. As can be seen, the main contribution come from the total formation enthalpy h^F. Other contribution to the equilibrium enthalpy is the translational enthalpy h^T, which is mainly due to molecular agitation in the gas. A zoom on the range of temperatures where vibrational and rotational enthalpies increase is shown in Fig. 2.8b. Above 7000 [K], all the molecules are fully dissociated, and it is not possible anymore to have rotational and vibrational modes of energy as only single particles are considered.

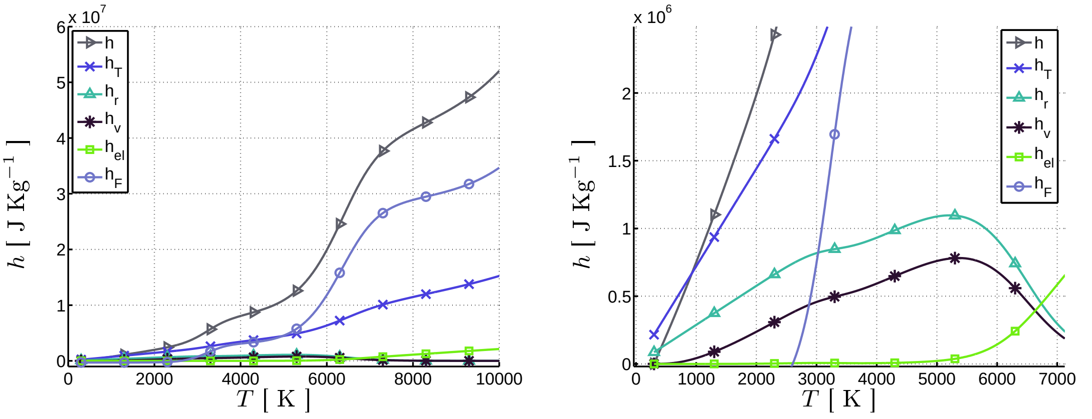

(a) Contributions

(b) Zoom on rotational and vibrational enthalpy

Figure 2.8: Contributions to enthalpy for air at $p = 17143$ [Pa].

Other thermodynamics properties can be derived from the expression of the equilibrium mixture enthalpy, as the equilibrium specific heat at constant pressure

$$c_p = \left.\frac{\partial h}{\partial T}\right|_p . \tag{2.40}$$

2.3.3 Gas state equation

Under the LTE assumption, the gas state equation (2.33) is still of application locally. It can be written in terms of the molar fractions as follows. From $k_B = \mathcal{R}/N_A$, $n = N/V$ and $mN_A/N = \mathscr{M}$, we have

$$p = \rho \frac{\mathcal{R}}{\mathscr{M}} T. \tag{2.41}$$

Using $R_0 = \mathcal{R}/\mathscr{M}_0$, where R_0 and $\mathscr{M}_0$ are the specific gas constant and the mixture molar weight of the air mixture at sea-level conditions (also referred as the *undissociated* values). Mixture molar weight can be expressed from the composition of the gas using the molar fractions x_i as

$$\mathscr{M} = \frac{m}{\mathscr{N}} = \frac{\sum m_i}{\mathscr{N}} = \frac{\sum \mathscr{N}_i \mathscr{M}_i}{\mathscr{N}} = \sum x_i \mathscr{M}_i \tag{2.42}$$

Therefore the gas state law can be written, for a mixture of perfect gas in LTE as

$$p = \rho R_0 T \zeta, \tag{2.43}$$

where we introduced the factor of compressibility ζ which expressed as

$$\zeta = \frac{\sum_{i \in \mathcal{S}} x_{0,i} \mathscr{M}_{0,i}}{\sum_{i \in \mathcal{S}} x_i \mathscr{M}_i}, \tag{2.44}$$

$$= \frac{\mathscr{M}_{\text{undiss}}}{\mathscr{M}_{\text{diss}}}. \tag{2.45}$$

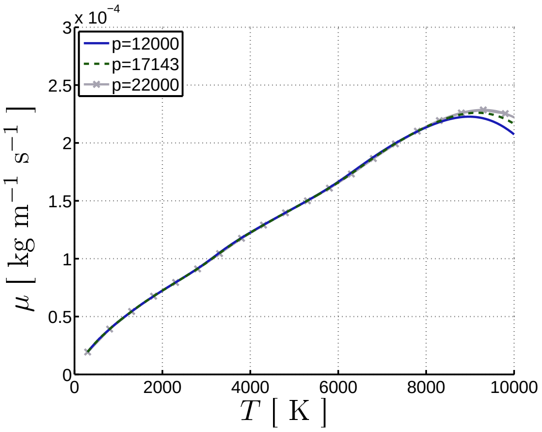

Figure 2.9: Viscosity of air as a function of temperature and variation with pressure.

where $\mathscr{M}_{0,i}$ corresponds to the molar weight of species i at sea-level (standard pressure and temperature), $x_{0,i}$ the elemental fraction of element. The others quantities that appear in Eq. 2.45 are defined at the local equilibrium temperature T. For the 79% of nitrogen and 21% of oxygen Earth atmosphere, $\mathscr{M}_{\text{undiss}} = 28.84$ [g/mol].

If we were considering a 5-species air mixture (N_2, NO, O_2, N, O), we would have $\zeta \to 2$ at sufficiently high temperature ($T > 8000$ [K]), when all N_2 and O_2 are dissociated in N and O. However, for the 11-species air mixture, ionization is triggered near 7000 [K] and ζ increases further. Of course, for the calorically perfect gas, there is no dissociation ($\mathscr{M}_{\text{undiss}} = \mathscr{M}_{\text{diss}}$) and $\zeta = 1$.

2.3.4 Transport properties

The transport properties can be obtained from the rigorous theory of Chapman-Enskog considering a chemically reacting mixture of perfect gas. A correction from the kinetic theory shown in the previous section is needed in order to account for chemical reactions and internal structures. Elaborated cross-section that consider accurate particle interactions can also be derived. Their development requires a mathematical treatment that is out of the scope of this work and it is not reviewed here. They are however implemented in the MUTATION library and the transport properties thus obtained are discussed from a physical point of view.

Viscosity

The shear viscosity computed with the MUTATION library is shown in Fig. 2.9. As predicted by the simple kinetic theory, the viscosity increases with temperature, except that now some modulations can be observed. These ones can be linked to the change of the composition of air due to molecular dissociation that could not be predicted from the simple model. For temperatures greater than 8000 [K], the viscosity starts decreasing. This corresponds to the ionization process that is triggered in the gas. In fact, the growth in the number of charged particles increases the number of collisions in the gas and the mean free path is reduced. The overall viscosity is therefore reduced (consider Eq. 2.6). For higher temperatures, the effect of ionization would be much more effective and the decrease more significant.

In Fig. 2.9, the influence of pressure is also considered. The range of pressure represented corresponds to conditions that can be met in the Plasmatron. Compare to the thermal variation, the pressure has a little influence on the viscosity. The pressure modifies slightly the viscosity when ionization starts.

Thermal conductivity

The mixture heat flux is written here as

$$\boldsymbol{q} = -k\boldsymbol{\partial_x}T, \tag{2.46}$$

where k is the equilibrium thermal conductivity of the gas mixture, is still applicable, if heat transport due to chemical reactions and the contribution of internal energy are considered. The thermal conductivity comes from several physical phenomena and the following decomposition in its different contributions is assumed:

$$k = k_{\mathrm{react}} + k_{\mathrm{soret}} + k_{\mathrm{int}} + k_{\mathrm{h}} + k_{\mathrm{e}}, \tag{2.47}$$

where k_{react} is the thermal reactive conductivity due to diffusion of mass species (Fick's law), k_{soret} is the Soret thermal conducitivity (also linked to diffusion heat flux), k_{int} is the contribution of internal energy modes, gathering the roational, vibrational and electronic thermal conductivity, k_{h} the translational thermal conductivity of heavy particles and k_{e} the translational thermal conductivity of electrons. The result obtained from MUTATION is shown in Fig. 2.10. The different contributions are shown in Fig. 2.10a and variation with pressure in Fig. 2.10b.

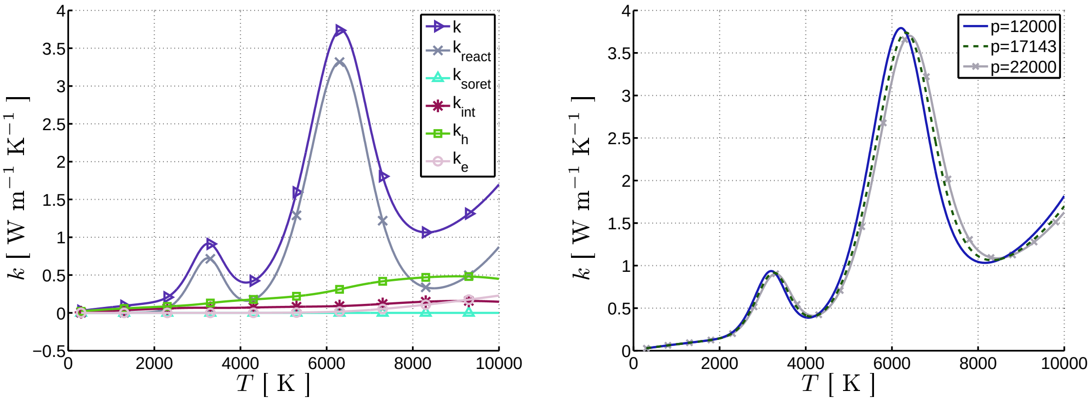

(a) Contributions (b) Variation with pressure ([Pa])

Figure 2.10: (a) Contribution to thermal conductivity for air at $p_{tc} = 17143$ [Pa] and (b) variation of thermal conductivity with pressure.

The term k_{react} is responsible of the major contribution to the thermal conductivity. It is associated to the transport of enthalpy due to diffusion mass species and a large amount of energy is released when molecules dissociate. The peaks in the thermal conductivity are therefore linked to the dissociation and the maximum occur where strong variations in the molar fractions x_i are observed, or equivalently, when the enthalpy increases (Figs. 2.7 and Fig. 2.8a). The translational thermal conductivity of heavy particles k_{h} presents the same behaviour as the viscosity. k_{h} and k_{int} are the major component below 2000 [K] and between the peaks. Translational thermal conductivity of electrons appear when ionization starts, i.e. above 7500 [K].

Considering the variation of the thermal conductivity with pressure presented in Fig. 2.10b, it can be seen once again that this effect is very negligible compared to the thermal variation.

2.3.5 Comparison of the properties of a calorically perfect gas with the properties of a mixture of perfect gases in LTE

The properties obtained from the MUTATION library are compared with the classical law of a calorically perfect gas in Fig. 2.11. It can be noted that the two theories are in good agreement at low temperature gas.

The viscosity (Fig. 2.11a) computed from Sutherland's law predicts a lower increase with temperature than the accurate relation obtained from MUTATION. The two results are not so different and moreover the coefficients in the Sutherland's law could be fitted in order to correspond better to the accurate curve. Of course, at high temperatures, Sutherland's law can not predict the decrease in the viscosity due to ionization, as the gas is considered to be perfect.

The comparison of the Sutherland's law for the thermal conductivity with its accurate expression shows that these two results are quite different. The Sutherland's law was only an expression of the thermal conductivity due to the transport of energy of heavy particles (k_{h}) and predicted a $\sqrt{T}$ growth (compare with k_{h} in Fig. 2.10a, they look quite similar). The different peaks due to reactive thermal conductivity could not be predicted by the simple kinetic model.

The second viscosity coefficient λ (Fig. 2.11c) is equal to $-2/3\mu$ (Stoke's hypothesis) and has therefore exactly the same shape as μ.

By definittion, a calorically perfect gas is one with constant specific heats c_p and c_v. In turns, the ratio of specific heats $\gamma = c_p/c_v$ is constant. For this gas, the enthalpy and internal energy are functions of temperature only, given explicitly by

$$h = c_p T, \tag{2.48}$$

$$e = c_v T, \tag{2.49}$$

where $c_p = 7/2R_0$ and $c_v = 5/2R_0$ for the air considered as a calorically perfect gas. Comparison between the CPG and the CRG gases is made in Fig. 2.11d. It can be noticed once again that the Sutherland's law is well representing the translational enthalpy (refer to Fig. 2.8a). On the other hand, discrepancies between the two laws can become very high at high temperature as the enthalpy of the CPG gas does not account the chemical reactions, which are the most influencing the total mixture enthalpy.

Density ρ in Fig. 2.11e is given by the classical gas state equation $\rho = p/(R_0 T)$ for a calorically perfect gas. The two models give almost the same result. At high temperature, the gas has a very low density and the role played by the factor of compressibility ζ in the expression for the density is negligible.

Finally, ζ is shown in Fig. 2.11. For the CPG gas, it is trivially equal to one. For the CRG gas, ζ is an increasing function of temperature. The increase in ζ can again be related to the different molecular dissociations and ionization: the first increases in the range $T \in [3000, 4000]$ K, is due to the dissociation of O_2 in O and the second increase in the range $T \in [5000, 8000]$ is due to the dissociation of N_2 in N. Finally above 8000 [K], ionization starts slowly an ζ increases further. Thus, the changes in ζ are only due to the molar fraction x_i.

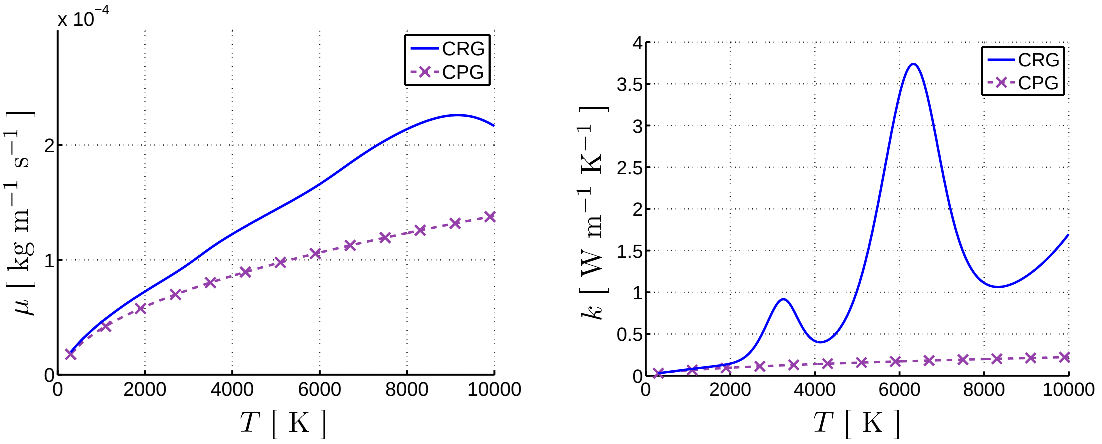

(a) Dynamic viscosity

(b) Thermal conductivity

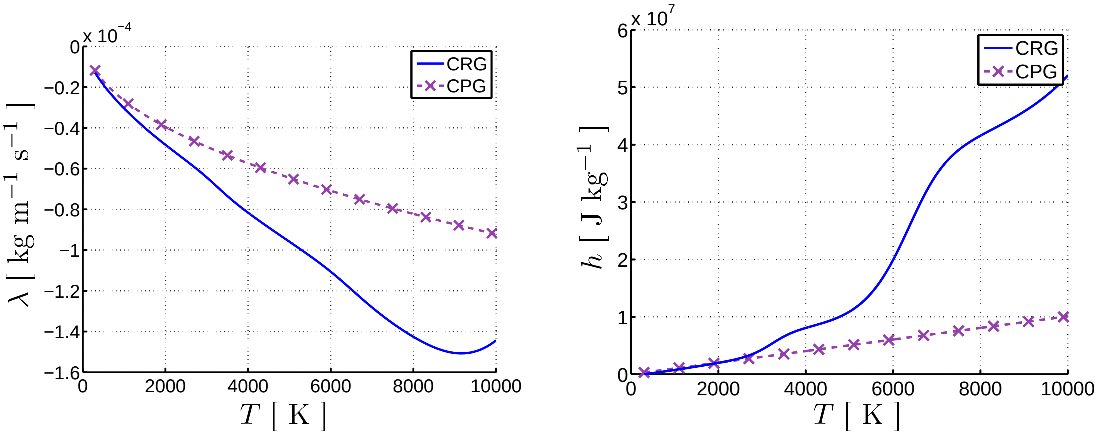

(c) Second viscosity coefficient

(d) Enthalpy

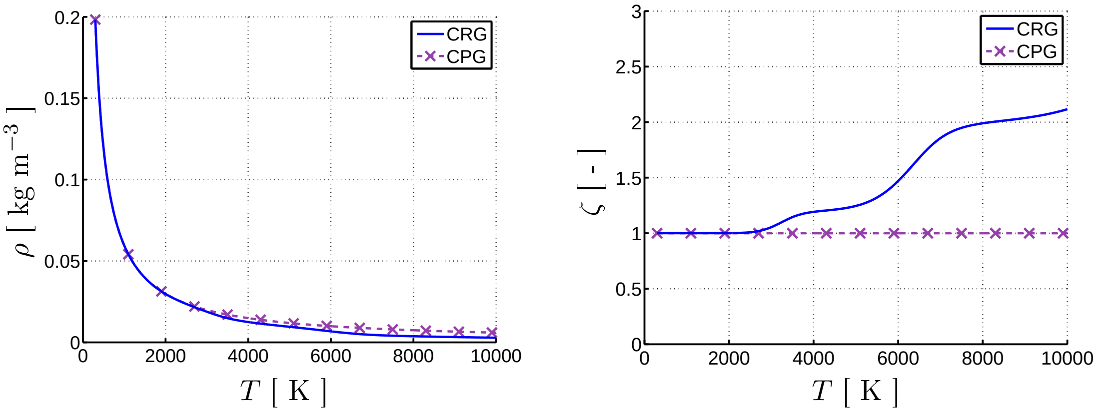

(e) Density

(f) Compressibility factor

Figure 2.11: Comparison of the properties of a calorically perfect gas with the properties of a chemically reacting mixture of perfect gases in LTE as a function of temperature.

2.4 Properties of the Plasma Jet in Local Thermodynamic Equilibrium

2.4.1 General description of free jet flows

A jet is an efflux of fluid originated from a long and narrow orifice. Jets are also called free jet flows as they are not confined by solid walls. The orifice can be planar or circular and in the latter case the jet flow is naturally called a *circular jet*. The surrounding is assumed to be made up of the same fluid as the jet itself, and some of this ambient fluid is carried along with the jet by the viscous drag at the outer edge of the jet, as sketched on Fig. 2.12. The process of drawing in the surrounding fluid from the sides of the jet by frictional forces is called *entrainment*. The ambient fluid can be at rest or moving at very low velocities.

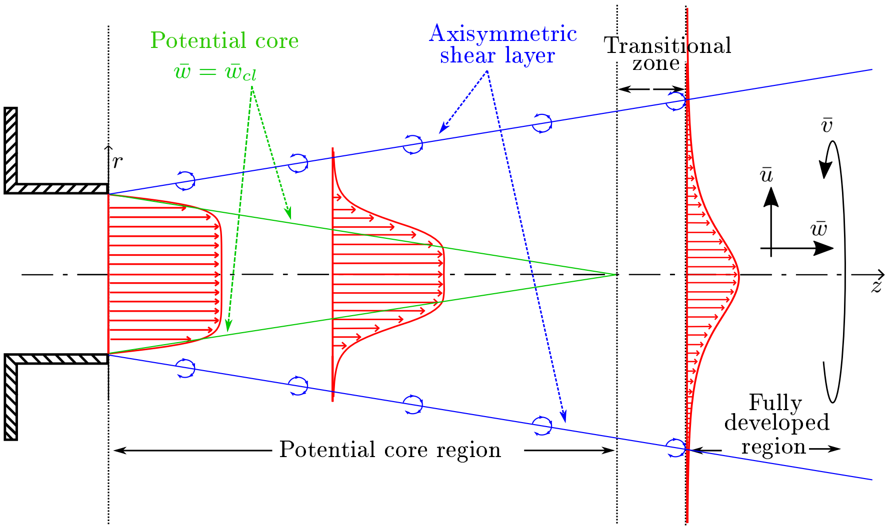

Figure 2.12: Sketch of a free jet flow.

The flow field of a jet can be roughly divided into three distinct regions:

- **The potential core region**: in this first section, there is a core of flow with undiminished velocity equal to the exit velocity and the centerline velocity W_{cl}. This core is surrounded by two convergent annular shear layers where turbulence occurs. At the beginning of the core region, the shear layer is very thin and often modeled by a vortex sheet, as in the theoretical studies of Gill and Tam and Hu. The “tophat” profile also belongs to the potential core region with a thin but finite shear layer. This region can be represented by hyperbolic-tangent functions.
- **The transitional zone**:
- **The fully developed region**: this region can be represented by a Gaussian or a parabolic profile and this profile is self-similar. The studies of Batchelor and Gill, Lessen and Singh and Morris all chose the same parabolic profile. The profile is characterized by a thick shear layer with slowly varying velocity

A comprehensive account of the theory of free turbulent jets was given by Abramovich [1] and Rajaratnam [30]. In most practical cases the circular jet is turbulent and has been widely studied in literature. However the case of laminar jet leads to similar behaviour as for the turbulent jet [31]. Jet flows are parts of free shear flows that can all be related to the *boundary layer theory*. Indeed, boundary layers exist not only next solid walls but also in jets and wakes which are all characterized by a finite viscous layers. The transition from the centerline velocity in the potential core to the zero free stream velocity at some distance of the jet takes place in a very thin layer, the so-called boundary layer. The boundary layer theory has been widely studied by H. Schlichting [31] and he devoted major effort to the problem of the stability of laminar boundary-layer flows. More recent study on boundary-layer theory and stability are found in the work of Kundu and Cohen [19].

Jet governing equations

As circular free jets are investigated in this work, a cylindrical coordinate framework is used for the description of the jet. In this framework, r stands for the radial direction, θ for the azimuthal angle and z to the streamwise (or axial) direction. We shall adopt a system of coordinates with its origin in the slit and with its longitudinal axis coinciding with the jet axis. The velocity vector is again denotes by $\boldsymbol{u}$ with velocity components u, v and w respectively the radial, azimuthal and axial velocity. The velocity vector can be written as $\boldsymbol{u} = (u, v, w)$. An axisymetric configuration is retained to model the jet, that implies that derivatives in the azimuthal direction θ cancel, $\frac{\partial}{\partial\theta} = 0$.

The strong coupling between the Maxwell's and the Navier-Stokes equations mainly takes place inside the torch, where the plasma is heated.

The plasma jet is described by the full set of Navier-Stokes equations for which the electromagnetic field is obtained from Maxwell's equations. This must be rigorously resolved in order to obtain the correct flow field.

In the case of the linear stability theory, some simplifications are made. The strong coupling between Maxwell and Navier-Stokes equations mainly takes place inside the torch, where the plasma is heated. Outside the jet, the mass forces due to the electromagnetic field are assumed to be negligible and the terms in the right-hand side vanished. The Plasma jet considered will be considered decoupled from Maxwell's equations, which is quite correct when a solution sufficiently far from the nozzle is sought.

The following hypothesis are assumed for the jet flow.

- Stationary flow ($\frac{\partial}{\partial t} = 0$).
- Axisymmetric configuration ($\frac{\partial}{\partial\theta} = 0$).
- The mass forces are negligible ($Fr >> 1$). This approximation does not hold inside the torch as strong electromagnetic field is produced for the heating of the plasma. However, only the flow outside the torch is investigated in this work and Lorentz forces can be neglected.
- Jet is a slender structure ($l_z >> l_r$).
- Boundary layer approximation ($p = p(z)$).
- No swirl ($v = 0$).

The dimensionless equations that describes a hot jet in cylindrical coordinates are

$$\frac{\partial(\rho w)}{\partial z} + \frac{1}{r}\frac{\partial(\rho r u)}{\partial r} = 0, \tag{2.50a}$$

$$\rho w\frac{\partial w}{\partial z} + \rho u\frac{\partial w}{\partial r} = \frac{1}{Re}\frac{1}{r}\frac{\partial}{\partial r}\left(r\mu\frac{\partial w}{\partial r}\right), \tag{2.50b}$$

$$\rho w\frac{\partial T}{\partial z} + \rho u\frac{\partial T}{\partial r} = \frac{1}{PrRe}\frac{1}{r}\frac{\partial}{\partial r}\left(rk\frac{\partial T}{\partial r}\right) + \frac{(\gamma-1)M^2}{Re}\left(\frac{\partial w}{\partial r}\right)^2. \tag{2.50c}$$

μ and k are the dimensionless dynamic viscosity and thermal conductivity respectively. All these variables are made dimensionless with their centerline value at the aperture and with the nozzle radius for length variables. The adimensional numbers are therefore: $Re = \rho_c W_c R/\mu_c$ for the Reynolds number, $Pr = \mu_c, c_p/k_c$ for the Prandtl number, $M = W_c/\sqrt{\gamma \mathcal{R} T_c}$ for the Mach number. γ is the ratio of specific heats c_p/c_v and $\mathcal{R}$ is the universal gas constant with $\mathcal{R} = 8314$ [J/(Kmol K)]. Eq. 2.50a is the mass conservation, or continuity equation for stationary compressible flow. Eq. 2.50b is the momentum equation in the streamwise direction. Momentum equation in radial direction can be substituted equivalently by the boundary layer assumption while the azimuthal momentum equation is automatically satisfied for axisymmetric problems. Eq. 2.50c is the energy equation. Streamwise momentum (2.50b) is obtained assuming a newtonian fluid and using Stokes' hypothesis. Stokes' hypothesis has no impact when fluid is considered as incompressible, as the second viscosity coefficient λ multiplies as divergence term in momentum and energy equations. For most compressible flow, this hypothesis works but is unproven. However, for hypersonic flow and inductive plasma (thermal expansion), these terms could not be negligible [10].

These equations must be completed with adequate boundary conditions

$$r = 0: \qquad \frac{\partial W}{\partial r} = U = \frac{\partial T}{\partial r} = 0, \tag{2.51a}$$

$$r \to \infty: \qquad W = T - \frac{T_{\text{amb}}}{T_0} = 0 \tag{2.51b}$$

and initial conditions at $z = 0$

$$0 \leq r \leq 1: \qquad W(r) - \frac{W_j(r)}{W_0} = T - \frac{T_j(r)}{T_0} = 0, \tag{2.51c}$$

$$r > 1: \qquad W = T - \frac{T_{\text{amb}}}{T_0} = 0. \tag{2.51d}$$

2.4.2 Numerical model for the plasma jet

The numerical solution of the Navier-Stokes equations, coupled with Maxwell's equations, are solved numerically by the solver CooLFluiD developed at the VKI. An implicit time marching method is used to reach a steady state solution. At each time step, two linear system are solved using iterative methods. The equations for the electromagnetic field are first solved independently of the hydrodynamic field and then Navier-Stokes equations are solved. At each iteration step, thermodynamic and transports properties are evaluated, increasing significantly the computational cost.

Practically, a mean solution for the plasma flow can be obtained providing the mass flow rate $\dot{m}$, the pressure in the test chamber p_{tc} and the power injected to the plasma flow P_{fl}. In Fig. 2.13, the numerical simulation for the plasma jet at $p_{tc} = 17143$ [Pa], $\dot{m} = 16$ [g/s], $P_{fl} = 85$ [kW] is presented. The flow field is computed assuming the 11-species air mixture model. The parameters are summarized in Tab. 2.1 and this case will be called the nominal case (the meaning of z_{jet} will be explained in a few lines). Sensitivity analysis and uncertainty quantification will be based on this reference case. It seems therefore important to present the solution obtained for this set of parameters and its main features. In this work, the case of the jet with no probe (no TPM) in the Plasmatron is considered, so that no ablation species can be found inside the jet.

p_{tc} [Pa]	$\dot{m}$ [g/s]	P_{fl} [kW]	z_{jet} [m]	Fluid mixture
17143	16	85	0.6	Air_{11}

Table 2.1: Parameters of the nominal case.

Figs. 2.13a and 2.13b are the mean streamwise velocity and temperature fields. Relatively low values for the streamwise velocity and high temperature values near the centerline can be observed. Fig. 2.13c confirms the boundary layer approximation (outside the nozzle) as the relative pressure $\Delta p = |p - p_{tc}|$ is almost zero everywhere inside the chamber.

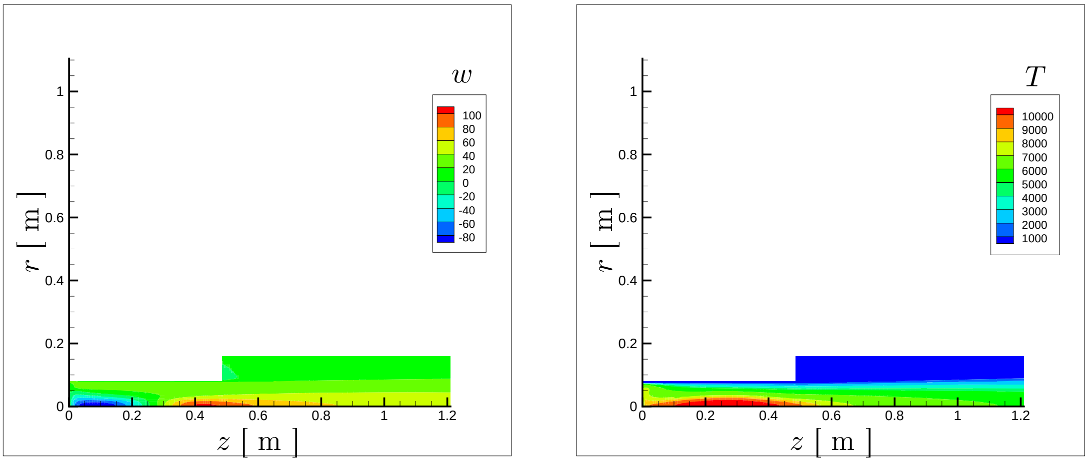

(a) Streamwise velocity [m/s]

(b) Temperature [K]

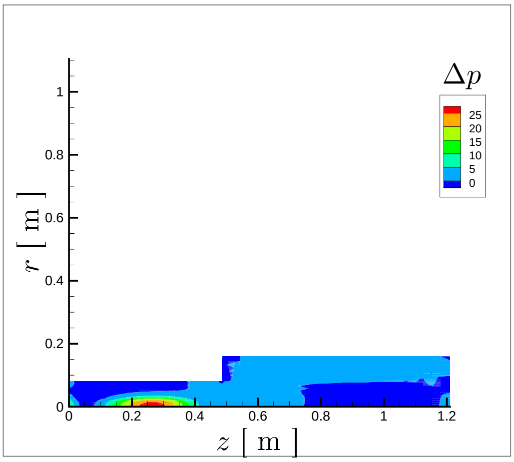

(c) Relative pressure [Pa]

Figure 2.13: Numerical simulation of mean streamwise velocity, temperature and pressure of the plasma jet from the ICP CooLFluiD solver.

The linear stability analysis of the plasma jet will be performed only at a given location inside the chamber. We will limit ourselves to the case $z_{\text{jet}} = 0.6$ [m]. Referring to Fig. 2.13 this is the solution extracted at $z = 0.6$ [m] inside the chamber. The one dimensional profiles obtained are given in Fig. 2.14. Values for the centerline velocity and the centerline temperature are respectively $W_{cl} = 79.14$ [m/s] and $T_{cl} = 7537.5$ [K]. The extraction is necessary for the stability analysis (presented in the next chapter) for which local parallel flow hypothesis is made.

Note

In the sensitivity analysis performs in chapter 4, the stability of the jet when thermodynamic and transport properties are modified is investigated. It is important to mention at this point that the influence of the flow properties on the flow field obtained from CooLFluiD is of course not investigated. Using non accurate laws for the properties could lead to non plausible results and a stability analysis would be hopeless. The profiles obtained from these numerical simulations are thus considered to be the raw data on which stability analysis is directly performed.

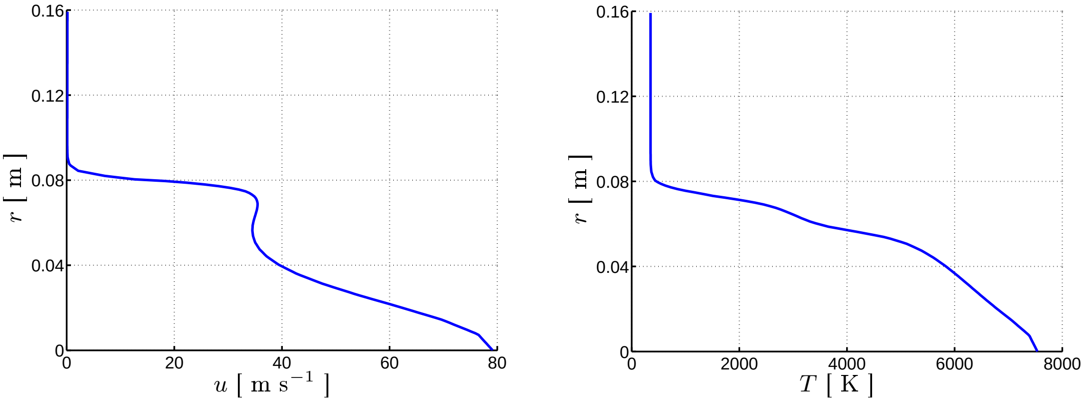

(a) Streamwise velocity

(b) Temperature

Figure 2.14: Mean streamwise velocity and mean temperature profiles for the nominal case at $z_{jet} = 0.6$ [m].

2.4.3 Thermodynamic and transport properties of the jet in local thermodynamic equilibrium

The properties of the chemically reacting mixture of perfect gases in LTE are applied to the temperature profile of the jet obtained from the CooLFluiD numerical simulation with the parameter of the nominal case. Results are show on Fig. 2.15 and are represented by the continuous lines. This representation was made possible thanks to the LTE hypothesis. Assuming this, the properties of the jet can be determined by local inspection. In fact, the corresponding property at a particular location in the radial coordinate can be assigned locally a temperature and an equilibrium state and the MUTATION properties at equilibrium, presented in the previous section, can be used as a look-up table.

Properties for a calorically perfect gas are also used for the high temperature jet and are represented in dotted in Fig. 2.15. For each flow properties, its value is underestimated near the centerline, as the temperature is high. On the contrary, outside the jet the two theory predict quite well the properties of the flow. As expected, the two theory converge at low temperature. Note that ρ is not very different considering either the CRG or the CPG properties. Near the centerline, density is very low and the parameter ζ, i.e., the mixture composition, has only a small influence on the density.

Once all profiles are knwon, adimensional number can be obtained. Considering either the CRG or the CPG properties, they will be slightly different. From the values of Mach and Reynolds, the flow is subsonic and laminar, as already stated.

	Re	M	Pr	Ec	H
CRG	127.38	0.035	0.847	0.00013	0.00289
CPG	423.102	0.0455	0.626	0.00082	0.00289

Table 2.2: Adimensional numbers for the nominal case of the plasma jet.

The properties of the jet obtained in this section are directly used, after adimensionalization, for the study of the stability. It is worth to mention that these profiles are actually mean profiles, as they were computed using the mean temperature. Velocity, temperature, thermodynamic and transport properties altogether determine the stability of the jet. Their derivatives can also play a significant role in the stability. The linear stability presented in the next chapter will be used to investigate the evolution of these profiles when they are subjected to small perturbations.

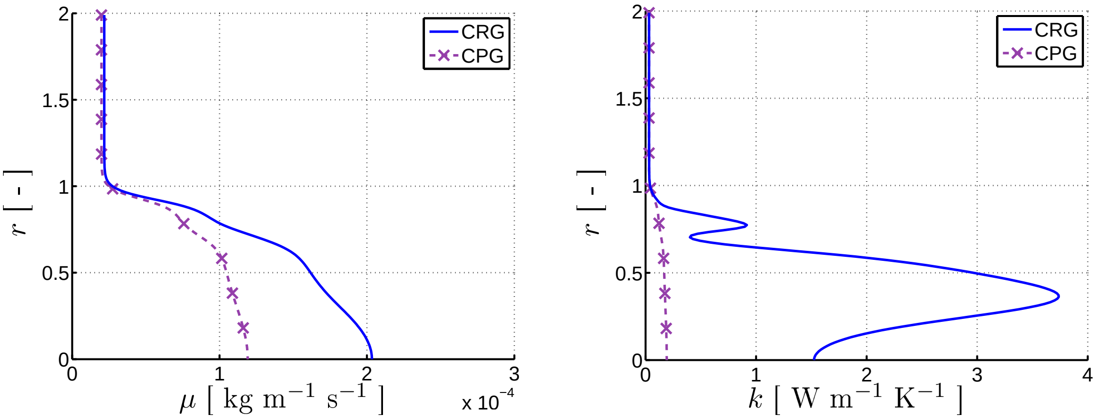

(a) Dynamic viscosity (b) Thermal conductivity

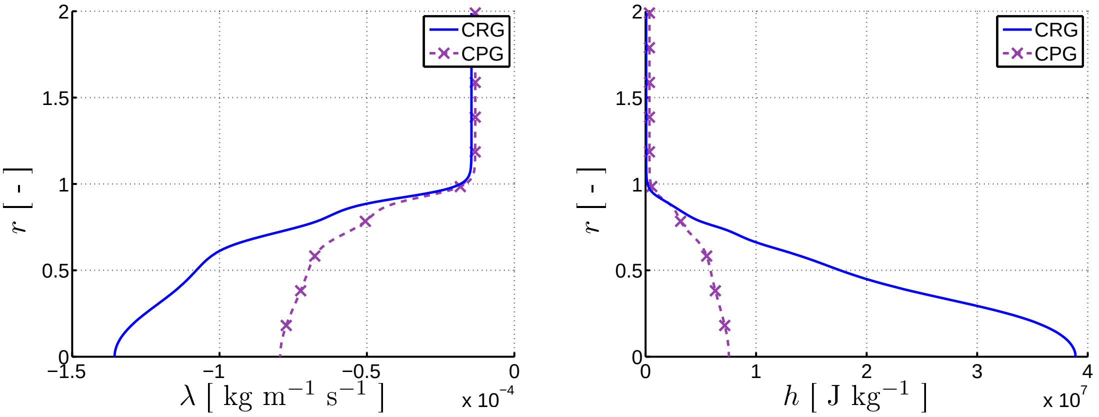

(c) Second viscosity coefficient (d) Enthalpy

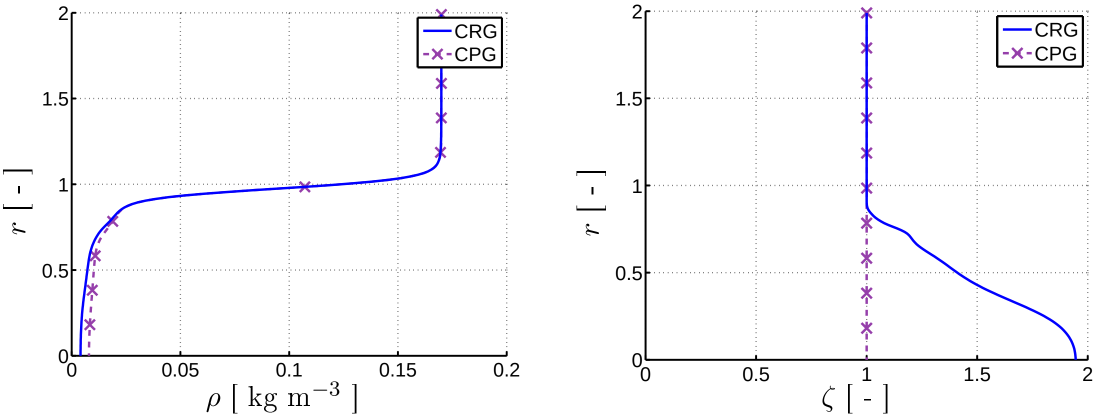

(e) Density (f) Compressibility factor

Figure 2.15: Comparison of the properties of a calorically perfect gas with the ones of a chemically reacting mixture of perfect gases in LTE applied to the nominal case of the high temperature plasma jet as a function of the adimensional radial coordinate.

2.5 Summary of the Chapter

Two models for high temperature gas were investigated. On the one hand, a simple model based on the kinetic theory and neglecting internal energy as well as chemical reactions. This model was referred to as the calorically perfect gas model and showed to be accurate for low or moderate temperature flow. On the other hand, a more sophisticated model based on a kinetic theory and the statistical mechanic of the Boltzmann equation and accounting for internal energy as well as the chemistry of high temperature flow in local thermodynamic equilibrium. The calorically perfect gas model was shown to underestimate all the properties predicted by the more accurate model. These accurate and non accurate thermodynamic and transport properties were then applied to a new reference case for the high temperature plasma jet in LTE.

Chapter 3

Hydrodynamic Instabilities and Linear Stability Theory

The first interest in the study of stability was in the prediction of the transition from laminar to turbulent regimes. In aeronautics, the prediction and control of the transition is of great interest for limiting drag due to turbulence and thus reducing fuel consumption. In aerospace design, it is desirable to predict accurately the transition during reentry phase for a better sizing of the TPS and thus enhancing the overall efficiency of the spacecraft. In the present case of the plasma jet, the stability analysis is not used to define the parameters at which transition occurs. It is rather used to determine the intrinsic behaviour of the unstable plasma jet and try to identify the mechanisms that are responsible for the instabilities observed during experimental tests. By combining both numerical simulations of the mean flow and stability analysis, it would be possible to reproduce numerically the experimental behaviour.

The restricted number of existing codes devoted to the study of the linear stability of high-temperature and hypersonic flows, and the growing interest in the aerospace field for such transitions led to the development of a consistent toolkit in the VKI. VESTA (VKI Extensible Stability and Transition Analysis), developed first by Pinna, is aimed to study the stability of flow at different regimes, from low to high Mach numbers [29].

The toolkit gathers a number of codes used for the resolution of different flow regimes. They are all based on the same Chebyshev pseudo-spectral collocation method for the resolution of the differential stability equations of fluid mechanics. The code was developed in a very modular way in order to allow further developments to be added to the existing core. Historically speaking, the code was first developed by Pinna (2012) for the linear stability analysis for flow from low to high Mach numbers in a Cartesian coordinates system. The validation of the code was made on blasius boundary layer test cases. A branch taking into account the stability of flow mixture in LTE was also developed. Shortly after, Parabolized Stability Equations (PSE) have been developed by Groot and incorporated to the compressible solver of VESTA [16]. Although PSE can take into account a slow streamwise evolution of the flow, which would be more suited to the case of the plasma jet, these ones are not considered in this work (and PSE has not been yet extended to the LTE solver). The code of Pinna was then extended to cylindrical problems by Garcìa Rubio (2013) and verification test cases were made from simple poiseuille flow to the axisymmetric hot jet, considered at that time as a calorically perfect gas [12]. He performed a study on the length of the domain for unbounded flow (jet) for the determination of the computational domain that is required for the discretisation in order to remove the influence of the boundary conditions. It appears that the jet domain must be of the order of 10 to 15 times the jet radius. The range of valid Mach numbers also appeared to be lower than 3. The linear stability equations in a cylindrical reference frame were finally extended to flow under the LTE hypothesis by Chiatto (2014) and verification test cases were made on axisymmetric jets and for the plasma jet in the VKI Plasmatron. Nevertheless, a strong link between the results coming from VESTA with the experiments for the plasma jet still need to be done for the validation.

In this chapter, we discuss first some few aspects about the interest of studying stability and why it is important in the case of the plasma jet. A short introduction to the linear stability theory is presented as it is the tool that will be used is this work. Then, a short review of the state-of-the-art on jet instabilities is presented. This review is necessary in order to interpret correctly the results that are obtained from the numerical linear stability analysis. A practical application of VESTA is then presented for the nominal case, that was defined in Sec. 2.4.2 (see Tab. 2.1). This analysis will be used to illustrate the different features introduced in the review on instability and it will serve to pose the limit of the sensitivity analysis and uncertainty quantification that will be made in the next chapter.

3.1 Hydrodynamic Instabilities

Hydrodynamic stability theory is concerned with the response of a laminar flow to a disturbance of small or moderate amplitude. If the flow returns to its original laminar state (the disturbance is damped) then the flow is defined as stable, whereas if the disturbance grows and causes the laminar flow to change into a different state (that can be a more complex laminar state or a turbulent state), then the flow is said to be unstable. Stability theory deals with the mathematical analysis of the superposition of many disturbances on the laminar base flow.

3.1.1 Interest of stability analysis

The solution obtained from COOLFLUID for particular operating conditions in the VKI plasmatron gives us a steady state solution of the plasma jet. We saw that in the VKI Plasmatron the flow field had some oscillations in space which could not be predicted by the steady numerical simulation. The exact results of the Navier-Stokes equations coule be obtained, for example by Direct-Numerical-Simulation. However, this would be very painful and computationally expensive.

It is therefore useful to investigate the unsteady features of the flow by means of stability analysis. It is natural to investigate the solution of the dynamic equations of the laminar flow of the real fluid motion to small disturbances. Small disturbances of the motion, that are always present, must be damped in time or space so as to not change the general nature of the flow. In the other case, when small disturbances increase in time or space, the motion deviates considerably from its original solution. It is therefore desirable to derive conditions for instability of a fluid. Methods for finding such conditions are the objectives of the *hydrodynamic stability theory*.

The study of stability carried in this work does not aim in determining a critical parameters that described a transition from one laminar state to an other, but rather in determining the unstable modes (i.e. the particular disturbances) that are inherent parts of the mean flow that is investigated. The modes thus obtained can show us if the flow field is stable on unstable, and in the latter case it will show us the different modes that are actually amplified in the plasma jet flow. We would like therefore to know to which disturbance this behaviour can be related to.

One of the objective of the stability analysis of the plasma jet was first to confront the experimental observations with the numerical ones. Thus, numerical simulations of the mean flow plus the linear stability analysis could be used to predict the overall behaviour of the jet generated inside the Plasmatron. Going further, by understanding the mechanisms of formation of the different modes of instability, we would be able to control them and even remove them.

3.2 Linear stability theory

The simplest means of investigating hydrodynamic stability is the general method of small disturbances. In this case we assume the disturbances to have small amplitudes so that many simplifications on the basic equations can be made. As the general Navier-Stokes equations are non-linear, the linear equations can fail to predict accurately the evolution of the disturbance after the amplitude reached a certain value above the basic flow. However, the linear stability theory is very useful for detecting physical growth mechanism and identifying dominant disturbance type.

The basic idea of the method is to write the flow field as the sum of a *mean* part and a *perturbed* part, the latter being small compared to the mean flow. Considering a generic flow variables Φ, like the velocity or the pressure, the instantaneous variable can be written as

$$\Phi = \overline{\Phi} + \phi'. \tag{3.1}$$

Inserting this decomposition in the Navier-Stokes equations and developing all the products, a set of second order equations in the disturbances is obtained. Then, the Linear Stability Theory (LST) consists of linearising these equations by neglecting the second order terms as the fluctuating quantities are assumed to be very small. The mean flow is also supposed to satisfy Navier-Stokes equations and these terms therefore cancelled out. The only remaining terms are the perturbation ones and the problem can be stated as an homogeneous eigenvalue problem

$$\mathbf{L}\phi' = 0, \tag{3.2}$$

where $\mathbf{L}$ is a linear operator including both the linearized Navier-Stokes equations and the boundary conditions. Eq. 3.2 admits the trivial solution $\phi' = 0$ for which the mean flow is retrieved. Other non-trivial solutions of Eq. 3.2 will give the expression for the perturbations. Either the perturbation will grow in space or time and therefore is said to be unstable either it will be damped and the perturbation is said to be stable. However this equation seems to encounter mathematical difficulties for flow in tubes, boundary layers on solid bodies or jets [37]. Two more assumptions can therefore be introduced in the LST, namely the *Parallel Flow Hypothesis*, which is related to the mean flow, and the *Modal Decomposition*, which is related to the perturbations. The decomposition of the solution in different modes is also called the *Method of Normal Modes*.

3.2.1 Parallel flow hypothesis

LST considers the flow to be particularly simple, namely not depending on the streamwise component z but only on the radial component r. While channel or pipe flow correspond exactly to this representation (in established flow), it is only approximated for boundary layer and for jet flows. The collapse of the potential core in the case of free jets is the prove that these flows are only approximative parallel flows. However, as Michalke proposes, in order to investigate round jet instabilities, it is acceptable to assume that the basic jet flow is parallel, meaning that the jet velocity vector $\boldsymbol{u}$ has only as non zero component the streamwise velocity w and that the mean variables depend only on the radial direction r, *i.e.* $\bar{w} = \bar{w}(r)$ [27]. Indeed, as already said, jets are slender structures where characteristic lengths are greater in the streamwise direction than in the radial direction ($l_z >> l_r$) resulting in much stronger gradients in the radial direction. Therefore, the parallel flow hypothesis will be assumed to be valid locally. In means that the analysis at a particular section in the jet will not be representative of the whole jet. It is also worth to note that jet instability with swirling velocity $V(r) \neq 0$ could be investigated but it is not the aim of this project. Therefore, in the case of boundary layer of free jet study, the *parallel flow assumption* where the jet is treated as *locally parallel* is introduced.

3.2.2 Modal decomposition

So far nothing has been said about the nature of the disturbances that are investigated. The modal decomposition consists of assuming that each fluctuating quantity ϕ' propagates independently from each other and has the following general form:

$$\phi' = \widetilde{\phi}(r) \exp\left(i(\alpha z + q\theta - \omega t)\right) + c.c. \tag{3.3}$$

where "*c.c*" stands for complex conjugate. This expression is equivalent to say that we are interesting in wave-like solution of disturbances. There exists a lot of different shape for the fluctuating quantity (dirac, rectangle, ...) but the expression in Eq. 3.3 is the most used as many simplifications can be made further with little loss of generality.

3.2.3 Temporal and spatial analysis

The wavenumber α and the angular frequency ω are generally belonging to $\mathbb{C}$. Azimuthal wave number can only be real number, as an azimuthal growth rate is not possible. Moreover, it will take only integer values as $\theta \in [0, 2\pi]$.

Depending on the complex nature of either α or ω, two cases are considered.

Temporal amplification theory

In this case, angular frequency ω is complex and α is real. Decomposing ω in its real and imaginary part, *i.e* $\omega = \omega_{\mathcal{R}} + i\omega_{\mathcal{I}}$, Eq. 3.3 can be rewritten as

$$\phi' = \widetilde{\phi}(r) \exp(\omega_{\mathcal{R}} t) \exp(i(\alpha z + q\theta - \omega_{\mathcal{I}} t)) \tag{3.4}$$

One see that the real part of omega is related to the temporal amplification of the disturbance. When $\omega_{\mathcal{R}}$ is positive, the mode is stable. On the contrary, when $\omega_{\mathcal{R}}$ is negative, the mode is unstable. The imaginary part is linked to the temporal frequency of the mode (its oscillating behaviour). The case of a temporally growing disturbance is represented in Fig. 3.1a

Spatial amplification theory

In this case, the streamwise wavenumber α is complex and the angular frequency ω is real. Once again, we consider the decomposition $\alpha = \alpha_{\mathcal{R}} + i\alpha_{\mathcal{I}}$ and the modal decomposition reads as

$$\phi' = \widetilde{\phi}(r) \exp(-\alpha_{\mathcal{I}} z) \exp(i(\alpha_{\mathcal{R}} z + q\theta - \omega t)) \tag{3.5}$$

Here, $\alpha_{\mathcal{I}}$ is the spatial growth rate. The mode will be amplified if $\alpha_{\mathcal{I}}$ is negative and it will be stable if $\alpha_{\mathcal{I}}$ is positive (it was the opposite for ω). Later in the document, the quantity $-\alpha_I$ will be often used. The real part of α is linked to the phase speed of the mode, as $c_{ph} = \omega/\alpha_{\mathcal{R}}$. The case of a spatially growing disturbance is represented in Fig. 3.1b.

From the previous discussion, we see that the spatial theory will correspond more to the physics of the plasma jet inside the VKI plasmatron. Indeed, we are looking at disturbances that are triggered inside the ICP torch (or somewhere inside the jet) and its behaviour (stable or unstable) when they are convected downstream is tracked. It corresponds therefore to the case represented in Fig. 3.1b and thus to the spatial theory. The case of temporal theory would be seek if the initial disturbance were present in the whole jet initially.

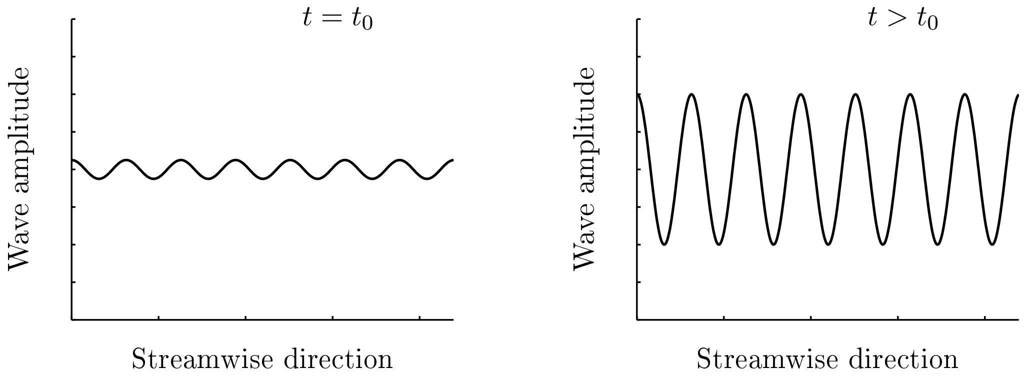

(a) Temporal evolution of a disturbance

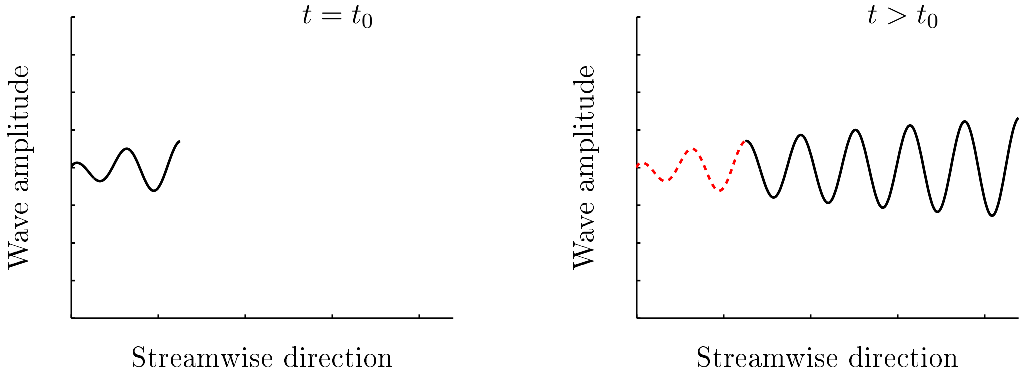

(b) Spatial evolution of a disturbance

Figure 3.1: Comparison of the evolution of a disturbance using (a) temporal analysis and (b) spatial analysis. In the spatial theory, initial disturbance at $t > t_0$ is represented in dotted line (– –).

3.3 Jet instabilities

Instabilities in jet flows have been widely investigated in the past for their great interest in noise generation in supersonic jets [33][34] and in more recent applications as jet-like galactic structures [11]. It is still of great interest in many domains and a state-of-the-art on findings on jet instabilities needs to be first done before the application to the VKI Plasmatron jet plasma.

In previous studies, two types of instability modes have been found: *vortical* and *acoustic* modes. The vortical mode is the generalisation of the Kelvin-Helmholtz instability for compressible flow. The term “vortical” refers to the origin of the instability that is generated when there is strong vorticity in the flow field, i.e. inside the shear layer. A large review of findings on vortical mode instability for different flow configuration has been given by Michalke [27]. The acoustic mode instability was first discovered by Mack in compressible boundary layers and by Gill in jets and wakes [23][13].

Vortical mode

Vortical mode is the extension to the compressible regime of the Kelvin-Helmholtz instability. Therefore, the mechanism that generates this type of mode is the same. Fig. 3.2 represents the formation of a one dimensional instability wave based on the Ackeret’s explanation [34].

First a vortex sheet is deformed by a small perturbation in a sinusoidal wave with phase speed c_{ph}, as shown in Fig. 3.2a. Ackeret suggested that one should view the flow not in the stationary frame of reference but with a frame of reference moving with the travelling wave with phase velocity c_{ph}. In this new frame of reference, the flow is as shown in Fig. 3.2b. Now assuming the flow is in a quasi-steady approximation, one should view it as a flow past a wavy-wall. At subsonic jet Mach number for the jet and the phase speed in the moving frame of reference, pressure is lowest at crests of the wavy-wall and highest at the troughs. Since the crests and the troughs interchange on the two sides of the vortex sheet the result is that a net pressure imbalance would exist across the thin mixing layer in the quasi-steady approximation. The pressure imbalance is in phase with the vortex sheet displacement and hence would tend to increase its amplitude leading to the well known Kelvin-Helmholtz instability.

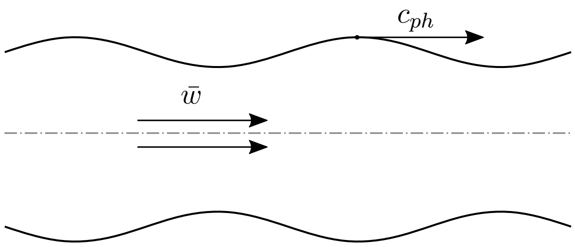

(a) Stationnary frame of reference.

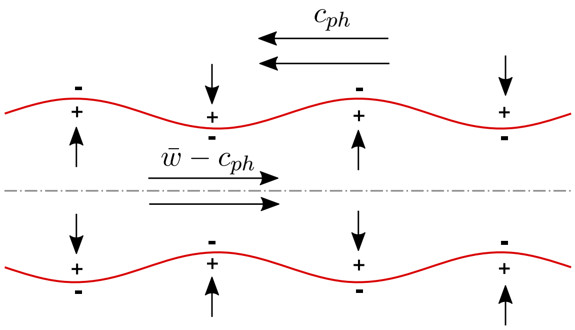

(b) Wave frame of reference.

Figure 3.2: Kelvin-Helmholtz instability mechanism at subsonic Mach number. The plus and minus signs denote high and low pressure regions respectively.

For supersonic velocities on the two sides of the wavy-wall, the phenomenon is slightly different. In this case, the pressure distribution along the wall is no longer in phase but rather 90 degrees out of phase. This results in identical pressure in both side of the vortex sheet and gives rise to neutral waves (or neutrally stable waves) that are neither amplified nor damped.

Considering the case of the jet, the existence of this kind of mode can be easily considered. Jet flows are characterized by strong gradient in the velocity field in the shear layer.

Acoustic mode

The acoustic mode refers to the sound wave than can be reflected back and forth between the wall and the sonic line, for boundary layer, and between the boundaries of the cylindrical vortex sheet for the jet, as represented in Fig. 3.3. As sound wave are convected with the flow, it is necessary to introduce the notion of relative Mach number, for both the jet and the ambient fluid. They are defined in cylindrical coordinates as follows [34]:

$$M^r_{cl} = M_{cl}\cos\phi\left(\bar{w}_{cl} - \frac{c_{ph}}{\cos\phi}\right), \tag{3.6}$$

$$M^r_{\infty} = \frac{M_{cl}}{\sqrt{\bar{T}_{\infty}}}\cos\phi\left(\frac{c_{ph}}{\cos\phi} - \bar{w}_{\infty}\right) \tag{3.7}$$

where $\phi = \alpha/(\alpha^2+q^2/r^2)^{1/2}$. The superscript r stands for *relative*, and subscripts cl and ∞ stand for centerline and ambient value respectively. By definition, a relative Mach number is a wave Mach number in the direction of the wave travelling at an angle ϕ relative to the z-axis with phase speed

$$c_{ph} = \frac{\omega}{\alpha}. \tag{3.8}$$

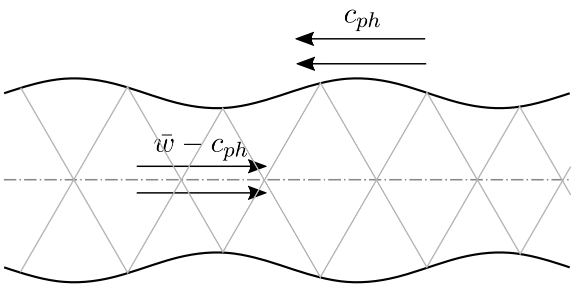

Figure 3.3: Pictorial representation of an acoustic mode inside a round jet with reflecting acoustic disturbances.

From this pictorial representation of acoustic modes, it seems obvious that the pressure disturbance of an acoustic wave is basically confined *within* the jet. The condition under which such a Mach wave system can exist is that in the wave frame of reference, the flow inside the jet is supersonic [34]. This condition is often referred as to the Mack's criterion, which can be stated as follows: *"acoustic modes exist whenever there is an embedded region of locally supersonic flow relative to the phase speed of the instability wave"*. Therefore, an acoustic mode will correspond to $M_{r1} > 1$. Relative Mach number is therefore a very practical tool for identifying the nature of the mode.

It is also useful to distinguish modes that have subsonic and supersonic relative Mach numbers to the ambient (Eq. 3.7). A mode for which $M^r_{\infty} < 1$, *i.e.* it is subsonic to the ambient fluid, is said to be non-radiating. The pressure disturbance of these modes are confined strictly inside de jet. On the contrary, modes with $M^r_{\infty} > 1$ are called radiating modes as their pressure disturbance dynamic can be showed to extend far away from the jet.

3.4 Vesta Toolkit

A brief description of the Vesta toolkit is given in this section. The differential linear stability equations for the Navier-Stokes systems are solved by means of a pseudo-spectral Chebyshev collocation methods. The development of the methodology implemented in Vesta can be found in [29]. The inputs parameters required for a single computation a presented and the different steps for the calculation of the linear stability analysis of the plasma jet are described.

3.4.1 Input parameters

When creating a test case, several inputs need to be provided to Vesta. These inputs concern:

- the mean flow variables,
- transport and thermodynamic properties,
- adimensional numbers,
- modal and discretization parameters.

The first two set of inputs can be obtained from numerical simulations or they can be provided from direct experimental measurements. The CooLFluiD solver and the Mutation library are used to compute mean flow fields and flow properties respectively. Characteristic scales for the adimensional number are all considered at the centerline of the jet. For the length scale, the choice of the nozzle radius is adopted. Finally, a set of modal inputs, coming from the modal decomposition Eq. 3.3, and numerical parameters used by Vesta for the discretization of the physical domain, must be provided. Tab. 3.1 summarizes all the parameters that the user must provide to Vesta for a single test case. Note that all the flow variables and properties are mean values and are must provided in dimensionless form. All the test cases will be solved using discretization parameters as well

Vesta input parameters	Notation
Streamwise velocity profile and its derivatives	w, w_r, w_{rr}
Azimuthal velocity profile and its first derivative	v, v_r
Temperature profile and its first derivative	T, T_r
Pressure profile and its first derivative	p, p_T
Computational domain (radial coordinate)	r
Dynamic viscosity profile, its first and second derivatives	μ, μ_T, μ_{TT}, μ_P, μ_{PP}, μ_{PT}
Second viscosity coefficient profile and its derivatives	λ, λ_T, λ_{TT}, λ_P, λ_{PP}, λ_{PT}
Thermal conductivity profile and its derivatives	k, k_t, k_{TT}, k_P, k_{PP}, k_{PT}
Enthalpy profile	h, h_T, h_{TT}, h_P, h_{PP}, h_{PT}
Compressibility factor profile and its derivatives	ζ, ζ_T, ζ_{TT}, ζ_P, ζ_{PP}, ζ_{PT}
F and G parameters	F, G
Reynolds number	Re
Mach number	M
Prandtl number	Pr
Eckert number	Ec
H number	H
Azimuhtal wavenumber	q
Frequency or streamwise wave number	ω or α
Number of collocation points	N
Mapping parameter	r_i

Table 3.1: Input parameters for the LTE solver of Vesta in cylindrical coordinates.

	N	r_i	q
Value	220	1.5	0

Table 3.2: Values of the discretization parameters of VESTA and azimuthal wavenumber.

as azimuthal wave number fixed. Their value are given in Tab. 3.2. Parameters N and r_i were discussed in the work of Garcìa Rubio and their value are such that the stability of the jet is independent of the boundary conditions used. The choice of a fixed value of q is for simplicity reasons. It means that only axisymmetric perturbation waves will be sought. Note that stability of the jet for different values of q could also be investigated.

3.4.2 Generation of analytic profiles

Mean streamwise velocity and temperature profiles are obtained from numerical simulations coming from COOLFLUID for which we extracted data at a particular position inside the jet (Sec. 2.4.2). However, convergence rate of spectral methods depends strongly on the regularity of the functions that have to be differentiated. Therefore, both mean streamwise velocity and temperature profiles, after being extracted, will be fitted to analytical functions in order to ensure sufficiently high regularity in the functions and their derivatives.

Following the methodology applied in previous studies on the stability of the plasma jet, we will assume that $\bar{w}$ and $\bar{T}$ can be expressed as the sum of some base functions. We consider the following Gaussian and hyperbolic tri-parametrized functions

$$f_{\text{Gauss}}(r; a, \mu, \sigma) = \frac{a}{\sigma\sqrt{2\pi}} \exp\left(-\frac{(r-\mu)^2}{\sigma^2}\right), \tag{3.9}$$

$$f_{\tanh}(r; b, c, d) = b\left(1 - \tanh\left(c(r-d)\right)\right), \tag{3.10}$$

as base functions, where a, μ, and σ are the parameters of the Gaussian curve (μ and σ are the mean and standard deviation respectively, while a is an amplitude parameter), and b, c, d the parameters for the hyperbolic tangent function. This choice of base functions can be easily motivated by the general shape of free jet flows, as discussed in Sec. 2.4.1. Free jets approach an hyperbolic tangent function in the potential core region and converge to a bell-shaped function in the fully-developed region. Therefore, it would be reasonable to think that the mean velocity profile can be described by a combination of these kind of functions. Hyperbolic tangent can represent strong gradient. The choice of the Gaussian curve is then motivated by the fact that it admits a zero derivative at $r = \mu$ which is interesting for reproducing the profiles near the centerline of the jet.

We then assume that the mean streamwise and temperature profile express as

$$\begin{aligned} \bar{w} =& f_{\text{Gauss}}(r; a_{1w}, \mu_{1w}, \sigma_{1w}) + f_{\tanh}(r; b_w, c_w, d_w) \\ &+ f_{\text{Gauss}}(r; a_{2w}, \mu_{2w}, \sigma_{2w}) + f_{\text{Gauss}}(r; a_{3w}, \mu_{3w}, \sigma_{3w}), \end{aligned} \tag{3.11}$$

$$\begin{aligned} \bar{T} =& f_{\text{Gauss}}(r; a_T, \mu_T, \sigma_T) + f_{\tanh}(r; b_{1T}, c_{1T}, d_{1T}) \\ &+ f_{\tanh}(r; b_{2T}, c_{2T}, d_{2T}) + h_T. \end{aligned} \tag{3.12}$$

$\bar{w}$ is thus a function of 12 parameters while $\bar{T}$ is a function of 10 parameters. The fourth term in Eq. 3.11 has been added, compared to previous studies, in order to catch correctly the fact that $\bar{w}(r = 0) = 1$ The number of terms in the expression of the fitted profiles depends mainly on the shape of the profile. Regularity of both Gaussian curve and hyperbolic tangent allows us to compute their derivatives analytically using the same set of parameters. Parameters of the function in Eqs. (3.11) and (3.12) are determined by a regression fitting of the analytical profile on the CFD profiles in a least-square sense. This optimization problem is directly solved in `Matlab` and is therefore not discussed here. The parameters obtained for the fitting of the nominal case are summarized in Tab. 3.3. In this

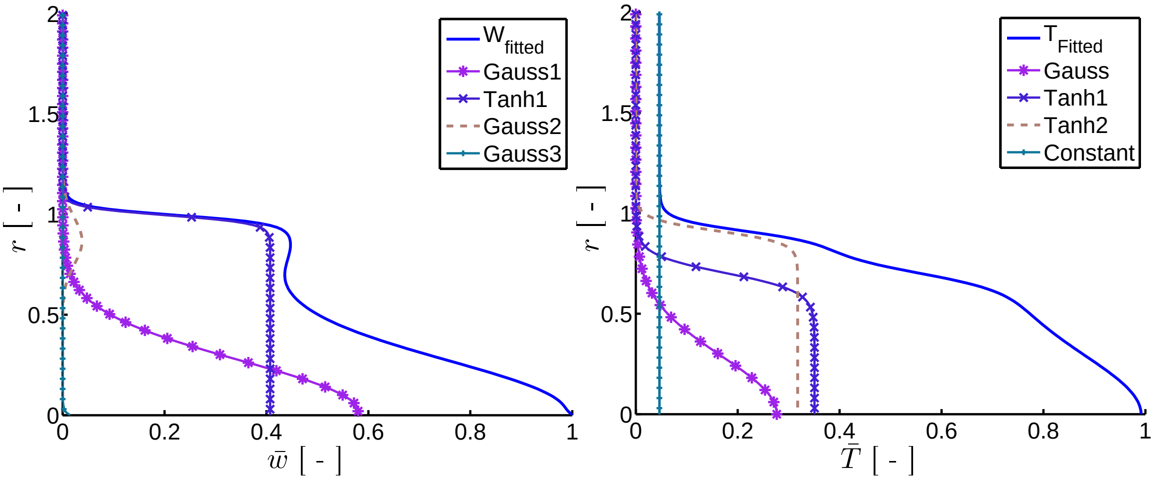

(a) Mean streamwise velocity profile

(b) Mean temperature profile

Figure 3.4: Mean streamwise velocity and mean temperature profiles after the fitting process and their components.

Parameter	Value
a_{1w}	0.383460
μ_{1w}	0.009466
σ_{1w}	0.259274
b_w	0.201468
c_w	25.062732
d_w	0.995030
a_{2w}	0.012325
μ_{2w}	0.863672
σ_{2w}	0.117673
a_{3w}	10.567959
μ_{3w}	-2.379240
σ_{3w}	0.3869191

(a) Mean streamwise velocity

Parameter	Value
a_T	0.201040
μ_T	0
σ_T	0.289825
b_{1T}	0.175395
c_{1T}	10.973974
d_{1T}	0.158824
b_{2T}	16.769290
c_{2T}	0.912363
d_{2T}	0.046437
h_T	10.567959

(b) Mean temperature

Table 3.3: Parameters of the analytical fitting for the mean velocity and temperature profiles.

case, the obtained residual mean square distance between correct and analytical profiles are 0.000833 and 0.001463 respectively for velocity and temperature profiles. Graphical results for the fitting of the nominal case are presented in Fig. 3.4, where the different terms that composed the profiles are represented.

This fitting procedure is applied each time a profile has been extracted from COOLFLUID. Once a set of fitted parameters is available for a profile, these ones can be used as initial guess for the optimization problem for other profile. In Sec. 4.2 on the uncertainty quantification, several profiles at different electric power P_{fl} will be generated and the fitting process will be achieved in a very automatic way using each time the fitted parameters of the closest profiles. The only requirement is that input data must be close enough for the fitting to converge toward a correct minimum[1].

Finally, note that the jet properties presented in Fig. 2.15 were computed for the fitted temperature profile. It was not explicitely specified at that time to not confuse the

---

[1] Think of the least-square problem as the search of a local minimum of a high-dimension function in the set of parameters. Many local minima exist and this is why initial guess must not be to far from an acceptable solution.

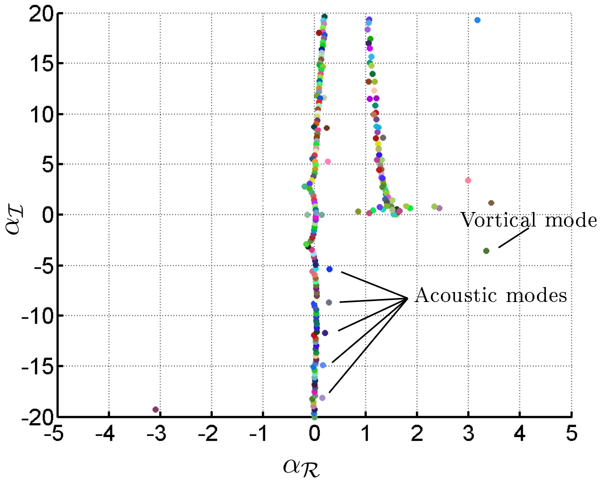

Figure 3.5: Spectrum of the linearized operator of the nominal case with modal parameters $\omega = 0.7$ and $q = 0$.

reader with the fitting process. Results are exactly the same using directly the profile from CooLFluiD as both analytical and numerical profiles are closed to each other.

3.5 Numerical Results from Vesta

It this section, the results obtained from Vesta for the nominal case are presented. A brief discussion of the main features of the spectrum and the eigengfunctions of unstable mode are given. In particular, a vortical mode and several acoustic modes can be identified in the spectrum. Then the influence of the frequency related of the instabilites is discussed on the vortical mode. This example will be useful for the definition of the quantities of interests that will be used in the next chapter.

3.5.1 Spectrum of the linearized operator

The spectrum of the nominal case computed with Vesta is presented in Fig. 3.5. First we notice that, according to Eq. 3.3, the part of the spectrum for which $\alpha_{\mathcal{I}}$ is greater than zero constitutes the stable part while the part for which $\alpha_{\mathcal{R}}$ is lower than zero constitues the unstable part. Stable part is not of interest in this study. Modes for which $\alpha_{\mathcal{R}} < 0$ are modes that propagate upstream the jet, i.e. toward the nozzle and do not interest us as well.

There are two main branches that can be identified in the spectrum. The first branch, located near $\alpha_{\mathcal{R}} = 0$ is part of the continuous spectrum[2]. These are modes that propagate at very high phase speed. Most of them have their eigenfunction dynamic that takes place outside the jet and is not interesting in this case. These radiating modes however appear to be much more efficient in noise generation and could be of interest considering this kind of problems [22]. Others mode in the unsable continuous part have a highly oscillating behaviour and are not likely to be excited. The second branch, located between $\alpha_{\mathcal{R}} = 1$ and $\alpha_{\mathcal{R}} = 2$ constitutes the stable continuous spectrum which of interest here.

We are interested mainly in the set of modes that constitutes the discrete part of the spectrum, which are analysed below. It is possible to investigate separately the eigenfunctions of the set of perturbations for each mode that is present in the spectrum. Looking at the modes that are of interest, both vortical and acoustic mode instabilities are found

---

[2] Be careful to not confuse the discretization of the continuous spectrum with the discrete part of the spectrum. The first is due to the discretization inherent to all numerical methods. Ideally, for a infinite number of points, the continuous branches can be recovered.

for this profile. This is in agreement with the theory of the instability modes that can be found in round jets. The eigenfunctions of modes that lies in the unstable discrete part of the spectrum are presented in Fig. 3.6. Note that the radial direction is represented in the domain $[0, 2]$ only for graphical purpose, but we should keep in mind that the stability analysis was made on a domain up to ten times the jet radius.

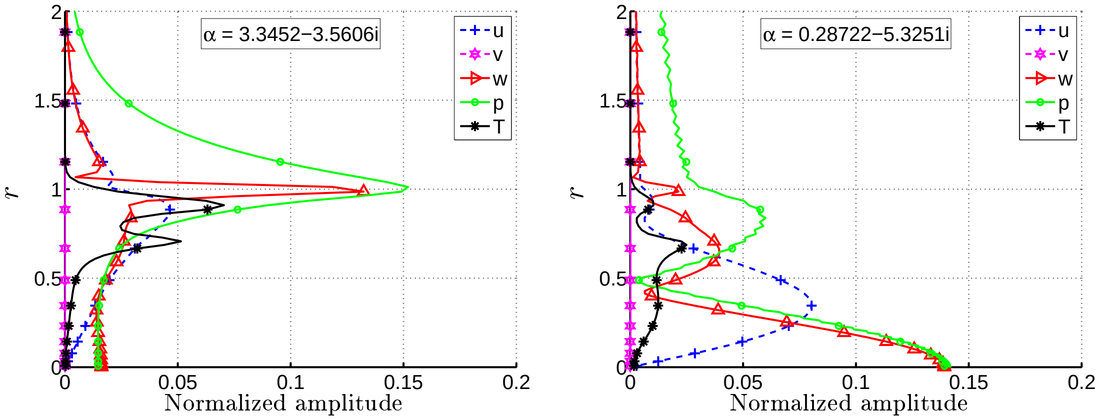

(a) Vortical mode $(0, 0)$ (b) First acoustic mode $(0, 2)$

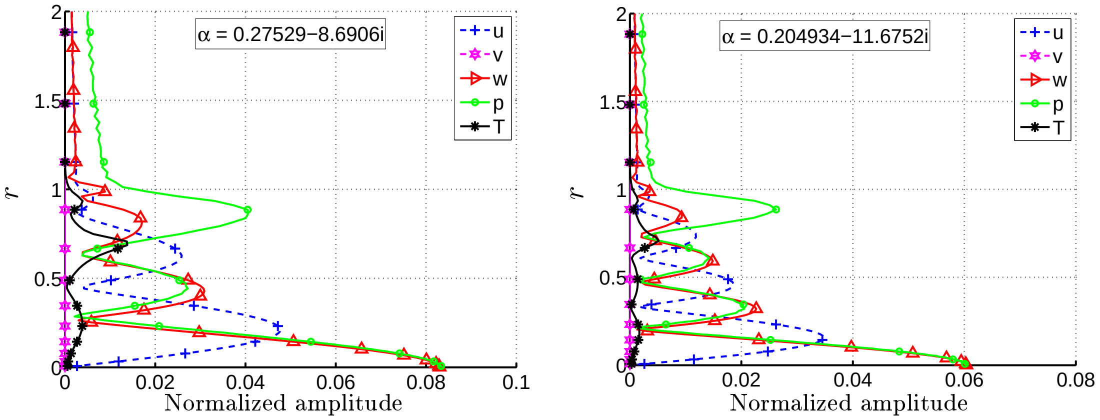

(c) Second acoustic mode $(0, 3)$ (d) Third acoustic mode $(0, 4)$

Figure 3.6: Eigenfunctions of the perturbations for the vortical mode and the three first acoustic modes for the nominal case with modal parameters $\omega = 0.7$ and $q = 0$.

In Fig. 3.6a, a maximum is observed in the pressure and streamwise velocity distributions of the wave at a distance $r = 1$, which corresponds to the radius of the nozzle. This is where there strong velocity gradients occur and the mode has the features of a vortical mode described previously. For this mode, we have $M_{r1} < 1$ confirming the vortical nature of the mode. It will be called the vortical mode. Eigenfunctions for the other discrete modes close to the continuous spectrum are presented in Figs. 3.6b, 3.6c and 3.6d. For convenience of discussion, we will refer to a particular mode by an integer pair (q, m). Thus, mode (q, m) has an azimuthal wavenumber q $(q = 0, 1, 2 \ldots)$ and a radial mode number m $(m = 0, 1, 2 \ldots)$ characterizing the number of anti-nodes (maximum oscillation points[3]) in the pressure distribution of the wave in the radial direction [34]. The mode $(0, 1)$ is not observed in this case and the mode $(0, 0)$ can be used unambiguously to denote the vortical mode. The number of anti-nodes is well defined in the pressure distribution of the wave so that each acoustic modes can be assign a unique pair (q, m). For axisymmetric modes $(q \neq 0)$, the first anti-nodes is located at the center of the jet. Note that for helical waves (not investigated in this work), the pressure wave is zero at the centerline (this is a

---

[3] Minimum of oscillation point are called quasi-nodes, as they are not necessarily equal to zero

direct consequence of the boundary conditions for $q \geq 1$). However, these modes are not really acoustic modes as their are found to have their relative Mach number $M^r_{cl} < 1$, which would corresponds to a vortical mode. However, their pressure distrubance eigenfunction have all the characteristics of acoustic modes, and they will be referred to (pseudo-)acoustic modes. The denomination "first acoustic mode", "second acoustic mode", etc, refers to the apparition of the mode in the spectrum and not on the radial number. Note that for each mode represented in Fig. 3.6, the eigenfunction of the azimuthal velocity disturbance is null.

It is generally assumed in linear stability theory that the mode that will be observed is the mode that is the most amplified amongst all others. Acoustic modes are therefore better candidates for determining which ones are predominant.

3.5.2 Growth rate and phase speed as a function of frequency

The representation of the spectrum in Fig. 3.5 is only for one particular dimensionless angular frequency ω and one azimuthal wavenumber q. For a complete flow stability analysis, the spectrum should be computed for every value of the couple of variables (ω, q). This methodology is of course very expensive from a computational point of view and is not very efficient as all the complex values of α are not of interest. For this purpose, an other branch of VESTA was also developed for following a particular mode when one or several input parameters are modified. This solver is called the *local* solver, in contrast with the previous *global* solver used for the computation of the whole spectrum at once. The local solver uses the value of the mode investigated coming from a preliminary resolution of the whole spectrum as initial guess for converging toward the new value of the mode when input parameters are varied. The variation in the input(s) parameter(s) must not be signification in order to ensure the convergence to the correct mode.

The case of helical mode, i.e. with $q \neq 0$ is not investigated in this work. However, the dimensionless angular frequency ω is allowed to vary. The local solver of VESTA is therefore used in order to follow the vortical mode when ω is modified. The range of frequency that will be sweep each time is $\omega \in [0, 4]$, as for frequencies greater than 4, the vortical mode tends to be stable. Numerical results for the growth rate and phase speed obtained as function of frequency for the nominal case are shown in Fig. 3.7. The growth rate in Fig. 3.7a ($-\alpha_{\mathcal{I}}$ is reresented) first increases with frequency. It has a destabilizing effect on the mode until it reaches a maximum. After the maximum, the growth rate starts decreasing and becomes more and more stable. The phase speed, represented in Fig. 3.7b is incredibly high at low frequencies. On the spectrum, the mode would be moving towards the the continuous branch near $\alpha_{\mathcal{R}} = 0$. When frequency increases, the mode moves away from the continuous line. This translates in very small oscillations in space and the phase speed is very slow. Note that when phase speed is low, the relative mach number would tend to increase and the mode could not be considered as a vortical mode anymore considering Mack's criterion.

The peak in the growth rate at $\omega = 1.870$ is very interesting concerning the instability of the jet. This frequency is called the *most amplified frequency*, as it is the frequency at which the maximum value of the growth rate is reached. Practically, this would be the oscillating frequency that would be observed in the Plasmatron if the vortical mode was the most unstable mode amongst others. Considering the growth rate as function of frequency, that is $\alpha_{\mathcal{I}} = \alpha_{\mathcal{I}}(\omega)$, the most amplified adimensional frequency is defined mathematically as

$$\arg\max_{\omega} \alpha_{\mathcal{I}}(\omega) := \{\omega \mid \forall \omega' \ : \alpha_{\mathcal{I}}(\omega') \leq \alpha_{\mathcal{I}}(\omega)\} \tag{3.13}$$

The adimensional modal parameters α and ω can be rescaled using the characteristic scales of the jet. For the jet, centerline velocity w_{cl} and temperature T_{cl} are used and R_{jet} is the length scale. The time scale is therefore $\tau = R_{jet}/w_{cl}$. Dimensional frequency f ([Hz]) and

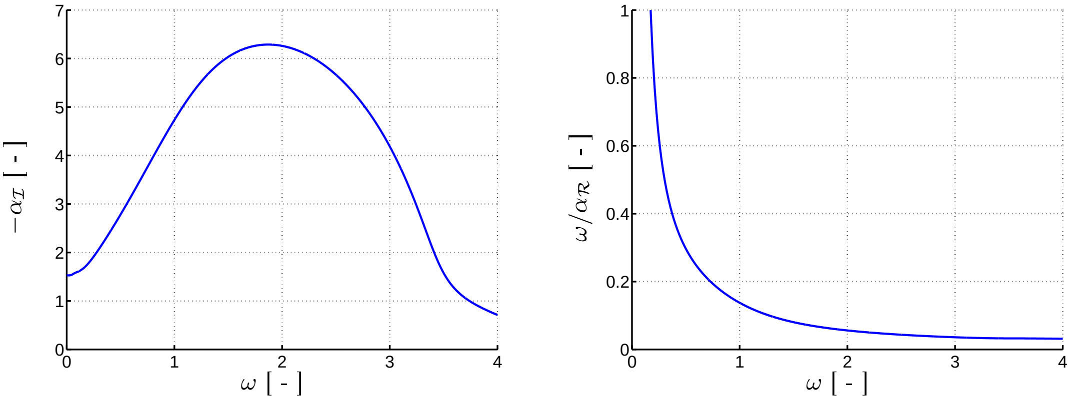

(a) Growth rate (b) Phase speed

Figure 3.7: (a) Non-dimensional growth rate and (b) phase speed as a function of frequency for the vortical mode for the nominal case.

wavelength $\lambda_{\mathcal{R}}$ ([m]) can be retrieved using the following rescaling

$$f = \frac{\omega}{2\pi\tau} = \frac{\omega w_{cl}}{2\pi R_{jet}} \tag{3.14}$$

$$\lambda_{\mathcal{R}} = \frac{2\pi}{\alpha_{\mathcal{R}}} \tag{3.15}$$

The most amplified frequency can be defined as well in dimensional form as

$$\arg\max_{f} \alpha_{\mathcal{I}}(f) := \{f \mid \forall f' \ : \alpha_{\mathcal{I}}(f') \leq \alpha_{\mathcal{I}}(f)\} \tag{3.16}$$

Using the transformation of Eq. 3.14, the most amplified frequency is found to be 294.88 [Hz]. These quantities for the characterization of the instability of a particular mode of the plasma jet will be used in Chapter 4 for the sensitivity analysis and the uncertainty quantification.

3.5.3 A note on earlier results and link with experiments in the Plasmatron

Two cases were considered so far in previous studies on plasma jet instabilities, namely the *low-pressure* and *high-pressure* case, presented in Tab. 3.4. These two cases were widely investigated in the work of Garcia-Rubio for a calorically perfect jet and in the work of Chiatto for the mixture in LTE [12][7].

	$\dot{m}$ [g/s]	p_{tc} [Pa]	P_{fl} [kW]	z_{jet} [m]	Fluid mixture
Low pressure case	16	20000	90	0.6	Air$_{11}$
High pressure case	16	1500	90	0.6	Air$_{11}$

Table 3.4: Parameters of the low pressure and high pressure cases.

These two cases have been investigated as their parameters were close to the experimental conditions used by Cipullo in his test campaign [8]. On the one hand, it has been possible to link the dimensional frequency of the first and second acoustic modes (see Tab. 3.5), fo the high-pressure case, to the experimental results of Cipullo. On the other hand, for the low-pressure, no experimental verification could be made.

For future reference, it seems useful to mention a slight correction that has been added to the results from previous studies. It seems that in the work of Chiatto, the value of the specific gas constant for air at sea-level was misinterpreted and a value of $R_0 = 512$

was assigned. It was recomputed here with the correct value $R_0 = 287$ [J/(kg K)]. The results are compared in Tab. 3.5. The two results are closed and the conclusion made in the previous study remain valid. For the comparison of growth rate and phase speed with other input parameters, they have been investigated for vortical and acoustic modes at two different pressure and for different azimuthal wavenumber by Garcìa Rubio for the cold jet and by Chiatto for the jet in LTE [12][7]. For both low and high pressure cases(1500 and 20000 [Pa] resp.), acoustic modes remain the most unstable. By contrast with vortical modes, which stabilizes for high frequencies, acoustic modes are still unstable for high frequencies.

	Chiatto [7]	Present study
Vortical mode	4.552 - 4.2954i	4.3932 - 4.2798i
1st acoustic mode	0.3016 - 5.0567i	0.3040 - 5.0235i
2nd acoustic mode	0.4149-8.2525i	0.4109 - 8.2233i

Table 3.5: Comparison of the values of vortical and acoustic modes obtained in previous studies with the values from the present study for the high-pressure case at $\omega = 0.7$ and $q = 0$.

3.6 Summary of the Chapter

The linear stability analysis of a high temperature jet was addressed. A state-of-the-art stability analysis of high temperature and high speed jets was briefly discussed. The stability of the plasma jet was then computed using the numerical code VESTA developed at the VKI for the numerical study of linear stability. Some features that were observed in previous studies on jet instabilities were retrieved and it was possible to observed two types of mode, namely the vortical and acoustic modes. The vortical mode is seen as an instability occurring in the shear layer due to a pressure imbalance. Acoustic modes is seen as acoustic waves reflecting back and forth inside the round jet.

Chapter 4

Sensitivity Analysis and Uncertainty Quantification

In this chapter, the two main research questions of the project are addressed. The first question that we would like to answer is how do the quantities of interest behave as we are going from the cold jet (the calorically perfect gas) model to the hot jet (or chemically reacting mixture of perfect gas under the LTE assumption) model and from which properties (thermodynamic and transport) originates the main contribution? The second question is concerned with the study of the stability of the jet when an input is considered uncertain. The input uncertainty studied in this work is the electric power transmitted to the plasma, as it is shown that this quantity may have a strong influence on the velocity and temperature profiles. These two last parameters are dominant in the stability of the plasma jet.

The whole process used for the complete stability analysis of the plasma jet is sketched in Fig. 4.1. In Chapter 2, we described the first set of input variables that are the transport and thermodynamic properties. The numerical simulation from the ICP CooLFluiD solver was presented for the nominal case. In Chapter 3, the fitting procedure used for obtaining the analytical velocity and temperature profiles from the CFD simulations was presented. The Vesta solver for the linear stability analysis was then described and the results for the nominal case were presented. From this, we identified two quantities of interest, the growth rate $\alpha_{\mathcal{I}}$ of the mode and the most amplified frequency $\arg\max_{\omega} \alpha_{\mathcal{I}}(\omega)$ defined as the frequency where the mode is the most unstable (i.e. with the highest growth rate).

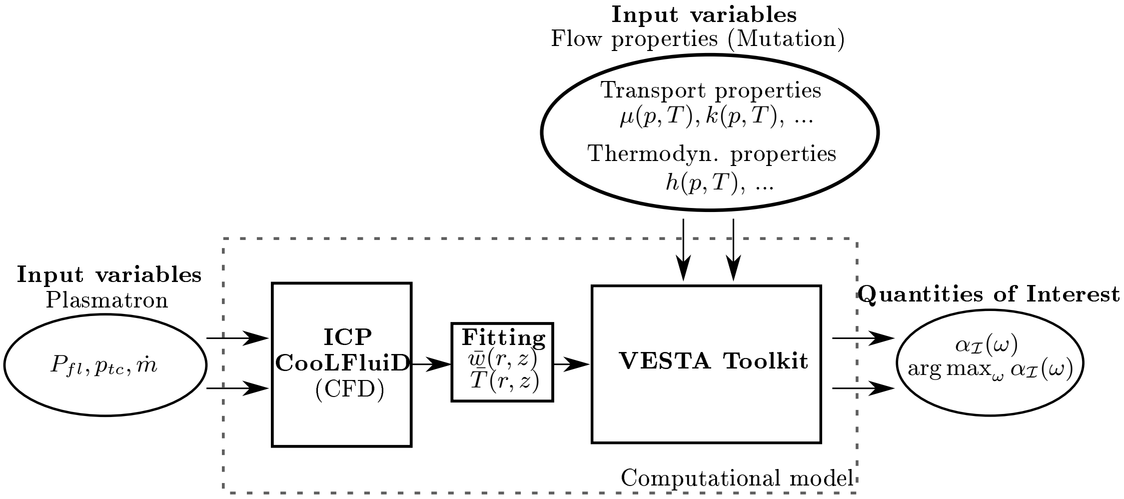

Figure 4.1: Computational model of the whole process for the stability analysis

The whole process, composed of the numerical simulations with the ICP CooLFluiD solver, the fitting process and the stability analysis using the Vesta toolkit, will be called the *computational model*. For the sensitivity analysis and the uncertainty quantification, this one will be considered as a black-box. The input variables are modified and the quantities of interest are observed, without any modification of the code. Proceeding this way, what happens "inside" the computational model is momentarily omitted.

In this chapter, the sensitivity of the two quantities of interest when the flow properties are modified is investigated. In Sec. 4.1, the notation used through this chapter is introduced. A superscript notation is introduced for the distinction of the different models used for computing the stability, each having a different set of input properties. In this analysis, the thermodynamic and transport properties of the mean flow are deliberately modified. The numerical results are then presented for the nominal case and the variation of the two quantities of interest when the model for the flow properties is changed are analysed. The vortical mode is first analysed for a fixed angular frequency ω. Then the sensitivity analysis is made when all the frequencies of the mode are investigated. Finally, the most amplified frequency is sought for each model and its variation is analysed.

In Sec. 4.2, a methodology for studying the stability of the plasma jet considering an uncertain input is addressed. The electric power transmitted to the plasma flow is assumed to vary from one simulation to the other, as the coupling between the generator of the Plasmatron and the plasma is not well defined. A stochastic collocation method is implemented for the uncertainty quantification and the results for the two quantities of interest are analysed. Again, vortical mode is first investigated at a fixed frequency. The same UQ analysis is then performed on all the frequency domain and finally the most amplified frequency is sought. For the uncertainty quantification analysis, new profiles from numerical simulations are needed as different electric power are considered (recall that the nominal case corresponded to $P_{fl} = 85$ [kW]). The UQ methodology is first developed using a few numbers of already available CFD simulations and interpolation between these profiles is made in order to obtain solutions at intermediate electric powers. A convergence analysis is then performed and the main features are presented using these approximate profiles. Secondly, new CFD are computed using the CooLFluiD solver. The number of profiles computed is based on the convergence analysis made on approximate profiles and for computational purpose. The solutions obtained for the accurate profiles are thus more accurate but a convergence analysis is made much more difficult to perform. Therefore, the two approaches will be presented. The second approach using the accurate CFD profile will be used to estimate the validity of the first one.

Finally, the sensitivity analysis made in Sec. 4.1 is recomputed assuming now that the input P_{fl} is uncertain, applying the methodology developed in Sec. 4.2 of this chapter.

4.1 Sensitivity analysis in the Nominal Case

In this first section, the properties of a calorically perfect gas are applied to the high temperature plasma jet and compared to the results for the jet under LTE hypothesis. This methodology is used in order to get some insight into the influence of the transport and thermodynamic properties of the flow on the stability of the jet.

4.1.1 Notation and description of the model used

The nominal case presented in previous chapters was computed using the correct thermodynamic and transport properties coming from the Mutation library. These are the properties for a Chemically Reacting mixture of perfect Gases, considering the air as an 11-species mixture under LTE. **This accurate model will be called the CRG model and it will be denoted by $\widehat{\textbf{CRG}}$**. On the contrary, we can introduce a fully incorrect model, for which all the thermodynamic and transport properties are described by the classical laws of thermodynamics and the Sutherland's laws described in Sec. 2.2. These are the properties of a Calorically Perfect Gas, which would correctly describe the behaviour of a cold jet (jet at low temperature). Using these properties for describing the plasma jet (a very hot jet) is of course misrepresenting the correct behaviour of the instabilities. **This inaccurate model will be called the CPG model and will be denoted by $\widehat{\textbf{CPG}}$**. We will note that, although the CPG model is using the inaccurate properties for the flow, the value of the quantity of interest, as the growth rate or the most amplified frequency, will remain close to the correct value of the CRG model. This is because the stability of the jet is mainly influenced by the mean streamwise velocity and temperature profiles that do not change from one model to an other, as they come from the CFD simulation of CooLFluiD. The methodology applied here is used to determine the property of the flow that is most influencing the stability of the jet when we are passing from the calorically perfect gas to the chemically reacting mixture of perfect gases under LTE assumption.

For this purpose, the CPG and the CRG model are used as references. Then, intermediate models are computed when modifying one or another parameter and the stability analysis is applied using Vesta. **We will denote an intermediate model by the property that has been modified with a "hat" superscript** for the computation of the stability spectrum. The "hat" notation is introduced to avoid any confusion between the model used and the physical property that is represented by the symbol itself without the "hat" superscript.

To illustrate the notation introduced, consider a model for which all transport and thermodynamic properties are computed with Mutation, except the dynamic viscosity. This model is noted $\hat{\mu}$. All the derivatives are also modified in consequence. The reader may refer to the Vesta input parameters table 3.1 for a better understanding. In the $\hat{\mu}$ model, we will assume that the whole "dynamic viscosity" line from the table will be computed using the corresponding calorically perfect gas law. For the dynamic viscosity, we saw that it was the Sutherland's law provided in Eq. 2.11. The derivatives of the Sutherland law are computed analytically.

Once the $\widehat{\text{CRG}}$, $\widehat{\text{CPG}}$ and intermediate models stability calculations are available, the variation of the quantity of interests with the reference $\widehat{\text{CRG}}$ model can be computed. The two quantities of interest, as defined in the introduction, are the growth rate and the most amplified frequency (both in dimensionless form unless specified). The growth rate, considering the spatial theory, is the imaginary part of the wavenumber (see. Eq. 3.3) with $\alpha = \alpha_{\mathcal{R}} + i\alpha_{\mathcal{I}}$. Imaginary and real parts are considered separately and the following distances can be defined

$$\Delta\alpha_{\mathcal{R}}^{\hat{\varphi}}(\omega) = \alpha_{\mathcal{R}}^{\widehat{\text{CRG}}}(\omega) - \alpha_{\mathcal{R}}^{\hat{\varphi}}(\omega)\,, \tag{4.1}$$

$$\Delta\alpha_{\mathcal{I}}^{\hat{\varphi}}(\omega) = \alpha_{\mathcal{I}}^{\widehat{\text{CRG}}}(\omega) - \alpha_{\mathcal{I}}^{\hat{\varphi}}(\omega)\,, \tag{4.2}$$

where $\hat{\varphi}$ denote a general model in which we modified some properties compared to the correct CRG model. For example, for the accurate $\widehat{\text{CRG}}$ model at $\omega = 0.7$, VESTA returns (for the first vortical mode) $\alpha^{\widehat{\text{CRG}}} = 3.3452 - i3.5606$ and for the inaccurate $\widehat{\text{CPG}}$ model $\alpha^{\widehat{\text{CPG}}} = 3.3172 - i3.6684$. The distances computed using Eqs. 4.1 and 4.2 are then $\Delta\alpha_{\mathcal{R}}(\omega = 0.7) = 0.028$ and $\Delta\alpha_{\mathcal{I}}(\omega = 0.7) = 0.1078$. From this consideration, notice first that the differences between the two models are quite low due to the fact that the same velocity and temperature profiles are used, as already said. Secondly, it can be deduced from the sign of $\Delta\alpha_{\mathcal{I}}$ if either the model has a stabilizing or a destabilizing effect on the instability considered. Here, we can say that, compared to the $\widehat{\text{CRG}}$ model, the $\widehat{\text{CPG}}$ model has a destabilizing effect on the model[1], which is in agreement with the previous work of Chiatto [7]. The same distance can be defined for the most amplified frequency

$$\Delta \arg\max_{\omega}(\alpha_{\mathcal{I}}^{\hat{\varphi}}) = \arg\max_{\omega}(\alpha_{\mathcal{I}}^{\widehat{\text{CRG}}}(\omega)) - \arg\max_{\omega}(\alpha_{\mathcal{I}}^{\hat{\varphi}}(\omega)) \tag{4.3}$$

For the sake of clarity, a set notation for enumerating the models is adopted:

- $\{\hat{\varphi}, \ldots, \hat{\varsigma}\}$ denotes a set of different models,
- $(\hat{\varphi}, \hat{\varsigma}) = \hat{\varphi} \cup \hat{\varsigma}$ is the model obtained from the union of a couple of models,
- $\varnothing$ is the null ensemble.

We consider the following set of models for the analysis: $\hat{\chi} = \{\hat{\mu}, \hat{k}, \hat{\lambda}, \hat{h}, \hat{\rho}, \hat{\zeta}\}$. Amongst them, there are also the two reference models, namely $\widehat{\text{CRG}}$ and $\widehat{\text{CPG}}$. Note that $\widehat{\text{CPG}} = (\hat{\mu}, \hat{k}, \hat{\lambda}, \hat{h}, \hat{\rho}, \hat{\zeta})$ and that $\widehat{\text{CRG}} = \varnothing$, i.e. no properties have been modified. It is also possible to define a subset of each model in $\hat{\chi}$ in which the zero order and the higher derivatives of the parameter considered are modified independently. For example, for ζ, the following set of models can be defined: $\{\hat{\zeta}_0, \hat{\zeta}_P, \hat{\zeta}_{PP}, \hat{\zeta}_T, \hat{\zeta}_{TT}, \hat{\zeta}_{PT}\}$. Of course, we have $\hat{\zeta} = (\hat{\zeta}_0, \hat{\zeta}_P, \hat{\zeta}_{PP}, \hat{\zeta}_T, \hat{\zeta}_{TT}, \hat{\zeta}_{PT}) = \cup_i \hat{\zeta}_i$.

4.1.2 Results of the sensitivity analysis on the nominal case

The distance between two values of both the growth rate $\alpha_{\mathcal{I}}$ and $\alpha_{\mathcal{R}}$ for the first vortical mode are computed for different models. In this first analysis, the differences between models are made for a fixed adimensional angular frequency $\omega = 0.7$.

For any combination of the model in $\hat{\chi}$, the corresponding properties and their derivatives are changed accordingly. Note that modifying a certain property can have an influence on the adimensional numbers and other parameters that are needed for the computation of the spectrum (Tab. 3.1). For example, the parameters F and G are related to the derivatives of ζ, as shown in Appendix B.1 and they need to be changed accordingly when the model $\hat{\zeta}$ is considered. Results for the six one-parameter models of $\hat{\chi}$ and the $\widehat{\text{CPG}}$ model, compared to the $\widehat{\text{CRG}}$ model, are represented in Fig. 4.2.

The distance between two models is represented here in a convenient way by means of a bar graph. Results are therefore quantified by the height of the column and thus make them more visual than in a simple table. The model that is compared to the $\widehat{\text{CRG}}$ model is specified on the abscissa.

Several observations can be drawn from the simple bar graph from Fig. 4.2. First, we note that the compressibility factor ζ is the one that modifies the most the stability of the jet when computed by means of the less accurate model. Only changing this parameter leads to almost the same result as the non accurate $\widehat{\text{CPG}}$ model. The models for $\hat{\mu}$ and $\hat{h}$ show that these two parameters have a very small influence on the stability of the vortical mode at $\omega = 0.7$. Finally, $\hat{\rho}$ and $\hat{\lambda}$ has no influence on the instability. As the value for

---

[1] Or, in a equivalent way, the introduction of the $\widehat{\text{CRG}}$ model has a stabilizing effect on the mode compared to the $\widehat{\text{CPG}}$ model

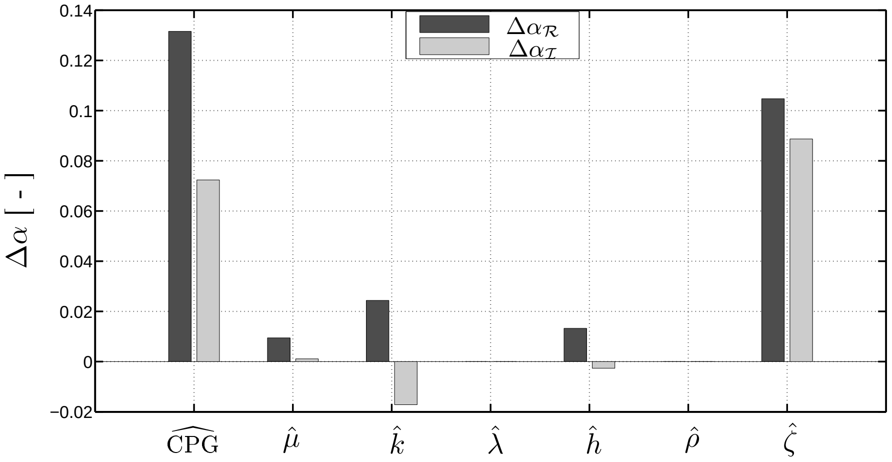

Figure 4.2: Influence of the model of transport and thermodynamic properties on the growth rate of the vortical mode compared to the accurate CRG model at $\omega = 0.7$ for the nominal case.

ρ was well predicted either considering a calorically perfect gas or a chemically reacting mixture of perfect gas, this results was expected (see Sec. 2.3.5).

As the thermal conductivity k and compressibility factor ζ are responsible of the two major contributions to the instability, let us investigate more closely their influence. The contribution of $\hat{\zeta}$ to the stability is made through the parameter ζ itself (i.e. without changing its derivatives) and its first and second derivatives (higher derivatives are not taken into account as they do not appear in the linearized stability equations). Let us denote by $\hat{\zeta}_T$ and $\hat{\zeta}_P$ the two models when only the derivatives of ζ are changed separately, without modifying any other parameters. We saw that the contribution of the derivatives of ζ also influenced the two parameters F and G, and must therefore be changed accordingly. The result obtain is shown in Fig. 4.3a.

The main contribution of ζ to the instability comes mainly from its first derivatives with temperature ζ_T, while ζ_P does not seem to have any influence of the stability of the mode.

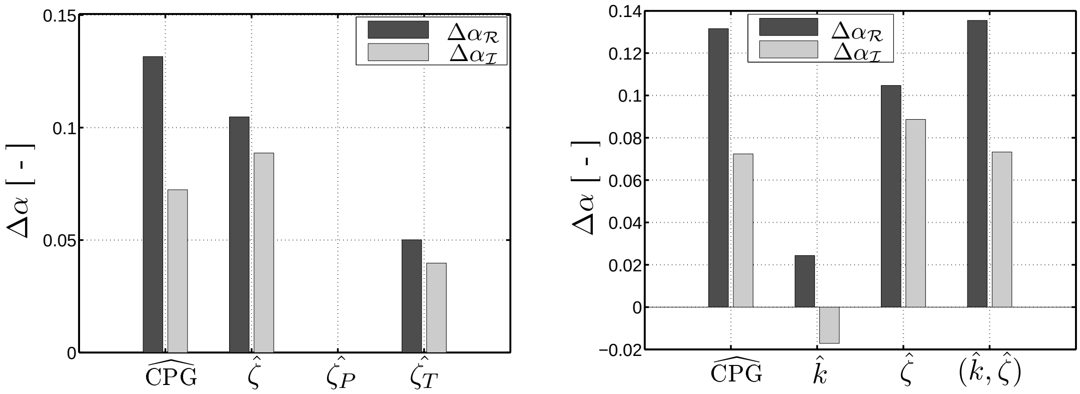

(a) Contribution of ζ and its derivatives

(b) Join contribution of $\hat{k}$ and $\hat{\zeta}$

Figure 4.3: Relative influence of model for the compressibility factor and thermal conductivity on the growth rate of the vortical mode related to the accurate CRG model at $\omega = 0.7$ for the nominal case.

This emphasizes once again the weak sensitivity of the flow properties to pressure.

From the previous results, it seems obvious that the gas state law plays a critical role in the stability of the jet. In particular, molar composition of the gas has to be known with good accuracy.

Finally, when modifying the law for both k and ζ, we see that they both contribute to the instability of the jet (Fig. 4.3b). The model with inaccurate law for both k and ζ is denoted by $(\hat{k}, \hat{\zeta})$. It can be observed that by modifying only the two parameters k and ζ, the value obtained with the CPG model can be almost retrieved. It suggests also that for this particular case, an additive property of the contribution of the different models to the instability of the mode can be observed.

In order to limit the dimensionality of the sensitivity analysis, we will restrict ourselves to the influence of frequency ω on the instability (next paragraph) and to the influence of the electric power P_{fl} (next section).

4.1.3 Dependence on frequency

The previous analysis was made for an adimensional frequency $\omega = 0.7$. We now extend it to the frequency range $\omega \in [0, 4]$. This range of values is chosen because for $\omega > 4$, the vortical mode tends to be stable. The local solver of VESTA is used and the starting solution for each model is the value obtained at $\omega = 0.7$. Starting from this solution, all the adimensional frequencies are swept by the local solver. For each model, the same curve as the one presented in Fig. 3.7a is computed and the distances between the adimensional wavenumber $\alpha^{\hat{\varphi}}(\omega)$ for two different models, defined in Eqs. 4.1 and 4.2, are calculated at each frequency.

The representation of the solution in bar graphs is not feasible anymore and one figure for each model for the quantity $\Delta\alpha_{\mathcal{I}}^{\hat{\varphi}}(\omega)$ as a function of ω is represented. Results for the one-parameter models for $\hat{\varphi} \in \{\widehat{\mathrm{CPG}}\} \cup \hat{\chi}$ are represented in Fig. 4.4.

For the $\widehat{\mathrm{CPG}}$ model in Fig. 4.4a, it can be observed that the function admits one zero. This means that at this frequency, the $\widehat{\mathrm{CPG}}$ and the $\widehat{\mathrm{CRG}}$ models give exactly the same result. It can be thought of as if there were a resonant frequency for which an accurate description of the flow properties is not necessary for the description of the instability of the mode.

While it was observed that k and ζ were the dominant parameters in the previous analysis for $\omega = 0.7$, it can be seen from the current analysis that this is not necessary the case everywhere. In fact, ζ is the dominant parameter at low frequencies. When instabilities for higher frequencies are considered, the influence of ζ decreases and μ (that was barely present previously) becomes the main driving parameter in the instability. $\Delta\alpha_{\mathcal{I}}(\omega)$ for both $\hat{\mu}$ and the $\widehat{\mathrm{CPG}}$ are indeed very close to each other in the range $[2, 3]$. At frequencies higher than 2.5, ζ is not influencing anymore the instabilities and all the behaviour is driven by the viscosity, except for some modulation by k and h at frequencies greater than three.

The model $\hat{\rho}$ and $\hat{\lambda}$ are represented on Fig. 4.4d as they both gives zero. For $\hat{\lambda}$ however, a small variation between $\omega = 3$ and $\omega = 4$ can be observed (of order 10^{-3}). This minimum is common for each model, except from $\hat{\zeta}$.

Again, it is possible to investigate from which derivative of the parameter ζ the instability is mainly initiated. Only ζ is investigated as it is the dominant parameter at low frequencies. The result is plotted in Fig. 4.5. As for $\hat{\zeta}_P$, $\Delta\alpha_{\mathcal{I}}$ is zero for all frequencies, we can deduce that the influence of the first derivative with respect to pressure of ζ and thus the parameter F can be neglected. For $\hat{\zeta}_P$, $\Delta\alpha_{\mathcal{I}}$ has the same shape as $\hat{\zeta}$ and therefore the influence on the stability due to ζ comes mainly from its first derivative w.r.t. temperature plus a contribution due to ζ itself and this relation seems linear with temperature. What is more important with ζ is that *it does not influence the stability anymore at high frequency.* At frequencies greater than two, the influence of ζ tends to zero, as well as its derivatives. This is a very interesting result as it means that for these frequencies the composition of

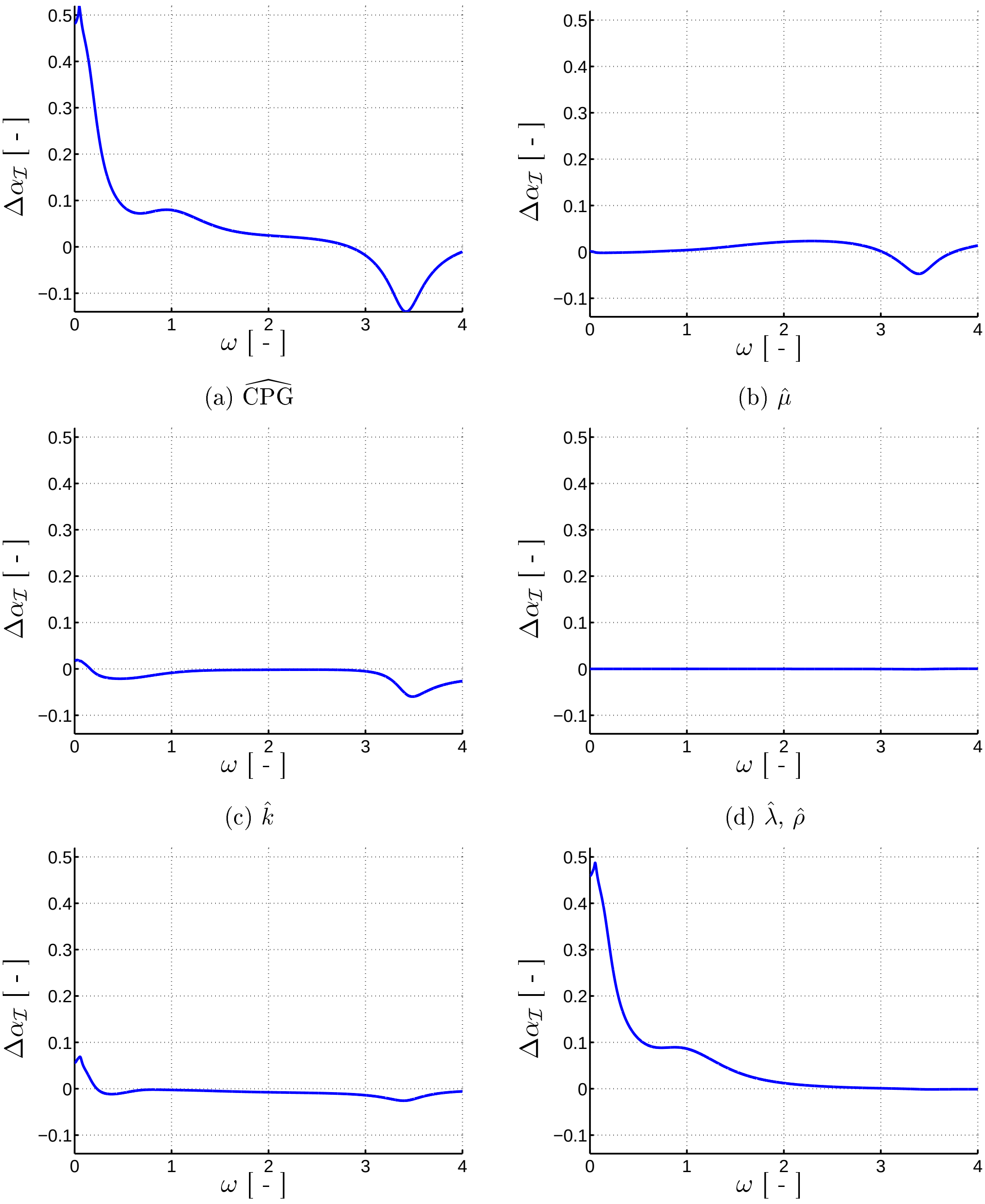

(a) $\widehat{\mathrm{CPG}}$ (b) $\hat{\mu}$

(c) $\hat{k}$ (d) $\hat{\lambda}$, $\hat{\rho}$

(e) $\hat{h}$ (f) $\hat{\zeta}$

Figure 4.4: Distance between the growth rate of the vertical mode of the $\widehat{\mathrm{CRG}}$ model and the different models involving simplified laws in temperature for the thermodynamic and transport as a function of the adimensional angular frequency ω.

the mixture is not determinant in the instability of the mode.

Finally, an interesting property, already observed in the analysis at fixed frequency, can be observed when summing the contributions to $\Delta\alpha_{\mathcal{I}}$ stemming from the models $\hat{\mu}$, $\hat{k}$, $\hat{h}$, $\hat{\lambda}$, $\hat{\zeta}$. Let us denote by

$$S_{\hat{\varphi}}(\omega) = \sum_{\hat{\varsigma}\in\hat{\chi}} \Delta\alpha_{\mathcal{I}}^{\hat{\varsigma}}(\omega) \tag{4.4}$$

the sum of the variation on the growth rate induced by each one-parameter model from $\hat{\varphi}$. The result obtained is represented in Fig. 4.6. The $\widehat{\mathrm{CPG}}$ model is recovered almost

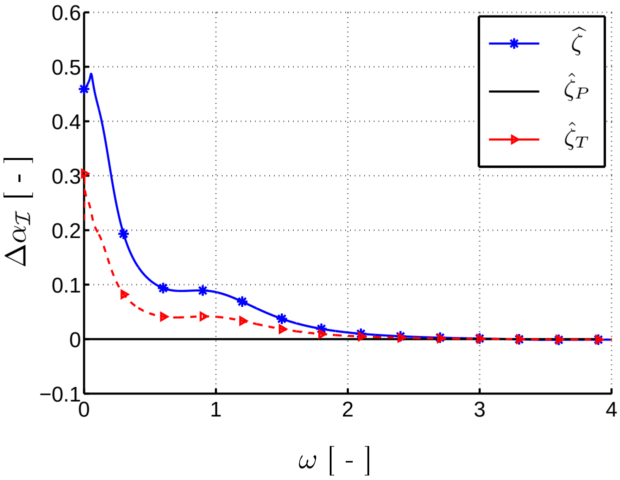

Figure 4.5: Comparison of the influence on the instability of the mode by the model considering a variation in the factor of compressibility ζ and its derivatives.

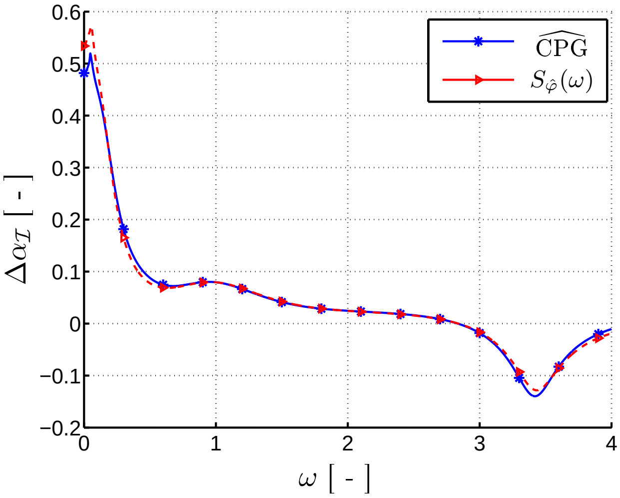

Figure 4.6: Comparison of the sum of all the variation on the growth rate of the mode induced by the different models with the reference model for a calorically perfect gas.

everywhere when summing all the variations on the growth rate induced by each model. A property of additivity in the contribution of each model to the instability of the mode is recovered in this case.

4.1.4 Influence of the model on the most amplified frequency

The last quantity of interest investigated in this sensitivity analysis for the nominal case is the frequency at which the growth factor attains its maximum. The distance between this most amplified frequency obtained for the reference $\widehat{\text{CRG}}$ model with an the one obtained for an arbitrary model is computed using the definition introduced in Eq. 4.3. The result for the most (dimensionless) frequency is given in Fig. 4.7a. The bar graph for the variation of the most amplified dimensional frequency from Fig. 4.7b is exactly the same (ignoring one multiplication factor) as all the characteristic quantities for the rescaling are the same for each model (centerline velocity, temperature and jet radius do not change).

In this last case, μ has a stronger influence than k. This stronger influence of viscosity is in agreement with the previous results from figure 4.4, where the influence of μ was greater near $\omega = 0.2$. Indeed, the most amplified frequency for the $\widehat{\text{CPG}}$ model was found

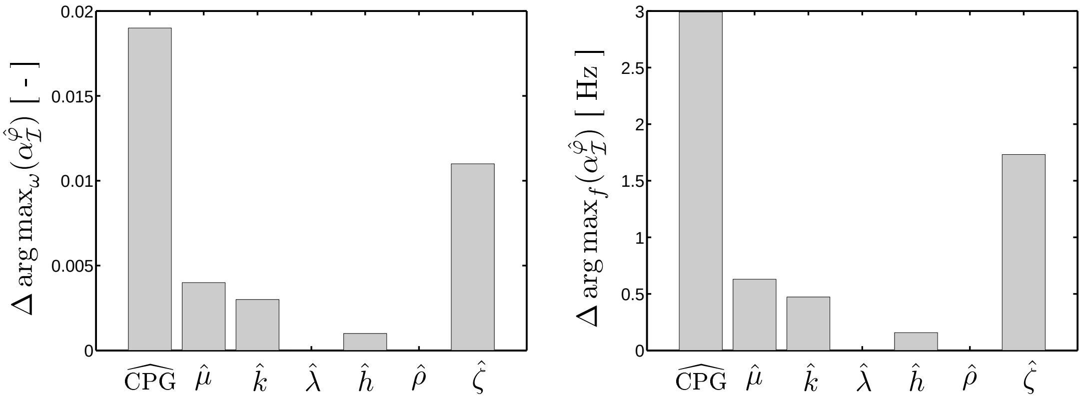

(a) Most amplified angular frequency

(b) Most amplified frequency

Figure 4.7: Influence of the model of transport and thermodynamic properties on the most amplified frequency compared to the accurate CRG model.

to be equal to 1.870 and does not change drastically from one model to an other, as can be seen in Fig. 4.7a. Therefore, the results for the most amplified frequency could be guess by looking at the results for each model close to $\omega = 1.87$.

4.1.5 Discussion on the results

Fixed frequency

It appears from this first analysis that the instability of the vortical mode of the jet at $\omega = 0.7$ is mainly due to the thermal conductivity k and the compressibility factor ζ. The sign of $\Delta\alpha$ indicates if the modification of the corresponding parameter is stabilizing or destabilizing comparing to the reference $\widehat{\text{CRG}}$ model.

The density of the gas has minimal influence on the stability but the composition of the flow has its influence through the compressibility factor ζ. A correct prediction of the mixture composition seems therefore important at low frequencies.

Influence with frequency and most amplified frequency

For frequencies higher than $\omega = 2.5$, the importance of the parameters is quite different. The compressibility factor has no influence on the instability of the mode at high frequency. This means that, regarding the linear stability, the composition of the gas has no more influence on its stability. Nevertheless, for frequencies in the range $\omega \in [2.5, 3]$ the main influence comes from the dynamic viscosity.

Finally, the same interpretation can be drawn considering the most amplified frequency of the vortical mode. The most amplified frequency is important in the analysis as it is the one that will be actually observed in the Plasmatron if the vortical mode is the dominant one. In this case, the value of ω is between 1.5 and 2. In this range of value, the influence of ζ on the mode has already decreased (compared to the previous case at $\omega = 0.7$) and the influence of μ is stronger than the thermal conductivity.

A more physical explanation for the influence of μ can be described when considering the microscopic behaviour of the flow. **Consider first the influence of μ with frequency**. The viscosity is associated to a transport of momentum of the particles and thus is linked to inertia. At low frequencies, the phase speed of the instability wave is very high compared to the speed of the flow (Fig. 3.7b) and the associated wavelength is high compared to the characteristic axial length. The instabilities does not have the time to influence the mean flow. On the contrary, for moderate frequencies, wavelength is comparable to the axial characteristic length of the jet. Then, a pressure imbalance as observed in the eigenfunctions of the vortical mode can cause the particles to move. **We consider now the destabilizing effect of the viscosity at moderate frequencies** ($\Delta\alpha_{\mathcal{I}} > 0 \Rightarrow \alpha_{\mathcal{I}}^{\widehat{\text{CPG}}} > \alpha_{\mathcal{I}}^{\hat{\mu}}$). The model $\hat{\mu}$ considers a lower value of viscosity than the $\widehat{\text{CPG}}$ model. Recall that vortical mode is due to a pressure imbalance initiated in the shear layer. A higher viscosity tend to keep the particles to each other and slow the mechanism of formation of vortical mode. At lower value of the viscosity, the flow will have a much faster response to a shear stress. From this consideration, it seems obvious that the viscosity has an influence of the instability of the vortical mode. This assumes therefore that the mechanism of formation of the instability considered plays a significant role. For the vortical mode, viscosity is the dominant driving parameter. It would therefore probably not willing to be the case if acoustics mode as they are modes that, as their name suppose, much more dependent on the equilibrium speed of sound. This thermodynamic property is strongly coupled to the enthalpy of the flow and one can expect that this will influence the stability of acoustic modes.

In order to verify this hypothesis, it has been possible to investigate the spectrum of the different flow models by identifying the acoustic modes by hand. The results for the second, third and fourth acoustic modes are given in Fig. 4.8 (for the values of the reference $\alpha^{\widehat{\text{CRG}}}$ and notation of the acoustic modes, see Fig. 3.6). The vortical mode is also represented for comparison. As expected, it can be observed that enthalpy is now playing a significant role in the instability of the mode, while is was barely noticeable for vortical mode. A general decrease in $\Delta\alpha_{\mathcal{I}}$ can be observed as the radial mode number is increasing. An increasing in the radial mode number was shown to have more anti-nodes in its pressure distribution. These modes could be seen as waves carrying less energy. The relative influence of ζ is strong for each mode.Note that while a kind of additivity was observed for the vortical mode, it is not the case here for the vortical mode. Models using more than one parameter modified, as in Fig. 4.3b could be investigated to see the effect of join contribution.

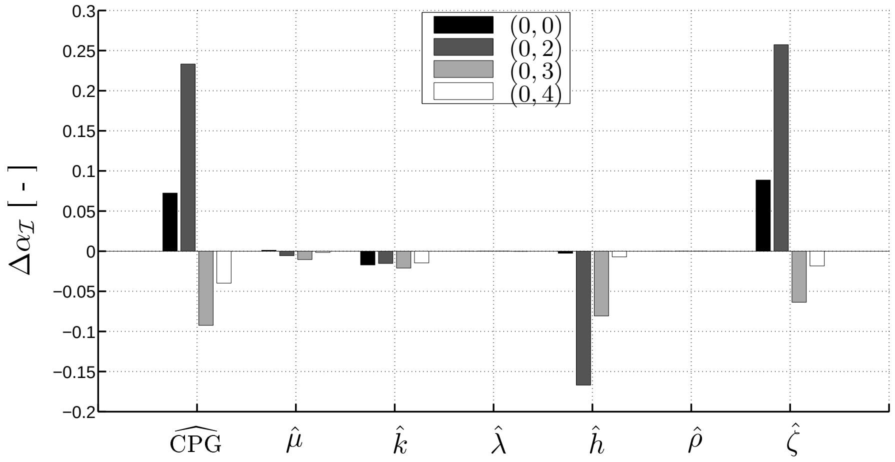

Figure 4.8: Influence of the model of transport and thermodynamic properties on the growth rate of the three first acoustic modes compared to their accurate CRG model at $\omega = 0.7$ for the nominal case.

The results of this sensitivity analysis may suggest therefore a methodology that could be used to identify the mechanism that are responsible of the instability of a particular type of mode. In the case of the vortical mode, we found that the viscosity was one of the main driving parameter of the instability. At low frequencies, talking about the vortical may not necessarily have sense as in this case, phase speed is incredibly high as so is the relative Mach number to the centerline velocity, and the vortical mode is not a vortical mode anymore by definition. Acoustic modes were related to the enthalpy of the flow, but also to the viscosity.

These results should however be interpreted carefully as the analysis for the acoustic modes is made only at a fixed frequency. For the vortical mode, a strong variation in the growth rate of the instability was observed when the frequency was varied and it was possible to emphasize the importance of the viscosity. Nothing can be said about the influence of the frequency on the acoustic modes obtained here. What we can emphasize however here is that enthalpy plays a significant role, at least for $\omega = 0.7$ for the acoustic modes, that was not present in the vortical mode. Ideally, a sweep of all frequencies should be made for each acoustic mode for a correct interpretation of the results. This however can become computationally expensive.

This analysis has been made for a single electric power of the plasma flow P_{fl} and a single mass flow rate $\dot{m}$. We have also presented the case for only one pressure in the Plasmatron. For the stability analysis, we also had to select one particular position in the jet and we had to restrict ourselves to a particular set of unstable modes. We should keep also in mind that the influence of flow parameters can also modify the value of the adimensional numbers. For example, the viscosity modifies the value of the Reynolds number. Ideally, the influence of the Reynolds and the viscosity should be investigated separately in order to see which one is the most responsible of the instability, as we did for example for the derivatives of ζ.

This emphasizes the issue of the multi-parametric dimension of the stability analysis of the jet. Moreover, some inputs can be considered as uncertain. The uncertainty of the electric power transmitted to the plasma is the topic of the next section.

4.2 Uncertainty Quantification of the Electric Power

The previous analyses were made for the nominal (deterministic) case with different model parameters and it resulted in one prediction for the output quantities of interest for each model. However, as already mentioned, the efficiency of the Plasmatron is not well defined and so far could not be measured inside the facility. In all the previous studies on the plasma jet, a single efficiency of the electric power equal to 50% was used.

In this second section, the effect of an uncertain electric power efficiency on the quantities of interest is investigated. The value of the electric power plays a significant role on the shape of the velocity profile and on the temperature of the jet and it can therefore modify significantly the stability of the jet. Characterizing the effect of the uncertainty on the electric power becomes therefore an important step for correctly interpreting the stability of the jet.

Many methods exist for the quantification of uncertainty and a short overview of a number of methods can be found in [3]. Although applied to computational mechanics, these methods can be applied in this case as well. In this work, a *probabilistic framework* is adopted and *non-intrusive* methods for quantifying uncertainty are used. Working with probability will allow us to characterize uncertain inputs and outputs with probability distribution functions, allowing an intuitive interpretation of the results. The input uncertainty can be either propagated by deriving a new model and implementation for the uncertainty problem, which can be solved at once. This is called intrusive UQ, because existing deterministic codes need to be modified. On the other hand, non-intrusive UQ methods can re-use an existing deterministic solver as a black-box. Non-intrusive methods will afford us to use the already existing developed codes (VESTA, COOLFLUID, MUTATION) without any modification of their core and this will allow us to develop routine around them and perform embarrassingly parallel simulations with little effort for speedup.

4.2.1 Methodology: characterization of the input uncertainty

The first step in the uncertainty quantification is the characterization of the input uncertainty. In this work, parametric approach is sought, that is the uncertain features of the computational model can be associated with some or all of its parameters. In this case, the electric power transmitted to the plasma P_{fl} is the only uncertain parameter. In the probabilistic framework this uncertain input is modelled as a random variable $\mathcal{X}$ with probability distribution $P_{\mathcal{X}}$. The random variable is a continuous variable with values in $\mathbb{R}$, but of course not all values will be encountered as it depends on the characteristics of the Plasmatron and its performance. The probability distribution $P_{\mathcal{X}}$ then attributes to any meaningful subset $B \in \mathbb{R}$ the probability $P_{\mathcal{X}}(B)$ of finding the random variable $\mathcal{X}$ in the subset B. In the case of continuous random variables, we can define a *probability density function* $\rho_{\mathcal{X}}(x)$ which is defined as

$$\begin{aligned} P_{\mathcal{X}}(B) &= \int_B \rho_{\mathcal{X}}(x) dx \qquad (4.5) \\ &= \int_B dP_{\mathcal{X}}(dx). \qquad (4.6) \end{aligned}$$

The following paragraphs are devoted to the characterization of the probability density function for the random variable $\mathcal{P}_{fl}$ and the definition of its subsets of admissible values.

In section 2.1, we already mentioned briefly that the electric power that is actually transmitted to the plasma flow, P_{fl} is not well-defined and can not be directly measured inside the Plasmatron facility. P_{fl} is supposed to be only a fraction of the initial electric power supply P_{el} and both can be related through an efficiency parameter η

$$P_{fl} = \eta P_{el}. \qquad (4.7)$$

We will now try to characterize the parameter η and gives bounds around its nominal value.

The efficiency, or the performance of the Plasmatron, depends on the coupling between the generator and the plasma. Without going into details, which are out of the scope of this work, the coupling may change from one set of operating conditions $(P_{el}, \dot{m}, p_{tc})$ of the Plasmatron to the other and thus change the overall efficiency. This efficiency has been estimated to be of the order of 50% [5]. More recent experimental results of the measurement of the efficiency using a global energetic balance of the Plasmatron facility showed a variability of the efficiency near ±5% [9]. Therefore, as a first insight in the uncertainty of the electric power, one could use an efficiency of $50\% \pm 5\%$ and assign it an equiprobable density function.

Finally, as P_{fl} is the power that has to be provided for the CFD simulations, one has to specify the range of values that will be used in this work. The choice of the range of P_{fl} is arbitrary and we choose here the range $P_{fl} = [75, 95]$ [kW] with mean value equal to 85 [kW]. This could be related to a $P_{el} = 170$ [kW] imposed to the Plasmatron with a given efficiency of $50\% \pm 5.88\%$. The probability density function of the random variable $\mathcal{P}_{fl}$ is represented in Fig. 4.9.

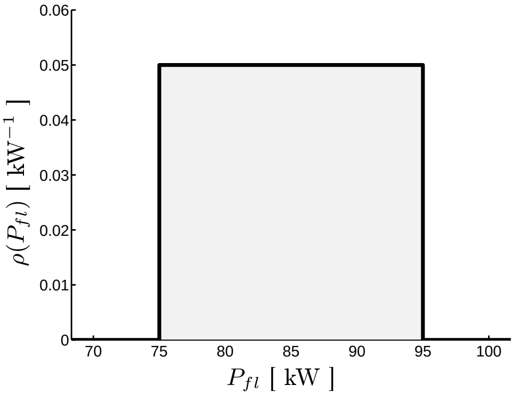

Figure 4.9: Input pdf

This choice of range of values has been motivated by the already available CFD simulation at the VKI. In this case, the three CFD simulations at 75, 85 and 95 [kW] were already available for $p_{tc} = 17143$ [Pa]. The UQ methodology developed through the next sections will be first tested only using these three simulations. Velocity and temperature profiles at intermediate powers will be obtained using linear interpolation between the existing simulations. This will be used to study the convergence of the stochastic model used. Then new CFD simulations will be computed to obtain more accurate results. The number of CFD simulations that will have to be computed will be based on the convergence analysis of the non-accurate results.

Before going to the UQ methodology, we should mention briefly the range of applicability of the study on P_{fl} as the input uncertainty. Imagine now that the efficiency is fixed and is considered to be deterministic. If P_{el} is now the uncertain input, it comes from Eq. 4.7 that the same uncertainty quantification on P_{fl} is still applicable. This means that the analysis developed in this section could be extended as well to the study of the uncertainty of the electric power injected to the facility. For example, the experimenter assigns an electric power of 170 [kW] to the facility with an uncertainty on its value of 5 [kW] and efficiency fixed to 50% would give rise to an uncertainty on P_{fl} in the range $[82.5, 87.45]$ [kW].

4.2.2 Methodology: propagation of uncertainties

The second step for uncertainty quantification is the *propagation of the uncertainty* through the computational model. Knowing the pdf of the input we would like to know what is the pdf of the quantity of interest (output). Once the output pdf is known, statistical descriptors can be computed for a direct characterization of the quantity of interest, such as the *mean*, the *variance* or the *coefficient of variation* (*cov*). These are defined as follows:

$$m_Y = \int_{\mathbb{R}} y \, dP_Y \ , \tag{4.8}$$

$$\sigma_Y^2 = \int_{R} (y - m_Y)^2 \, dP_Y \ , \tag{4.9}$$

$$cov = \frac{\sigma_Y}{m_Y} \ , \tag{4.10}$$

assuming these integrals are bounded. The last statistical quantity defined by Eq. 4.10 is an indicator of the relative range of uncertainty on a given quantity. A large coefficient of variation implies a large uncertainty on the quantity of interest. This one can be compared to the coefficient of variation of the input to see if the model actually amplifies the uncertainty or on the contrary decreases the uncertainty.

Several methods exist for uncertainty propagation and the most popular is the *Monte Carlo* method. Monte Carlo approach involves repeated simulations (also called realizations) with random sampling from the space of the random variable $\mathcal{X}$ according to the given input pdf. Output pdf can then be estimated using a kernel density estimation procedure. Statistical descriptors from Eqs. 4.8 and 4.9 can be estimated by summing all the results of the simulation and dividing by the number of samples

$$m_Y \approx m_Y^{\nu} = \frac{1}{\nu} \sum_{l=1}^{\nu} y^{(l)} \ , \tag{4.11}$$

$$\sigma_Y^2 \approx \sigma_Y^{2,(\nu)} = \frac{1}{\nu} \sum_{l=1}^{\nu} (y^{(l)} - m_Y^{\nu})^2 \ , \tag{4.12}$$

where ν represents the number of samples used in the Monte Carlo method. According to the Law of Large Number (LLN) the mean will converge to the exact value as the number of samples ν increases. By the Central Limit Theorem (CLT), the accuracy improves with the square root of ν.

However, this method can becomes prohibitive when applied directly to the computational model as many simulations are needed for convergence and the computation cost can becomes very high. Instead, an other class of method will be investigated and applied in this work. These are called *stochastic collocation methods*.

4.2.3 Implementation: stochastic collocation methods

We think of the computational model as a surjective mapping s of any value of the input into the quantity of interest, considered as random variables

$$\mathcal{Y} = s(\mathcal{X}) \ , \tag{4.13}$$

where $\mathcal{X}$ and $\mathcal{Y}$ are respectively the input and output random variables. This mapping is often a complex model to solve, involving many PDEs as it in the case for the VESTA code and a natural idea is to construct a much simpler mapping, or a *surrogate* model, that approximates the actual complex model.

Once a surrogate model s is known, it can serve as a substitute for the computational model for approximating the statistical descriptors of the quantity of interest. From the definition of the mean and variance Eqs. 4.8 and 4.9, these statistical descriptors can be approximated, considering $y = s(x)$, as

$$m_Y = \int_{\mathbb{R}} y \, dP_Y = \int_{\mathbb{R}} s(x) \, dP_X = \int_{\mathbb{R}} s(x)\rho_X(x)dx, \tag{4.14}$$

$$\sigma_Y^2 = \int_{\mathbb{R}} (y - m_Y)^2 \, dP_Y = \int_{\mathbb{R}} (s(x) - m_Y)^2 \rho_X(x)dx. \tag{4.15}$$

These two integrals can be approximated using quadrature rules, following the method applied in [17].

On the other hand, statistical descriptors and output pdf can be again estimated using Monte-Carlo sampling. The advantage now is that the Monte Carlo sampling is directly propagated through the surrogate model and the gain in computational cost is significant.

Many non-intrusive methods exist for building a surrogate model. *Spectral projection methods* and *interpolatory collocation methods* are often encountered. In the case of non-intrusive spectral projection methods (NISP), the model is sought as a projection on an orthonormal basis of the initial model and for which expansion coefficients are computed numerically. Interpolatory collocation methods, or stochastic collocation (SC) rely on the interpolation between a finite number of points where the solution has been computed. In the case of SC methods, the approximation will be exact at these collocation points. This second methodology of stochastic collocation will be used in this work and basic knowledge are presented through the next paragraphs.

Polynomial interpolation

The surrogate model is build by interpolating $n + 1$ solutions of the computational model at $n + 1$ pre-defined points. The surrogate model is assume to have the expression

$$s_n(x) = \sum_{i=0}^{n} s(x_i) l_i(x), \tag{4.16}$$

where $\{l_i\}_{i=0}^n$ are the Lagrange polynomials associated with the collocation points and $s(x_i)$ are the values taken by the computational model at these collocation points. The Lagrange polynomials are defined by the product

$$l_i(x) = \prod_{\substack{j=0, \\ j\neq i}}^{n+1} \frac{x - x_j}{x_i - x_j}, \quad \text{for } i = 0, \ldots, n. \tag{4.17}$$

More on polynomials interpolations can be found in [36].

Convergence of the surrogate model

A desirable property is that the precision with which the surrogate model approximates the computational model can be improved by increasing the number of collocation points in the interpolation, that is

$$\lim_{n\to\infty} \int_{\mathbb{R}} |s(x) - s_n(x)|^2 \, dP_{\mathcal{X}} = 0. \tag{4.18}$$

Provided that suitable collocation points are used, the property in (4.18) holds under mild conditions on the computational model s and on the probability distribution $P_{\mathcal{X}}$. The convergence can be expected to be fast if the computational model is sufficiently smooth.

Gauss quadratures

Statistical descriptors in Eqs. 4.14 and 4.15 are defined by integrals. As $s(x)$ is a polynomial, it could be integrated analytically. However, for Lagrange polynomials of high degree, computation can be quite fastidious. Numerical integration by means of appropriate quadrature rule is therefore sought [15].

A quadrature rule consists of replacing the integral by a weighted sum of the function evaluated at n given nodes $t_j^{(n)}$

$$\int f(x)\rho(x)dx \approx \sum_{j=1}^{n} f(t_j^{(n)})w_j^{(n)}, \tag{4.19}$$

where w_j are the weights of the quadrature rule. Zeros of orthogonal polynomials are excellent candidates for numerical integration. Orthogonal polynomials with respect to some probability density function on a given interval I are defined as

$$\int_I Q_m(x)Q_n(x)\rho(x)dx = \gamma_n\delta_{mn}, \tag{4.20}$$

where δ_{mn} is the Kronecker delta operator, γ_n a normalization constant and m, n the order of the polynomials $Q(x)$. Some useful properties of orthogonal polynomials and their zeros are stated below. Their demonstration and more discussion on them can be found in [36].

Property 4.1 Let $\{Q_n(x)\}$, $n \in \mathbb{N}$, $x \in I$, be orthogonal polynomials satisfying orthogonality relation (4.20). Then, for any $n \geq 1$, Q_n has exactly n real distinct zeros in I.

Property 4.2 Formula (4.19) is exact; i.e., it becomes an equality, if $f(x)$ is any polynomial of degree less than or equal to $2n - 1$.

It the case of a uniform density $\rho(x)$, polynomials $Q_n(x)$ are the Legendre polynomials and the corresponding quadrature rule is the Gauss-Legendre quadrature. For the standard Gaussian density, the polynomials are the Hermite polynomials and the quadrature rule is the Gauss-Hermite quadrature. From Property 4.2 we see that the mean (see Eq. 4.14) can be estimated correctly if the the computational model is a polynomial of degree lower than $2n - 1$. The order of the computational model is however not know *à priori*. In this work, as the probability density function is uniform, Gauss-Legendre quadrature are used for the numerical integration with respect to the pdf. The nodes and the weights can be found in pre-computed tables ([15]). Already built in functions can also be found[2].

Interpolation nodes

Until now, no assumption has been made on the interpolation points x_i used in Eq. 4.16 and they still need to be defined. The use of equidistant points is easy to implement but it may not be suitable for convergence property. As it is known, polynomial interpolation at uniformly distributed points can leads to oscillations near endpoints at high degrees (Runge phenomenon). On the contrary, zeros of orthogonal polynomials are excellent candidates for both interpolation and numerical integration (Property 4.1). Gauss-Legendre points offer better convergence properties than equispaced points and will generally be preferred. An other very popular choice are the Chebyshev collocation points. These nodes are defined as the maximum of the Chebychev polynomials, including the two boundary nodes. In this work, both Gauss-Legendre and Chebyshev points are presented as they have different properties that might be interesting.

---

[2] `http://people.sc.fsu.edu/~jburkardt/`

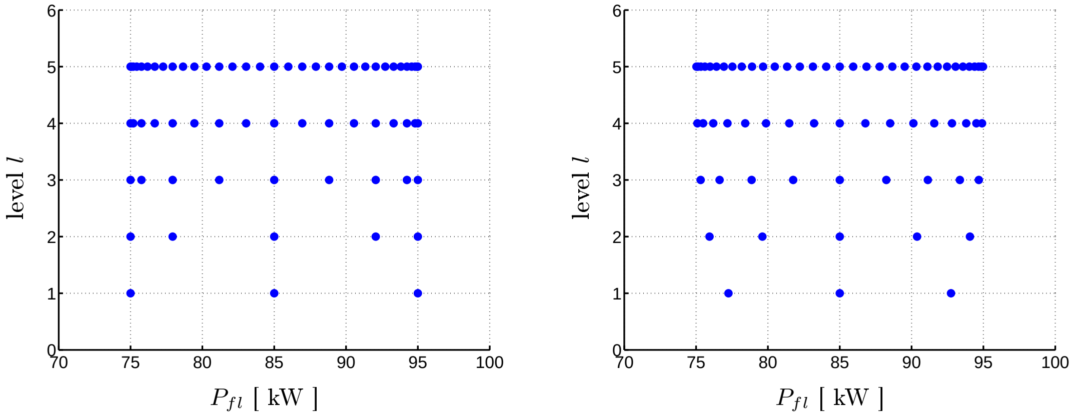

(a) Clenshaw-Curtis abscissa

(b) Gauss-Legendre abscissa

Figure 4.10: Comparison between Clenshaw-Curtis and Gauss-Legendre abscissa.

Gauss-Legendre interesting features have been discussed previously. They have the advantage of integrating polynomials of degree lower than $2n - 1$ with respect a uniform measure. They however have the drawback of not being nested, that is, of having a node distribution that depends on n.

For this purpose, Clenshaw-Curtis nodes are more appropriate. Although they do not verify the interesting property 4.2 of Gauss-Legendre quadrature rule, they have the advantage of being nested [20]. The number of nodes at a given level l are given by

$$n_l = 2^l + 1. \tag{4.21}$$

This property is illustrated in Fig. 4.10 where both Clenshaw-Curtis nodes (Fig. 4.10a) and Gauss-Legendre nodes (Fig. 4.10b) are compared. There are presented here on the domain of values $[75, 95]$, on which the input quantity P_{fl} is defined. For the Clenshaw-Curtis abscissa, each level $l > 1$ is defined by the nodes that were present on the previous level plus a new set of nodes. Therefore, if computations are present at a given level, they can be reused for the next level. On the contrary, Gauss-Legendre nodes and the results associated have to be recomputed for each level.

4.2.4 Numerical results: use of approximate profiles

In this section, the numerical model with all the correct transport and thermodynamics properties is used (i.e., the $\widehat{\text{CPG}}$ model). The parameters of the nominal case are again used except that we now vary the electric power. For each value of P_{fl}, a new mean velocity and temperature profile is computed (as in Fig. 3.4). As these two profiles are now allowed to vary, a greater change in the instability of the vortical mode is expected.

The surrogate model is computed succinctly using an increasing number of collocation points. Both models with Gauss-Legendre and Clenshaw-Curtis abscissa are compared. Fig. 4.11 shows the results for the growth rate of the first vortical mode.

We can see that the interpolations using the two types of abscissa lead to similar results. When using a low number of points, we see that $-\alpha_{\mathcal{I}}$ is close to a linear relation of P_{el}. When the number of points is higher, small oscillations are caught by the interpolation. The growth rate has therefore a global linear behaviour with a superposition of modes of small perturbations. If the relation was strictly linear, the output PDF would be the same as the input PDF. In this case, the output PDF can be expected to have oscillations around a constant values. This can be also interpreted as the fact that when using a small number of points, the surrogate model has not yet converged, as it will be confirmed in the next section by the convergence analysis.

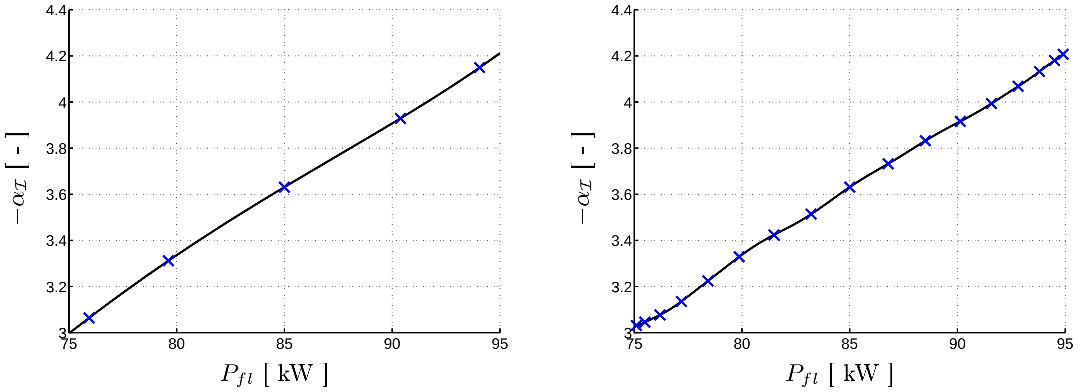

(a) Surrogate model with Gauss-Legendre collocation points (-×-)

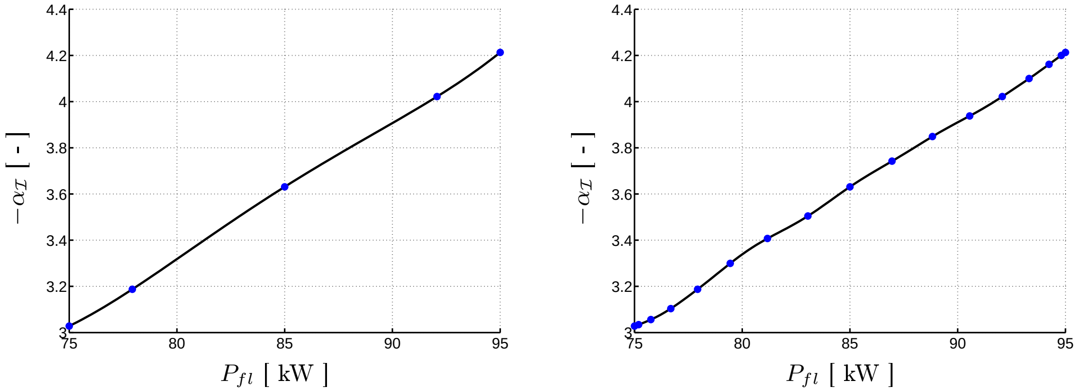

(b) Surrogate model with Clenshaw-Curtis collocation points (-●-)

Figure 4.11: Surrogate model for the growth rate α_i of the first vortical unstable mode at $\omega = 0.7$ using polynomial interpolation at: (a) Gauss-Lengendre collocation points and (b) Clenshaw-Curtis points, with 5 (left) and 17 (right) points.

Convergence analysis of the surrogate model

Before any uncertainty propagation, the convergence of the surrogate model has to be ensured. The exact solution of the model $s(x)$ is not know and Eq. 4.18 can not be applied directly. Instead, the following sequence will be computed numerically:

$$S_n^2 = \int_{\mathbb{R}} |s_n(x) - s_{n-1}(x)|^2 \, dP_{\mathcal{X}}. \tag{4.22}$$

We can show that S_n^2 tends to zero as n goes to infinity. Noting that Eqs. 4.18 and 4.22 is in fact the square of the norm defined on $\mathbb{L}_2$, $||\cdot||_2$, where $\mathbb{L}_2$ is the space of function for which the square is Lebesgue integrable, we have

$$\begin{aligned} S_n &= ||s_n(x) - s_{n-1}(x)||_2 \\ &= ||s_n(x) - s(x) + s(x) - s_{n-1}(x)||_2 \\ &\leq ||s_n(x) - s(x)||_2 + ||s(x) - s_{n-1}(x)||_2, \end{aligned} \tag{4.23}$$

where the inequality sign came from the triangular inequality. Taking the limit of n tending to infinity and using Eq. 4.18, it follows directly that

$$\lim_{n\to\infty} S_n = 0 \tag{4.24}$$

$$\Leftrightarrow \lim_{n\to\infty} S_n^2 = 0. \tag{4.25}$$

Although Eq. 4.22 is a good indicator for the convergence of the model, it does not say anything about the error made by the approximation $s_n(x)$ on the exact solution $s(x)$. Numerical results of the sequence S_n are shown in Fig. 4.12. For both Gauss-Legendre and Clenshaw-Curtis abscissa, the sequence seems to converge. The relative decrease between two approximations seems to stabilize for $n \geq 10$. Therefore, a suficiently high number of collocation points will have to be used for the uncertainty propagation.

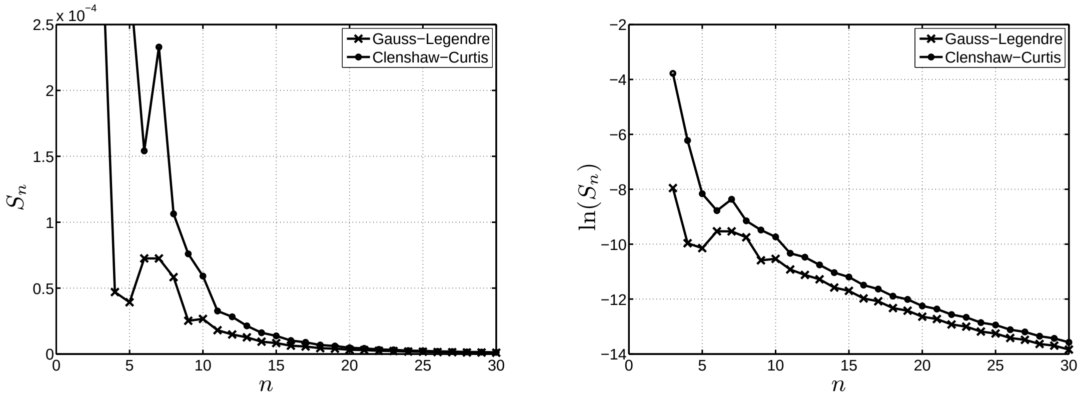

(a) Normal plot

(b) Semi-log plot

Figure 4.12: Convergence of the sequence S_n at $\omega = 0.7$ using Gauss-Legendre and Clenshaw-Curtis points on a linear scale (a) and on a semi-log ($\ln(S_n)$) scale (b)

From this convergence analysis, we can say that the two interpolation nodes lead to similar results at the same rate of convergence. Therefore, the Clenshaw-Curtis abscissa will be used for the interpolation in the next sections because of their nested property at each level l. As the surrogate models obtained with the two methods are quite close, the computation of the statistical descriptions by means of the Gauss-Legendre quadrature rule should give almost the same result.

Propagation of uncertainty at fixed frequency

Once the surrogate model is available, the propagation on the uncertain input through the model can be carried out. The most intuitive method for the propagation is the Monte-Carlo sampling. A set of i.i.d. samples is generated from the input density and the output is computed using the surrogate model. A distribution of samples is obtained on the domain of the output and the density can be estimated by using the kernel density estimation method. The result for the first quantity of interest, the growth rate $\alpha_{\mathcal{I}}$, is shown in Fig. 4.13.

Several observations can be made:

1) The surrogate model follows almost a linear relation. Therefore, the output pdf is close to an equiprobable distribution function but with some oscillations, due to the computational model.

2) Compared to the sensitivity analysis performed in Sec. 4.1 the variation of the growth rate of the vortial mode due to the variation of electric power is much more significant.

In the case of a strictly increasing function (or decreasing)[3], it is also possible to

---

[3] More generally, if the surrogate model is a bijective function.

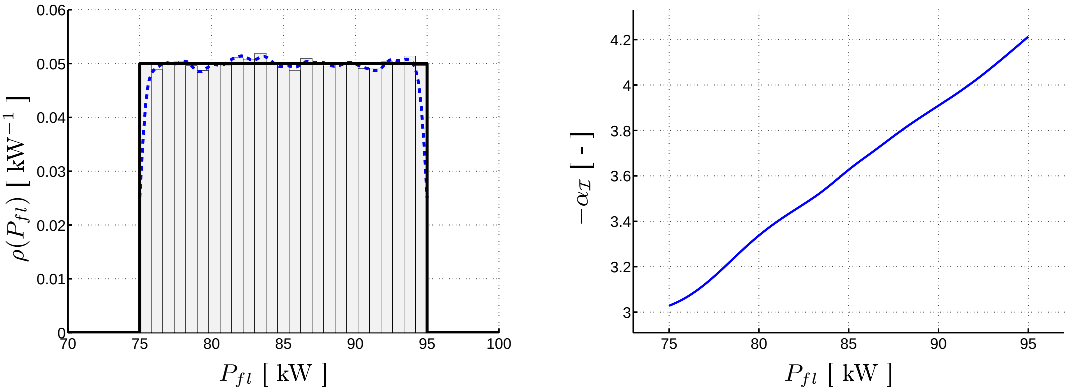

(a) Input pdf (b) Surrogate model

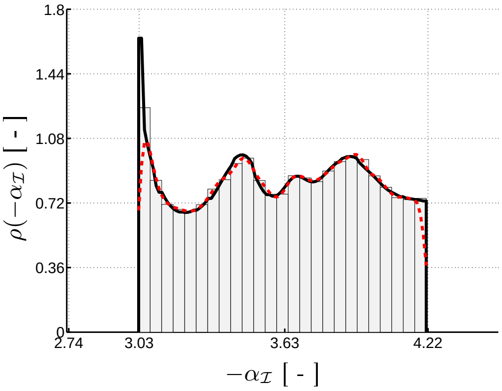

(c) Ouput pdf

Figure 4.13: Propagation of the input uncertainty (a) through the surrogate model of the first vortical mode (b) using 30 collocation points. (c): Output Ppdf. — : Analytical pdf's, – – : estimated pdf's. ω is fixed and equal to 0.7.

estimate the output pdf analytically.

$$\rho_{\mathcal{X}}(x)dx = \rho_{\mathcal{Y}}(y)dy, \tag{4.26}$$

$$\begin{aligned}
\rho_{\mathcal{Y}}(y) &= \rho_{\mathcal{X}}(x)\frac{dx}{dy} \\
&= \rho_{\mathcal{X}}(s^{-1}(y))\frac{d}{dy}s^{-1}(y) \\
&= \rho_{\mathcal{X}}(s^{-1}(y))\left(\frac{d}{dx}s(x)\right)^{-1} && (4.27) \\
&= \rho_{\mathcal{X}}(s^{-1}(y))\left(\frac{d}{dx}s(s^{-1}(y))\right)^{-1}, && (4.28)
\end{aligned}$$

where we used $x = s^{-1}(y)$, assuming that the inverse exists, which is verified for strictly increasing (decreasing) functions and where Eq. 4.27 was obtained using the inverse function theorem.

However, the inverse $s^{-1}(y)$ in Eq. 4.28 may not be easily expressed. For the interpolating lagrange polynomial, it becomes impossible to obtain it by direct analytical methods. Therefore, the output pdf is obtained pseudo-analytically.

The pseudo-analytical output pdf can be used to validate the convergence of the Monte-Carlo sampling for the estimation of the pdf. The two curves in Fig. 4.13c almost recovered exactly, except near the strong variation in the output pdf. Thus, the number of samples used in the Monte Carlo method (here, 10^5 samples were used) is sufficient to ensure the convergence of the solution.

We can also check the convergence of the Monte-Carlo method using the Law of Large Numbers for the estimate the mean m_Y using Eq. 4.11 as the number of samples increases. The following figure represents the estimation of the mean as a function of the number of samples ν. After 10^5 samples, the variations in the estimate of the mean becomes very small, indicating that the estimate has converged. The shaded area represents the 95% interval of confidence for the mean as the number of samples increase It is the range of value where the central limit theorem indicates with 95% confidence that the mean values will lie.

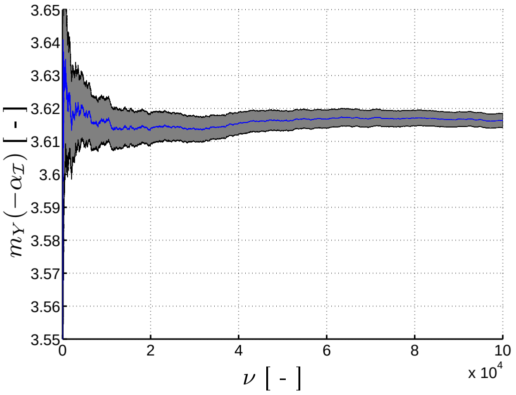

Figure 4.14: Convergence of the mean as the number of samples in the Monte-Carlo method increases.

It is therefore possible to compute the statistical descriptors using either the Monte-Carlo sampling and calculate Eqs. 4.11 and 4.12, or by direct numerical integration of the surrogate model with respect to the input pdf. The numerical values obtained are presented in Tab. 4.1. The result obtained for the mean by the Monte-Carlo estimation corresponds to the value obtained after $\nu = 10^5$ using the same sampling as in the previous figure. The two estimations are in good agreement. For the comparison, the input coefficient of variation $cov_X = 0.068$, which means that the uncertainty, after the propagation through the computational model, is greater on the output QoI than on the input electric power. The output mean m_Y of the QoI (which is here the growth rate of the vortical mode) is very close to the value that was obtained for the nominal case at $P_{fl} = 85$ [kW] (for which $-\alpha_{\mathcal{I}} = 3.5606$). The output standard deviation σ_Y indicates the distribution of the value of the QoI around the mean. This value has to be compared to the result of sensitivity analysis made in Sec. 4.1 for which a maximum value of $\Delta\alpha_{\mathcal{I}} = 0.09$ was obtained using the $\hat{\zeta}$ model, at $\omega = 0.7$ (see Fig. 4.2). Therefore, the variation on the growth rate due to the uncertainty on the input electric power has a greater influence compared to the variation when one or several flow properties of the model are not predicted accurately. This suggests that for a correct prediction of the growth rate of the first vortical mode, the uncertainty on the electric power must be reduced.

	Monte-Carlo	GL quadrature
m_Y	3.6175	3.6174
σ_Y	0.3418	0.3415
cov_Y	0.0945	0.0944

Table 4.1: Comparison of the statistical descriptors estimated by the Monte-Carlo method and by numerical integration using Gauss-Legendre quadrature rule.

The estimation of statistical descriptors by means of direct numerical integration will be preferred in the following sections. We emphasized here the two ways of computing them and showed that the results obtained using the two methods were closed.

Coefficient of variation as a function of frequency

The previous analysis was made for a single value of the frequency ω. However, the uncertainty on the growth rate due to the input electric power might not be the same for each value of ω. Therefore, the procedure applied previously for a single value of ω is now made for $\omega \in [0, 4]$. At this point, it is useful to think about VESTA as a function of the two variables P_{fl} and ω which returns a value in the $\alpha_{\mathcal{I}}$ space. Thinking this way, $\alpha_I(P_{fl}, \omega)$ can be represented by a 2D surface, as represented in Fig. 4.15a.

For each value of P_{fl} defined by the CC abscissa, the local solver of VESTA is used to sweep all the frequencies, starting from the solution at $\omega = 0.7$. Once the values of $\alpha_{\mathcal{I}}$ are obtained for each frequency and each electric power, the surrogate model can be computed. The Lagrange interpolating polynomial is built at each frequency and the statistical quantities are directly calculated by numerical integration. The coefficient of variation can be computed for each value of ω in order to give a global overview of the sensitivity to the output uncertainty.

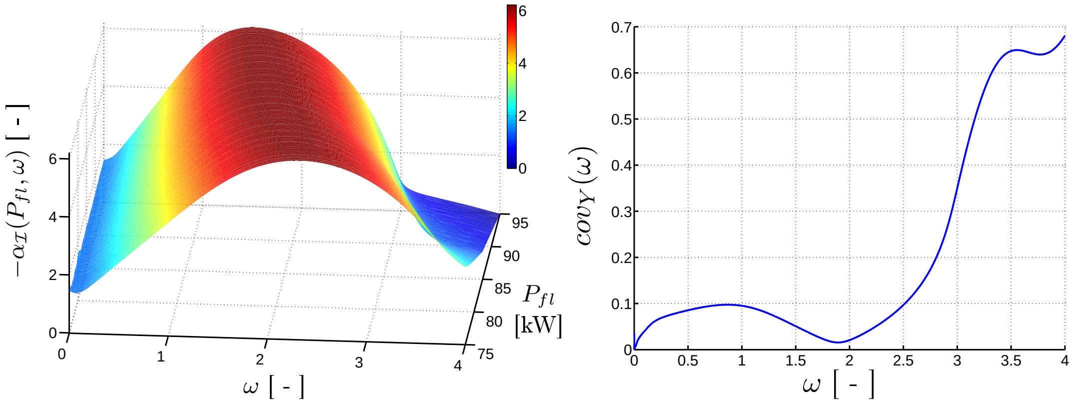

(a) Surface plot

(b) Coefficient of variation

Figure 4.15: (a) Surface plot of the growth rate as a function of the two variables P_{fl} and ω and (b) coefficient of variation as a function of ω.

The result obtained for the coefficient of variation is shown in Fig. 4.15b. This methodology of computing the coefficient of variation can be seen as a reduction of the dimensionality of the problem. The information on the uncertainty of the electric power is now contained in a single variable that depends only on ω. Of course, by doing this we loose the information provided by the whole output pdf but we can have and general idea on the evolution of the output pdf by only looking at the coefficient of variation. From Fig. 4.15b, we see that $cov_Y(\omega)$ is reaching a minimum value at $\omega = 1.893$ where $cov_Y(1.893) =$. This means that the growth rate of the instability wave with frequency $\omega = 1.893$ can be quite well predicted, no matter the uncertainty of the input electric power. For high frequency instability waves, the growth rate is very sensible to the input uncertainty and the prediction on the value of $\alpha_{\mathcal{I}}$ will be quite bad in this range.

Results for the most amplified frequency

The surrogate model for the most amplified frequency $\arg\max_{\omega}(\alpha_{\mathcal{I}})$ is addresses here. Considering once again Fig. 4.15, the most amplified frequency is not the same at each value of the electic power. Therefore, at each value of P_{fl} defined at the CC abscissa, the argument of the maximum growth rate is computed (Fig. 4.16). The values obtained for ω are then interpolated using the lagrange interpolating polynomial for the surrogate model.

The convergence of this surrogate model with increasing abscissa must also be proved. These results are not represented here as they lead to the same conclusions. The surrogate model for the most amplified frequency ω and the output pdf using Monte-Carlo sampling are represented in Fig. 4.17. Note that for the output pdf in Fig. 4.17b, it is again possible to compute the analytical pdf and compare it with the result of the Monte-Carlo sampling.

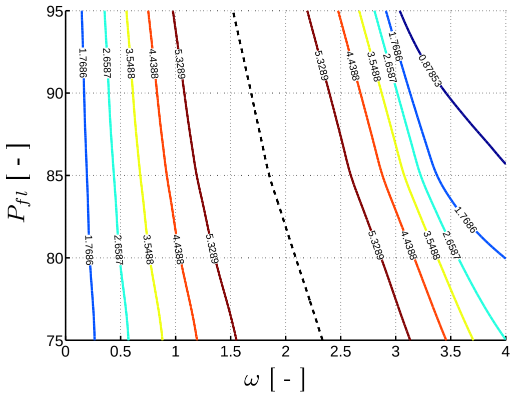

Figure 4.16: Isolines and most amplified frequency line for the growth rate. The growth rate is in dimensionless form. The isolines are represented by continuous lines and the most amplified frequency line is represented by a discontinuous line.

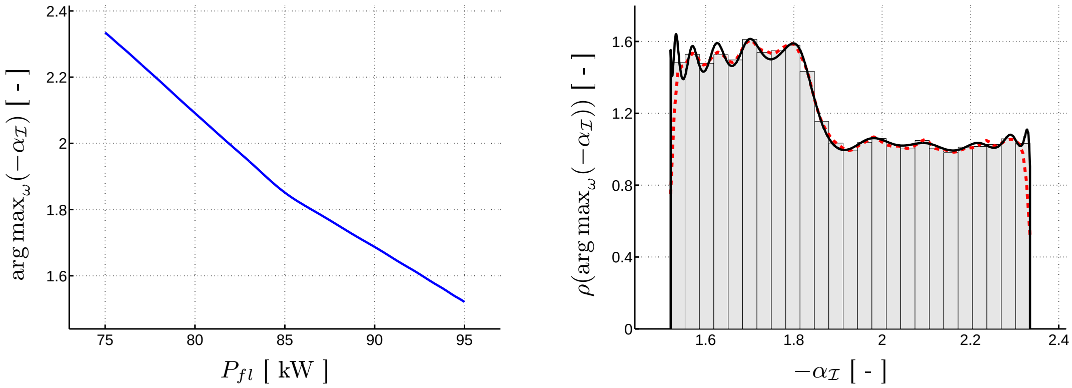

(a) Surrogate model

(b) Output pdf

Figure 4.17: Propagation of the input uncertainty for the most amplified frequency (a) through the surrogate model with 30 collocation points at CC abscissa. (b): Output PDF. — : Analytical pdf, – – : estimated pdf.

In this case, the surrogate model is a strictly decreasing function and it seems to follow a linear relation with two slopes. The output pdf has thus two regions of equiprobable density. Note that the range of value in which $-\alpha_{\mathcal{I}}$ is defined is much smaller than in the analysis at $\omega = 0.7$. This is because the most amplified frequency for each value of P_{fl} lies in the range where the coefficient of variation was found to be smaller.

4.2.5 Numerical results: use of accurate CFD profiles

In this section, new CFD profiles are computed for improving accuracy and validating the results previously obtained with the approximated profiles. These new computations are presented in Appendix C. The previous analysis used interpolation between existing models and thus some additional errors were introduced. This was however useful to investigate the convergence of the model and its main features. Clenshaw-Curtis abscissa, distributed on the domain of the input uncertainty for the level l, are again used for the computation of the CFD profiles. The nested level chosen here is $l = 4$, and 17 new CFD profiles are computed. This value for l is motivated by the satisfying convergence of the previous model reached for this number of points. On the other hand, $l = 5$ would require a great number of simulations, which is computationally expensive. However, nothing can be said for now on the convergence of the model when accurate profile are used, but we hope that the results will remain closed to the previous ones. The possibility of studying the convergence on the nested levels of the Clenshaw-Curtis abscissa is one of the main motivation of using them. Moreover, going to the next level $l = 5$ would required only a few numbers of simulations, which would not be the case with the Gauss-Legendre nodes.

Convergence analysis

Convergence analysis can be made here again but only on the nested levels. The CC abscissa and the corresponding simulations have been computed for $n = 17$ nodes and the analysis can not be made on the successive iterations. Thanks to the property of the CC abscissa of being nested, $n = 17$ corresponds to the fourth level (see Fig. 4.10a) and lower levels are composed by exactly the same nodes. Therefore, convergence can be verified using the fourth first levels of the CC nodes. The sequence computed for analysing convergence is exactly the same as in Eq. 4.22, except that the difference computed is now between two adjacent levels. This sequence is denote S_l and the convergence plot for the four first levels is given in Fig. 4.18.

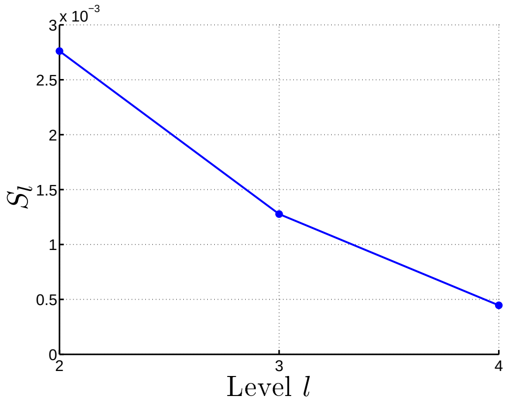

Figure 4.18: Convergence of the sequence S_l at $\omega = 0.7$ using accurate profiles obtained from numerical simulations at 17 Clenshaw-Curtis nodes fo the electric power.

The surrogate models obtained at $l = 1$ and $l = 4$ and $\omega = 0.7$ are represented in Fig. 4.19. Results look quite the same as before. The relation of the growth rate with the electric power is still close to a linear relation. In this case, oscillations are barely present in the model and the output pdf will be close to an equiprobable distribution like the input pdf. Note that now, at $P_{fl} = 85$ [kW], the value $-\alpha_{\mathcal{I}} = 3.5606$ is exactly recovered as now correct CFD profiles and the same fitting process are used. We can therefore compare directly the result obtained here with the ones from Sec. 4.1.

Coefficient of variation as a function of frequency

The input uncertainty is propagated through the surrogate models computed at each frequency and statistical descriptors can be obtained for the growth rate as a function of ω. The mean and the variance of the output pdf are directly computed by numerical integration for each value of ω. For the comparison with the previous case, the statistical descriptors at $\omega = 0.7$ are shown in Tab 4.2 below. The corresponding surrogate model

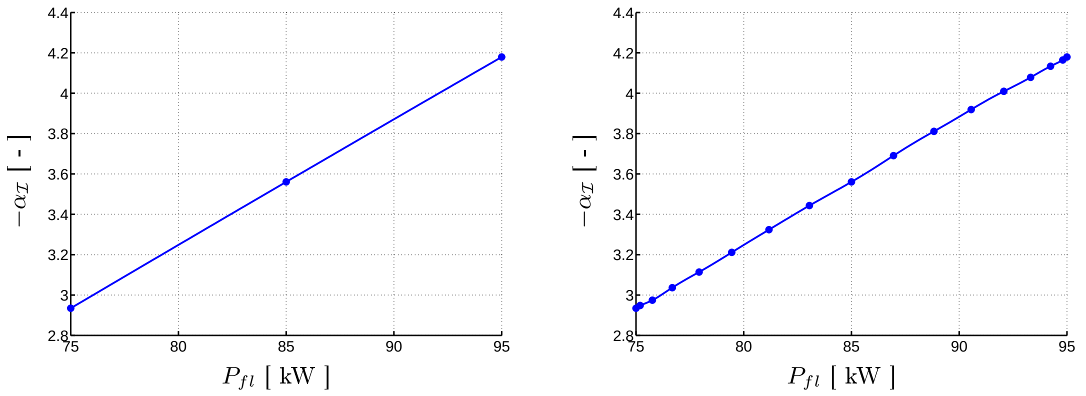

(a) $l = 1$, $n = 3$

(b) $l = 4$, $n = 17$

Figure 4.19: Surrogate model for the growth rate at $\omega = 0.7$ using accurate profiles from numerical simulations for different number of Clenshaw-Curtis abscissa

and output pdf is shown in Figs. 4.23a and 4.23f. Although the means are not exactly the same, standard deviations and coefficients of variation are of the same order.

	Approximate CFD profiles	Accurate CFD profiles
m_Y	3.617	3.563
σ_Y	0.3415	0.3637
cov_Y	0.094	0.102

Table 4.2: Comparison of the statistical descriptors estimated by numerical integration for the surrogate models built on approximated CFD profiles and surrogate models using accurate CFD profiles.

The result obtained for the coefficient of variation at each frequency is plotted in Fig. 4.20. The shape of the function is very similar to what was obtained previously. There is different sensibility of the output to the electric power in function of the frequency. We can observe approximatively three different regimes: a low frequency range located before $\omega = 1.5$, an intermediate frequency range ($\omega \in [1.52.5]$) where $cov_Y(w)$ reaches a minimum value, and a high frequency range for $\omega > 2.5$ where the coefficient of variation increases drastically.

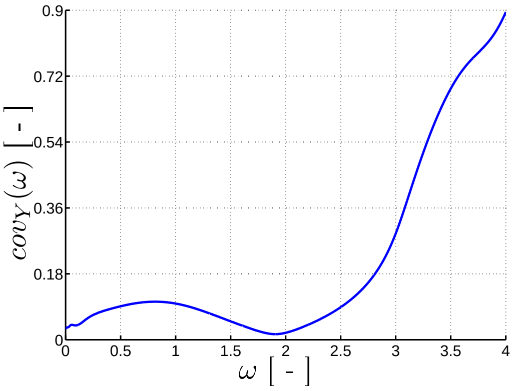

Figure 4.20: Coefficient of variation as a function of ω for the surogate model with 17 Clenshaw-Curtis nodes and accurate profiles.

The question from where the differences in the coefficient of variation come is now addressed In Fig. 4.21 are represented the surrogate models for three different values of ω, characteristic for the different regime defined above.

It can be observed that their behaviour can be very different depending on the frequency. Here the same scale is used in order to better emphasize their different range of values and explain the differences in the coefficient of variation. From this figure, it seems obvious that the variation in the *cov* is due to the range on value taken by de growth rate, and thus the standard deviation of the output pdf.

Indeed, for $\omega = 1.9$, where the minimum of $cov_Y(\omega)$ is located, the range of values for $-\alpha_{\mathcal{I}}$ is very restricted. The surrogate model at $\omega = 3.5$ gives a range of values $\alpha_{\mathcal{I}} \in [-0.31, -4.43]$, which is quite large compared to the other curves. At these frequencies however the mode tends to stabilize and might not be of interest. At low frequencies, the coefficient of variation remains in the same range, with a maximum near $\omega = 0.7$. At these frequencies, the surrogate model is close to a linear relation and the output pdf is equiprobably distributed on a restricted range. For $\omega = 0.7$, we found $\alpha_{\mathcal{I}} \in [2.93, 4.18]$.

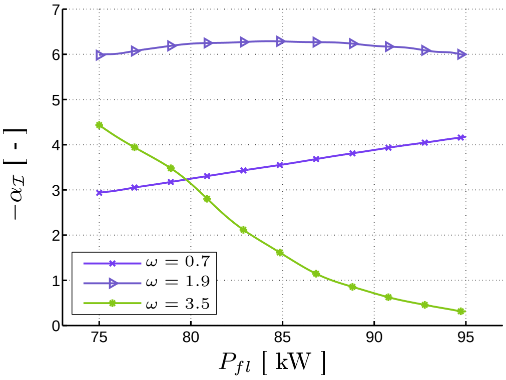

Figure 4.21: Comparison of the surrogate models obtained using accurate CFD profiles at different values of ω.

The shape and the output pdf of these three surrogate models can also be investigated. There are represented in Fig. 4.23 and as expected from the previous results, they are not the same. While at low frequencies the equiprobability density function is retrieved, it is not the case at higher frequencies.

Most amplified frequency

The numerical study of the stability of the plasma jet allows us to gain insight into the sensibility of the jet at the different frequencies of the instability. The coefficient of variation indicates that the sensibility of the growth rate can be different depending on the frequency. At high frequencies, the uncertainty on the input electric power induces a large uncertainty on the output growth rate while for low and moderate frequencies, the range of uncertainty was quite restricted.

Now the question of which uncertainty can be assigned to the frequency corresponding to the maximum growth rate when the electric power is uncertain is addressed. According to LST, the dominant instaiblity wave in the Plasmatron is the one with frequency that is the most amplified. Remind that this analysis is made only for the vortical mode, which is probably not the predominant mode.

As in the previous case where approximated profiles were used, the surrogate model is built by interpolating the frequency corresponding to the maximum growth rate at the CC abscissa. The surrogate model thus obtained and the propagation of the uncertainty through this model using Monte-Carlo sampling are represented in Fig. 4.22. The statistical descriptors obtained in this case are given in Tab. 4.3 and they are compared to the previous ones obtained using approximated profiles. Note that the QoI denoted by Y in the table is the quantity $\arg\max_{\omega}(-\alpha_I)$. From these results, it can be seen that the previous results obtained with approximated profiles gives almost the same results.

	Approximate CFD profiles	Accurate CFD profiles
m_Y	1.889	1.893
σ_Y	0.2358	0.23
cov_Y	0.12482	0.121

Table 4.3: Comparison of the statistical descriptors estimated by numerical integration for the surrogate models built of the most amplified frequency on approximated CFD profiles and surrogate models using accurate CFD profiles.

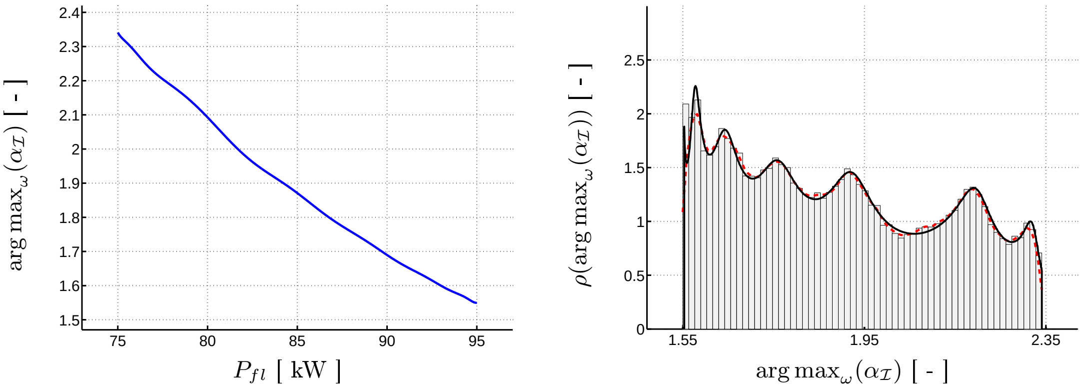

(a) Surrogate model

(b) Output pdf

Figure 4.22: Propagation of the input uncertainty for the most amplified adimensional frequency ω (a) through the surrogate model with 17 CC collocation points using accurate CFD profiles. (b): Outputpdf. — : Analytical PDFs, - - : estimated pdf.

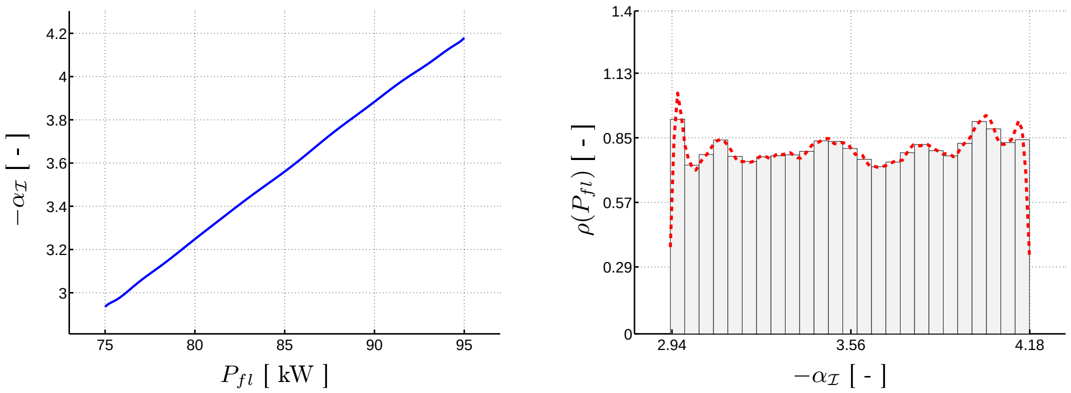

(a) Surrogate model ($\omega = 0.7$)

(b) Output pdf ($\omega = 0.7$)

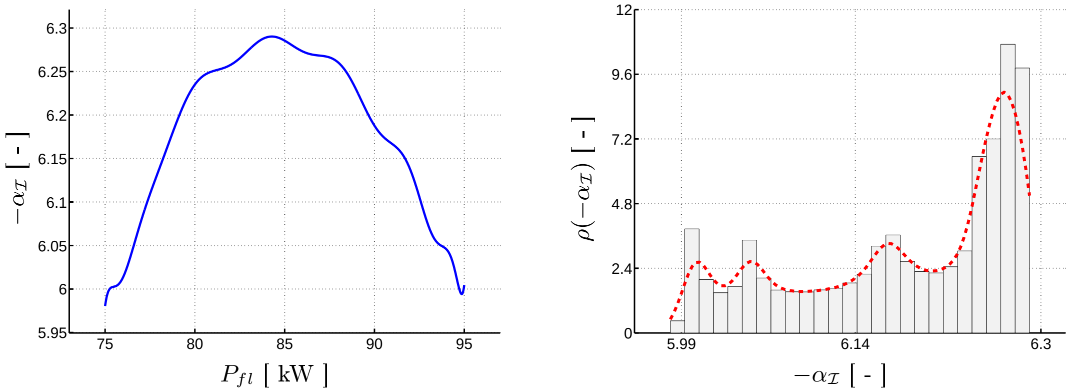

(c) Surrogate model ($\omega = 1.9060$)

(d) Output pdf ($\omega = 1.9060$)

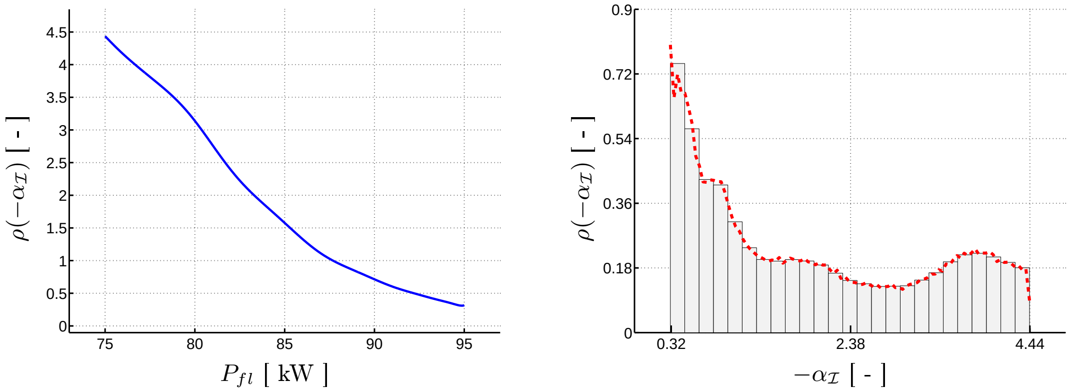

(e) Surrogate model ($\omega = 3.5$)

(f) Output pdf($\omega = 3.5$)

Figure 4.23: Propagation of the input uncertainty through the surrogate model (a) for the growth rate at different frequency ω. (b): Output pdf. – – : Estimated pdf's.

Link with dimensional frequency

The previous analyses were all made in terms of the adimensional angular frequency ω. However, the results in terms of dimensional frequency f ([Hz]) would be much more instructive. Recall that the relation that relates f to ω is $f = \omega w_{cl}/(2\pi R_{jet})$. In Sec. 4.1, the rescaling for the frequency was quite straightforward as any of these parameters were modified. However, in this case, the centerline velocity w_{cl} is also dependent on the electric power and the results in terms of f might be different.

A link between the adimensional frequency ω and the dimensional frequency f for the UQ analysis on the growth rate has not been made in this work. As the scaling is not the same for each values of P_{fl}, the function $-\alpha_{\mathcal{I}}(\omega)$ at the different values of P_{fl} after the dimensionalisation may not be defined on the same set of points (as we are dealing with numerical solutions). Thus, the interpolation for building the surrogate model is made more difficult. Moreover, the domain of frequencies where the new function $-\alpha_{\mathcal{I}}(P_{fl}, f)$ is defined changes from one curve to the other. This issue is represented in Figs. 4.24a and 4.24b for three different values of P_{fl}. A solution would be to define an analytical profile for the growth rate before the dimensionalisation. Interpolating data might be an other solution.

This has not been made in this work and it should be investigated as well in order to obtain a correct interpretation of the previous analyses in terms of the dimensional frequency. Nevertheless, by looking more closely at Fig. 4.24a it can be reasonably assumed that for low frequencies, the coefficient of variation, and thus the uncertainty on the growth rate will be lower than at high frequencies. Near $f = 300$ [Hz], the values seem to be more "packed" and consequently the coefficient of variation will be minimum in this range of frequencies, which corresponds to the range of the maximum growth rate.

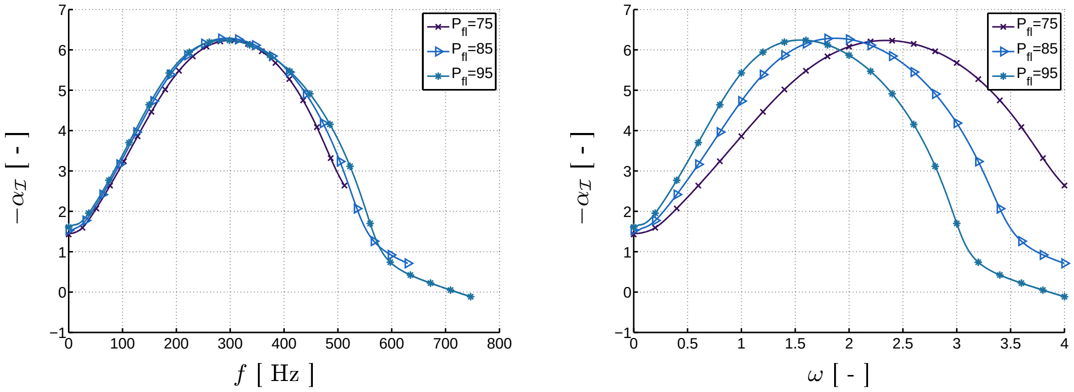

(a) Dimensional frequency

(b) Adimensional angular frequency

Figure 4.24: Growth rate in function of (a) the dimensional frequency and (b) the angular dimensionless frequency for different electric power values.

However, it has been possible to investigate the surrogate model for the most amplified dimensional frequency, as in this case the values at different frequencies are interpolated and are always defined (numerically speaking). Indeed, the most amplified dimensional frequency can be directly computed by finding the value of the most amplified ω and rescaling it. Then, the interpolation is made between these frequencies at the values of P_{fl} given by the CC abscissa. The result for the surrogate model and the output pdf is represented in Fig. 4.25. Note that in this case, the surrogate model is completely different. It is not possible to compute the analytical pdf and only Monte-Carlo sampling is possible to have an idea on the shape of the output pdf. The oscillations and the zero derivatives in the surrogate model induced strong variations in the output pdf, meaning that talking in terms of mean value and standard deviation might not be relevant.

This last analysis with the dimensional frequency allows a link with the numerical

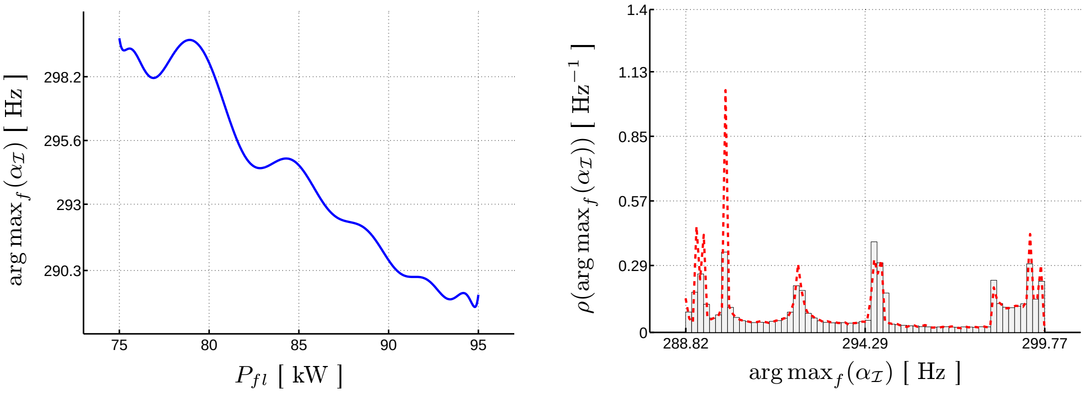

(a) Surrogate model

(b) Output pdf

Figure 4.25: Propagation of the input uncertainty for the most amplified dimensional frequency (a) through the surrogate model with 17 CC collocation points using accurate CFD profiles. (b): Output pdf. – – : Estimated pdf.

simulations to be established. A user who wants to simulate numerically the instability of the jet will be faced with the problem of choosing a value for the efficiency of the Plasmatron. The results obtained previously indicate that, assuming that the vortical mode is the dominant instability[4], the user will predict that the most amplify frequency of the jet will lie within a frequency range $[288.81, 299.77]$ with mean 294.19 [Hz]. Thus, when he will reproduce experimentally the numerical results obtained previously, he can expect that the frequency of the observed instability will be in the range obtained numerically. Thus, the uncertainty quantification study made in this section gives a range of values where the experimental results can be expected to lie and assigns to it a probability distribution. This can be of practical interest if we want only to have an approximate range of possible values of the instability frequency (as well as the associate wavelength) without any experimental realization.

Of course in the Plasmatron, the coupling between the generator and the plasma does not vary, if the operating conditions are kept constant, and the user will ideally obtain the same measurement of the instability each time. The uncertainty studied here is only on the numerical investigation of the stability of the plasma jet. However, if in the near future, the efficiency could be reduced or known exactly, these results must be updated accordingly. This illustrates the difference between *epistemic* uncertainty, which is due to a *lack of knowledge*, with the *aleatory* uncertainty, which consider the uncertain input as having an aleatory behaviour.

However, as already stated, this analysis can be linked to an uncertainty on the measurements of the electric power of the generator P_{fl}. Only in this case the experimentalist will observe this kind of variation from one experiment to the other and the uncertainty can be considered as aleatory, as the user will observe different results with the same set of input conditions.

---

[4] Although this is not likely to be the case as the acoustic modes are more unstable

4.3 Sensitivity Analysis with Input Uncertainty

We consider again the different models described in Sec. 4.1 and now we assume that the input P_{fl} is uncertain. The aim of this section is to investigate the variation of the first vortical mode when flow properties are modified and when the electric power is not exactly known. We are applying here the methodology developed in the previous section to the different models introduced at the beginning of the chapter for the sensitivity analysis.

We can compute for each set of parameters a surrogate model. This surrogate model can be considered here to be a function of three parameters: P_{fl}, ω and $\hat{\varphi}$. The last variable $\hat{\varphi}$ can be composed of any set of parameters as described in Sec. 4.1. For simplicity, we investigate here only $\hat{\varphi} = \{\hat{\chi}, \widehat{\mathrm{CPG}}, \widehat{\mathrm{CRG}}\}$. Of course, the surrogate model is a continuous function of P_{fl}, ω in $[75, 95] \times [0, 4]$ and a discrete function of $\hat{\varphi}$. It will be denoted here $s^{\hat{\varphi}}(x, \omega)$ where x stands for the electric power for simplicity of notation.

4.3.1 Growth rate and dependence on frequency

In order to follow the same steps as in Sec. 4.1, we first consider the differences in the growth rate at each frequencies for the different model parameters compared to the accurate $\widehat{\mathrm{CRG}}$ model.

In the previous sensitivity analysis in Sec. 4.1, at a given frequency, we gauged the difference between two models in terms of the difference between the values of the growth factor predicted by these two models at the nominal power. By contrast, in the present sensitivity analysis under uncertainty, in order to take into account the uncertainty in the power, at a given frequency, we must gauge the difference between two models in terms of the difference between the values of the growth factor predicted by these two models over a range of values of the power. Thus, at a given frequency, we consider the two models as functions that transform each value of the power into corresponding values for the growth factor, and we gauge the difference between these two models by the $\mathbb{L}_2$ norm between these functions. The following integration is considered here:

$$I^{\hat{\varphi}}(\omega) = \int ||s^{\widehat{\mathrm{CRG}}}(x, \omega) - s^{\hat{\varphi}}(x, \omega)||^2 \rho(x) dx. \tag{4.29}$$

Once again, as $\rho(x)$ is the equiprobable density function, we can use the Gauss-Legendre quadrature rule for the numerical integration. The integral is therefore

$$I^{\hat{\varphi}}(\omega) \approx \sum_{i=1}^{n_{GL}} ||s^{\widehat{\mathrm{CRG}}}(x_i, \omega) - s^{\hat{\varphi}}(x_i, \omega)||^2 w_j^{n_{GL}}, \tag{4.30}$$

where n_{GL} denotes the order of integration of the quadrature rule and $w_j^{n_{GL}}$ the weight j of order n_{GL}. The results for the numerical integration for the different flow models are given in Fig. 4.26.

As we are considering a norm here, it is not possible to say wheter the parameter has a stabilizing or a destabilizing influence. This figure has to be compared with the previous one obtained in Fig. 4.4

4.3.2 Most amplified frequency

One Surrogate model can be defined for the most amplified frequency of each model. The same integral as before is computed, except that now we are integrating the surrogate model for the most amplified frequency. The results obtained, for the dimensional and adimensional frequency, are shown in Fig. 4.27. It can be noticed once again that the influence of the flow properties is globally the same as in the first deterministic sensitivity analysis. The surrogate model for the

The surrogate models for the most amplified frequency f for the three models $\widehat{\mathrm{CPG}}$, $\widehat{\mathrm{CRG}}$, and $\hat{\zeta}$ are represented in Fig. 4.28. The quantity that was computed in Fig. 4.27b was in fact the norm 2 of the difference between one model and the $\widehat{\mathrm{CRG}}$. Looking at the surrogate models, it can be seen that, although the modification of the parameters influences the range of frequency, the global behaviour of the dependence of the most amplified frequency with the electric power is unchanged is unchanged.

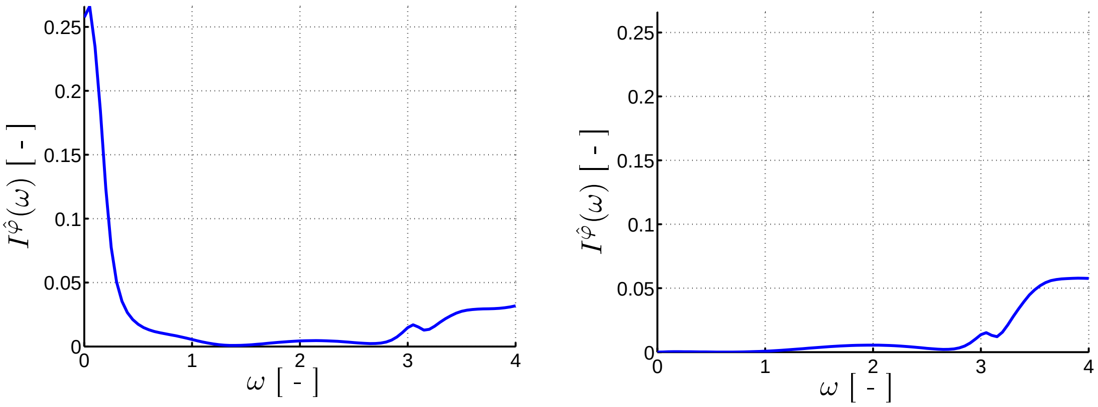

(a) $\hat{\varphi} = \widehat{\mathrm{CPG}}$

(b) $\hat{\varphi} = \hat{\mu}$

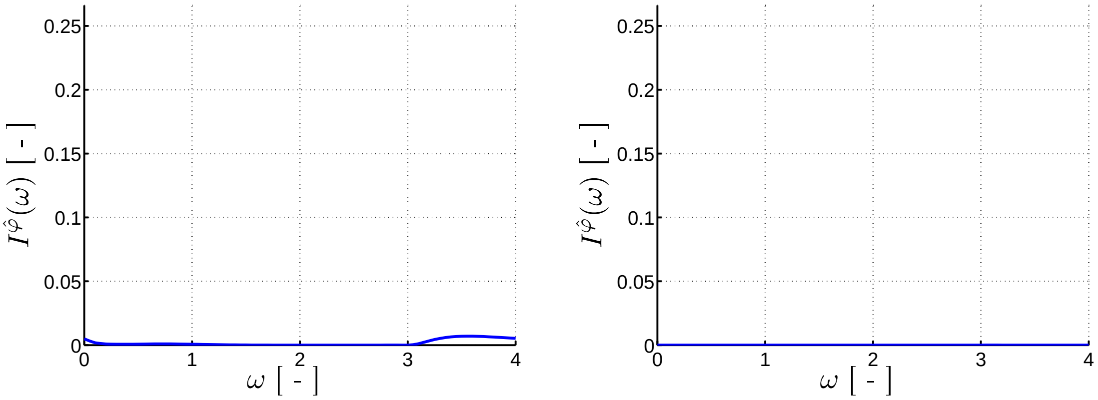

(c) $\hat{\varphi} = \hat{k}$

(d) $\hat{\varphi} = \hat{\lambda}$

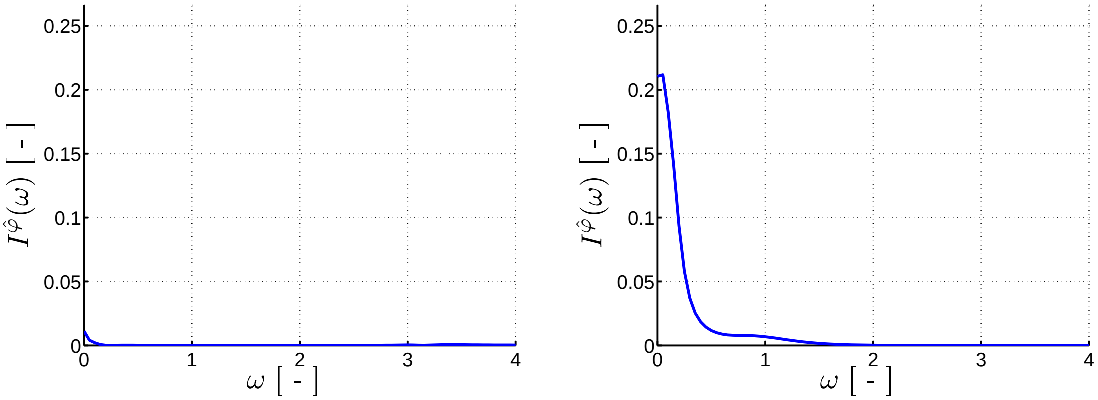

(e) $\hat{\varphi} = \hat{h}$

(f) $\hat{\varphi} = \hat{\zeta}$

Figure 4.26: Distance between the growth rate of the vortical mode of the CRG model and the different models involving simplified laws in temperature for the transport and thermodynamic properties in function of the adimensional angular frequency ω with uncertain input electric power.

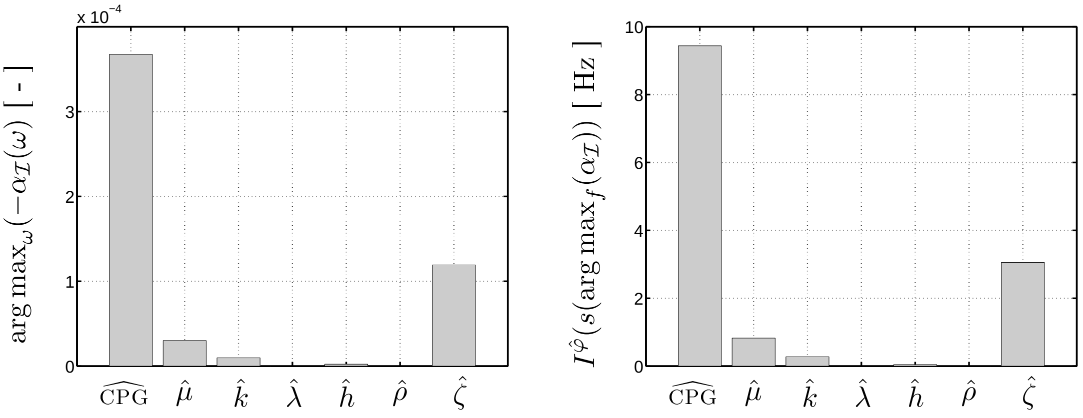

(a) Most amplified angular frequency

(b) Most amplified frequency

Figure 4.27: Influence of the model of transport and thermodynamic properties on the most amplified frequency compared to the accurate CRG model.

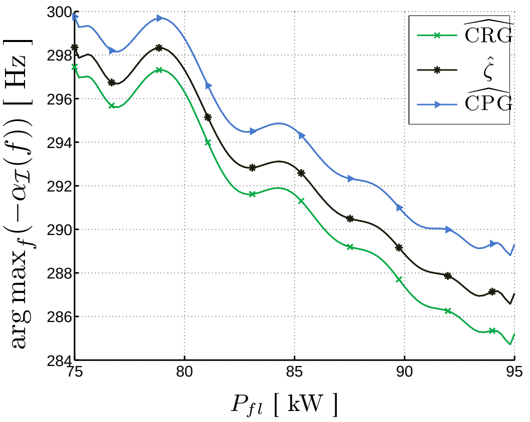

Figure 4.28: Comparison of the surrogate models obtained using accurate CFD profiles at different values of ω.

4.4 Summary of the Chapter

The previous analysis indicates that that all parameters of the model do not have the same influence on the instability of the vortical mode when the LTE hypothesis is introduced. Thermal conductivity k, dynamic viscosity μ and compressibility factor ζ are the parameters that most affect the instability. Total enthalpy of the gas h has only a weak influence on the vortical mode. But it appears that for acoustics mode, h and ζ are playing an important role Other parameters as the second viscosity coefficient λ or density ρ does not have any impact. The sensitivity analysis with the introduction of the uncertain electric power provides the same results concerning the relative importance of the different parameters.

A methodology for the uncertainty quantification for the stability of the plasma jet was proposed. A non-intrusive method was investigated here as many tools already developed and validated at VKI (CooLFluiD, Mutation, VESTA) come into play. The uncertainty on the plasma electric power was propagated through a surrogate model built on the interpolation of the solution at Clenshaw-Curtis abscissa. Gauss-Legendre points have also been discussed. This methodology remains general and could be applied to other scalar input quantities and other probability density function could also be investigated. In particular, uncertainty on the measurement of the electric power of the generator can be studied as well.

The variations of the growth rate and the most amplified frequency between the reference (correct) model and the simplified models are however much more dependent of the electric power. The consequence of this is that when running a CFD simulation, the experimenter has a greater interest in determining more precisely the efficiency η of the Plasmatron, corresponding to its particular case, in order to reduce the range of uncertainty on the electric power transmitted to the flow. This stronger dependence on the electric power was expected as it is influencing directly the mean profile computed with CooLFluiD. When considering different models, the mean profile remains unchanged.

One should be careful with these considerations. This study does not suggest that the flow properties does not have to be determined accurately. As stated in the beginning, the mean flow have to be computed using the rigorous flow properties. Without this, CFD results would be completely inaccurate or wrong.

Chapter 5

Conclusion

5.1 Contribution of this Thesis

Sensitivity analysis in the nominal case

A methodology for sensitivity analysis was proposed. It was observed that the driving parameter for low frequency jet instabilities was the compressibility factor. This parameter contains all the chemistry of the high temperature jet, a term that was not present when a calorically perfect gas was assumed for the plasma jet. It was also observed that the viscosity μ was one of the driving parameter in the instability of the vortical mode at moderate frequencies. However, at these frequencies the compressibility factor was tending to zero and was not influencing the stability anymore.

The analysis was made also for the three first acoustic modes. The enthalpy h was showed to be the main driving parameter in this case, together with the compressibility factor ζ. This analysis was made however for a fixed frequency of the instability and nothing could be said about the influence of the frequency. The influence of the enthalpy was also showed to decrease when considering acoustic modes with higher radial number. In these cases, the two models (CPG and CRG) tends to the same results and there is no more parameter influencing the stability.

These results suggested that the main driving parameter of the instability was in some manner linked to the mechanism of formation of the particular mode. Vortical modes are linked to an instability in the shear layer, and therefore they should be strongly coupled to the viscosity. Acoustic mode are linked to waves reflecting back and forth inside the jet and therefore may be related to the enthalpy (which determines the equilibrium speed of sound). Several explanations for the different mode of instabilities in high-temperature jets exist, but there is no universal one at that time. This sensitivity analysis may be a starting point in understanding their behaviour by numerical investigation.

Uncertainty quantification

A methodology for the uncertainty quantification when the electric power is uncertain was developed. The results showed that the growth rate and the most amplified frequency were strongly dependent on the electric power. While the uncertainty on the most amplified frequency is high when expressed in adimensional form, the uncertainty is reduced when it is expressed in terms of dimensional unit. Thus, when numerical investigation of the instability of the vortical mode of the jet is computed, an uncertainty of 10 [Hz] is made on the most amplified frequency. This result is limited of course to an input electric power in the range range $[75, 85]$ [kW] with equiprobable density. The methodology could also be extended as well to other types of modes.

It appeared also that the dependence on the electric power was not the same at each frequencies. In particular, the uncertainty on the growth rate of the vortical mode is minimum for low and moderate adimensional frequencies ($\omega < 2.5$).

Sensitivity analysis with input uncertainty

The sensitivity analysis, together with the quantification of uncertainty on the input electric power using stochastic collocations, was finally investigated. It appeared once again that the main driving parameters influencing the growth rate $\alpha_{\mathcal{I}}$ was the viscosity μ and the factor of compressibility ζ. The thermal conductivity k has an influence only for high frequencies ω. The results for the growth can not be interpreted in terms of dimensional frequency.

The same results as in the first sensitivity analysis are obtained for the most amplified frequency f. Parameters μ, k and ζ are the main driving parameter. A stronger variation is however observed when viscosity is modified and ζ has the biggest influence. From these considerations, it seems that the input electric power does not modifies the relative importance of the parameter driving the instabilities of the jet, at least for the vortical mode. Moreover, when flow properties are changed, the global dependence on the input electric power was still the same, except for a change in the range of values. This suggested that the electric power and the flow properties influence the instability of the vortical mode of the plasma jet in an independent manner.

Note that the results of the sensitivity analysis are made only regarding the stability analysis. Flow properties were not modified for computing the numerical simulations, as it would lead to completely wrong results.

5.2 Future Recommendations

- **Extension of the UQ analysis to several inputs.** The study was made on a single uncertain input, but it can also be extended to multiple uncertain inputs. For example, one can consider that the pressure in the Plasmatron is know in a certain range due to measurement errors. The stochastic collocation model thus obtained would be a polynomial of two dimensions and the relative importance of the uncertainty of the different inputs can be quantified. Stochastic collocation method can however be difficult to generalize to higher dimensions (curse of dimensionality) and other methods based on sparse grid construction may be considered [17].

- **UQ analysis of the Mutation properties.** In a future framework of uncertainty quantification study, errors on the MUTATION properties could also be investigated. In this case, the input would be an uncertain function of temperature and/or pressure a bounds should be put on the properties. A similar methodology of stochastic collocation could be for example developed. However, the previous sensitivity analysis showed that the variation of properties produced only small changes in the growth rate. Therefore, it can be easily predicted that the small bounds on the MUTATION properties will produce only a barely noticeable variation in the instability. However, considering now the correct thermodynamic and transport properties, it could be possible to consider the whole computational model, i.e. with the CFD model COOLFLUID, that was not considered in this work, for propagating the uncertainty. Accounting for this, a more realistic sensitivity analysis on the thermodynamic and transport and properties could be made and the influence of the input properties could be quantified in a more realistic way. However, the high-dimensionality of the problem may be limiting for the using of simple stochastic collocation methods and high dimensional non-intrusive UQ methods should be investigated.

- **Generalization to other type of modes.** In the uncertainty quantification part, we limited ourselves to the analysis of the vortical mode. This is of course not necessarily general and it could be extended as well to other types of instability that can be found in the spectrum of the linearized operator and in particular to acoustic modes. In the view of generalizing this analysis to other types of mode, it should be useful to develop a methodology for identifying the different modes in the spectrum. For example, acoustic modes are close to the continuous spectrum, which makes their identification by a simple guess on their wavenumber value much more difficult. The different acoustic modes could be identified by the number of quasi-nodes and anti-nodes present in their pressure eigenfunction which is well defined. Mack's criterion, which is useful for differentiating vortical modes from the acoustic ones, was also not verified for low frequency acoustic modes studied in this work and this should be investigated as well. The influence of the adimensional frequency on acoustic modes has not been yet extensively investigated. By doing this, we could get a better comprehension of these kind of instabilities.

Bibliography

[1] G. N. Abramovich. *The Theory of Turbulent Jets.* The Massachusetts Institute of Technology, 1963.

[2] John D. Anderson. *Hypersonic and High Temperature Gas Dynamics.* AIAA, second edition, 2006.

[3] M. Arnst and J.-P. Ponthot. An Overview of Nonintrusive Characterization, Propagation and Sensitivity Analysis of Uncertainties in Computational Mechanics. *International Journal for Uncertainty Qantification*, 4 (5):387–421, 2014.

[4] I. Benito, M. Aleo, and Y. Babou. VKI Plasmatron Performances Investigations: I. Air Plasma Jet Time Dependant Behaviour. *3rd International Workshop on Radiation of High Temperature Gases in Atmospheric Entry*, ESA Paper SP-667, 2008.

[5] B. Bottin, M. Carbonaro, S. Paris, V. Vanderhaegen, A. Novelli, and D. Vennemann. Vki 1.2 MW Plasmatron Facility for the Thermal Testing of TPS Materials. *3^{rd} European Workshop on Thermal Protection Systems*, March 1998.

[6] B. Bottin, O. Chazot, M. Carbonaro, V. Van Der Haegen, and S. Paris. The VKI Plasmatron Characteristics and Performance. Technical report, Von Karman Inst. for Fluid Dynamics, Rhode-Saint-Genèse (Belgium), 2000.

[7] M. Chiatto. Numerical Study of Plasma Jets by Means of Linear Stability Theory. Master's thesis, Von Karman Inst. for Fluid Dynamics, Rhode-Saint-Genèse (Belgium), June 2014.

[8] A. Cipullo, B. Helber, F. Panerai, L. Zeni, and O. Chazot. Investigation of Freestream Plasma Flow Produced by Inductively Coupled Plasma Wind Tunnel. *Journal of Thermophysics and Heat Transfer*, Vol. 28, No. 3, July - September 2014.

[9] A. Dorsa. Energy Balance for Plasmatron Facility. Technical report, Von Karman Inst. for Fluid Dynamics, Rhode-Saint-Genèse (Belgium), 2015.

[10] G. Emanuel. Bulk Viscosity of a Dilute Polyatomic Gas. *Phy. Fluids A*, Vol. 2, No. 12, December 1990.

[11] A. Ferrari, E. Trussoni, and L. Zaninetti. Magnetohydrodynamic Kelvin-Helmoholtz Iinstabilities Astrophysics - II. Cylindrical Boundary-Layer in Vortex Sheet Approximation. *Monthly Notices of the Royal Astronomical Society*, Vol. 169, pp. 1051-1066, 1981.

[12] F. Garcìa Rubio. Numerical Study of Plasma Jets Unsteadiness for Re-entry Simulation in Ground Based Facilities. Master's thesis, Von Karman Inst. for Fluid Dynamics, Rhode-Saint-Genèse (Belgium), September 2013.

[13] A. E. Gill. Instabilities of "Top-Hat" Jets and Wakes in Compressible Fluids. *Phys. of Fluids*, Vol. 8, pp. 1428-1430, 1965.

[14] V. Giovangigli. *Multicomponent Flow Modeling.* Birkhäuser, Boston, 1999.

[15] G. Golub and G. Meurant. *Matrices, Moments and Quadrature with Applications.* Princeton University Press, 2010.

[16] K. Groot. Error Free Derivation of Parabolized Stability Equations. Technical report, Von Karman Inst. for Fluid Dynamics, Rhode-Saint-Genèse (Belgium), 2013.

[17] G. Iaccarino. Uncertainty Quantification in Computational Science. In *Uncertainty Quantification in Computational Fluid Dynamics*, STO-AVT-VKI Lecture Series 2013/14 - AVT 235, Von Karman Inst. for Fluid Dynamics, Rhode-Saint-Genèse (Belgium), September 2014.

[18] A. F. Kolesnikov. Conditions of Simulation of Stagnation Point Heat Transfer from a High-Enthalpy Flow. *Fluid Dyn., No. 28 (1), 131-137*, 1993.

[19] P. K. Kundu and I. M. Cohen. *Fluid Mechanics.* Elsevier, 4th edition edition, 2008.

[20] O.P. Le Maître and O.M. Knio. *Spectral Methods for Uncertainty Quantification.* Springer, 2010.

[21] David R. Lide, editor. CRC Handbook of Chemistry and Physics. CRC Press, Boca Raton, FL, 2005.

[22] K. H. Luo and N. D. Sandham. Instability of Vortical and Acoustic Modes in Supersonic Round Jets. *Phys. Fluids*, Vol. 9, No. 4, pp. 1003-1013, 1997.

[23] L. M. Mack. On the Inviscid Acoustic-Mode Instability of Supersonic Shear Flows. Part I: Two-Dimensional Waves. *Theor. Comput. Fluid Dyn.*, 2, 97, 1990.

[24] T. Magin. Physical Gas Dynamics. Lecture notes. Von Karman Institute for Fluid Dynamics, 2010-2011.

[25] T. Magin. *A Model for Inductive Plasma Wind Tunnels.* Phd thesis, Université Libre de Bruxelles & Von Karman Institute for Fluid Dynamics, Belgium, 2014.

[26] M.R. Malik and E.C. Anderson. Real Gas Effects on Hypersonic Boundary-Layer Stability. *Phy. Fluids A*, Vol. 3, No. 5, Pt. 1, May 1991.

[27] A. Michalke. Survey on Jet Instability Theory. *Prog. Aerospace Sci.*, Vol. 21, pp. 159-199, 1984.

[28] P. J. Morris. The Spatial Viscous Instability of Axisymmetric Jets. *J. Fluid Mech.*, Vol. 77, part 3, pp. 511-529, 1976.

[29] F. Pinna. *Numerical Study of Stability of Flows from Low to High Mach Number.* Phd thesis, Università La Sapienza di Roma & Von Karman Institute for Fluid Dynamics, Belgium, 2012.

[30] N. Rajaratnam. *Turbulent Jets.* Elsevier, 1976. University of Alberta, Canada.

[31] H. Schlichting. *Boundary-Layer Theory.* McGraw-Hill, 7th edition edition, 1979.

[32] P. J. Schmid and D. S. Henningson. *Stability and Transition in Shear Flows.* Springer, 2001. Applied Mathematical Sciences, volume 142.

[33] C. K. W. Tam and D. E. Burton. Sound Generated by Instability Waves of Supersonic Jets: Part 2, Axisymmetric Jets. *J. Fluid Mech.*, Vol. 138, 273, 1984.

[34] C. K. W. Tam and F.Q. Hu. On the Three Families of Instability Waves in High-Speed Jets. *J. Fluid Mech.*, Vol. 201, 447-483, 1989.

[35] W.G. Vincenti and C.H. Kruger. *Introduction to Physical Gas Dynamics.* Wiley, New York, 1965.

[36] D. Xiu. *Numerical Methods for Stochastic Computations.* Princeton University Press, 2010.

[37] A. Yaglom. *Hydrodynamic Instability and Transition to Turbulence.* Springer, 2012. Fluid Mechanics and its Applications, volume 100.

Appendix A

Integral Calculus in Kinetic Theory

A.1 Useful Integrals

- $\int_0^\infty \exp(-ax^2)dx = \frac{1}{2}\sqrt{\frac{\pi}{a}}$
- $\int_0^\infty x\exp(-ax^2)dx = \frac{1}{2a}$
- $\int_0^\infty x^2\exp(-ax^2)dx = \frac{1}{4a}\sqrt{\frac{\pi}{a}}$
- $\int_0^\infty x^3\exp(-ax^2)dx = \frac{1}{2a^2}$

A.2 Mean peculiar velocity

Maxwellian distribution velocity function is recall here for convenience

$$f_i^M = n_i\left(\frac{m_i}{2\pi k_B T}\right)^{3/2}\exp\left(\frac{-m_i(\boldsymbol{c_i}-\boldsymbol{u})^2}{2k_BT}\right) \tag{A.1}$$

Let us denote $C_i^2 = C_{i,1}^2 + C_{i,2}^2 + C_{i,3}^2,\ i \in S$, where the peculiar velocity reads as $\boldsymbol{C_i} = \boldsymbol{c_i} - \boldsymbol{u}$ which represents the velocity of a particle of species i in the hydrodynamic reference frame. Mean peculiar velocity is given by

$$\begin{aligned}\bar{C}_i &= \frac{1}{n_i}\int C_i f_i^M d\boldsymbol{c_i} \\ &= \left(\frac{m_i}{2\pi k_B T}\right)^{3/2}\int C_i \exp\left(\frac{-m_i\boldsymbol{C_i^2}}{2k_BT}\right)d\boldsymbol{C_i},\end{aligned} \tag{A.2}$$

where we used the notation for the integral

$$\int(\,\cdot\,)\ d\boldsymbol{C_i} = \int_{-\infty}^{\infty}\int_{-\infty}^{\infty}\int_{-\infty}^{\infty}(\,\cdot\,)\ dC_{i,1}dC_{i,2}dC_{i,3}. \tag{A.3}$$

Having $C_i = \sqrt{C_{i,1}^2 + C_{i,2}^2 + C_{i,3}^2}$, it will be more useful to express the integral in spherical coordinates. With the spherical coordinate system (C, θ, φ), the integral bounds are now expressed as

$$\int(\,\cdot\,)\ d\boldsymbol{C_i} = \int_0^\infty\int_0^\pi\int_0^{2\pi}(\,\cdot\,)\ C_i^2\sin\theta dC_i d\theta d\varphi \tag{A.4}$$

Rewriting Eq. (A.2) using Eq. (A.4), we have

$$\bar{C}_i = \left(\frac{m_i}{2\pi k_B T}\right)^{3/2}\int_0^\pi \sin\theta d\theta\int_0^{2\pi}d\varphi\int_0^\infty C_i^3\exp\left(\frac{-m_iC_i^2}{2k_BT}\right)dC_i \tag{A.5}$$

Taking advantage of the fourth useful integral from Sec. A.1, it follows directly that

$$\bar{C}_i = 4\pi \left(\frac{m_i}{2\pi k_B T} \right)^{3/2} \frac{1}{2} \left(\frac{2\, k_b T}{m_i} \right)^2 \tag{A.6}$$

$$= \left(\frac{8 k_B T}{\pi m_i} \right)^{1/2} \tag{A.7}$$

The mean of the magnitude of the species peculiar velocity can be related to the thermal agitation of the particles in the gas.

Appendix B

Linear Stability Equations

B.1 Linearized Gas State Equation

The total number of unknown in the linear stability problem is five, namely, $[u', v', w', p', T']$, while Navier-Stokes system yields four equations. Therefore, an additional equation is needed in order to close the system and the gas state equation is naturally included. The equation of state for the gas mixture in adimensional form reads

$$Hp = \rho T \zeta, \tag{B.1}$$

where p, ρ, T, ζ are the instantaneous flow variables and $H = Ec\, c_p / R_0$. Proceding to the linearization by introducting the small perturbations into the flow, we have

$$p = \bar{p} + p', \tag{B.2a}$$

$$\rho = \bar{\rho} + \rho', \tag{B.2b}$$

$$T = \bar{T} + T', \tag{B.2c}$$

$$\zeta = \bar{\zeta} + \zeta', \tag{B.2d}$$

where the above bar indicates the mean flow variables. Inserting these decompositions in Eq. (B.1), removing high order terms in small perturbations and noting that mean variables also verify the gas state law, we have

$$Hp' = \bar{\rho}\bar{T}\zeta' + \bar{\rho}\bar{\zeta}T' + \bar{T}\bar{\zeta}\rho'. \tag{B.3}$$

ζ can be assumed to be a function of the two thermodynamic variables $p = \bar{p} + p'$ and $T = \bar{T} + T'$. Developing ζ in a Taylor series around $\bar{p}$ and $\bar{T}$, we have

$$\zeta(\bar{p} + p', \bar{T} + T') = \zeta(\bar{p}, \bar{T}) + \frac{\partial \zeta(\bar{p}, \bar{T})}{\partial \bar{p}} + \frac{\partial \zeta(\bar{p}, \bar{T})}{\partial \bar{p}} + \mathcal{O}((p')^2, (T')^2), \tag{B.4}$$

where $\zeta(\bar{p}, \bar{T})$ is equivalent to $\bar{\zeta}$. It follows that $\zeta' = \zeta - \bar{\zeta}$ and thus

$$\zeta' = \frac{\partial \bar{\zeta}}{\partial \bar{p}} p' + \frac{\partial \bar{\zeta}}{\partial \bar{T}} T'. \tag{B.5}$$

This last equation is valid in the application of LST as terms of higher degree in p' and T' were already neglected. Subsituting Eq. (B.5) in Eq. (B.3) leads to

$$Hp' = \bar{\rho}\bar{T}\left(\frac{\partial \bar{\zeta}}{\partial \bar{p}} p' + \frac{\partial \bar{\zeta}}{\partial \bar{T}} T'\right) + \bar{\rho}\bar{\zeta}T' + \bar{T}\bar{\zeta}\rho'. \tag{B.6}$$

In order to have an expression for the density perturbation in terms of pressure and temperature perturbation, we can write equivalently

$$\rho' = \left(\frac{H}{\bar{T}\bar{\zeta}} - \frac{\bar{\rho}}{\bar{\zeta}}\frac{\partial \bar{\zeta}}{\partial \bar{p}}\right) p' - \left(\frac{\bar{\rho}}{\bar{T}} + \frac{\bar{\rho}}{\bar{\zeta}}\frac{\partial \bar{\zeta}}{\partial \bar{T}}\right) T'. \tag{B.7}$$

Substituting $H = (\bar{\rho}\bar{T}\bar{\zeta})/\bar{p}$ and rearranging terms,

$$\rho' = \left(\frac{\bar{\rho}}{\bar{p}}\left(1 - \frac{\bar{p}}{\bar{\zeta}}\frac{\partial\bar{\zeta}}{\partial\bar{p}}\right)\right)p' - \left(\frac{\bar{\rho}}{\bar{T}}\left(1 + \frac{\bar{T}}{\bar{\zeta}}\frac{\partial\bar{\zeta}}{\partial\bar{T}}\right)\right)T'. \tag{B.8}$$

Parameters F and G appear naturally in the linearized gas state equation as

$$\begin{aligned} F &= 1 - \frac{\bar{p}}{\bar{\zeta}}\frac{\partial\bar{\zeta}}{\partial\bar{p}} \\ &= 1 - \left.\frac{\partial\ln\bar{\zeta}}{\partial\ln\bar{p}}\right|_T, \end{aligned} \tag{B.9}$$

$$\begin{aligned} G &= 1 + \frac{\bar{T}}{\bar{\zeta}}\frac{\partial\bar{\zeta}}{\partial\bar{T}} \\ &= 1 + \left.\frac{\partial\ln\bar{\zeta}}{\partial\ln\bar{T}}\right|_p. \end{aligned} \tag{B.10}$$

Finally, density perturbation can be written as

$$\rho' = F\frac{\bar{\rho}}{\bar{p}}p' - G\frac{\bar{\rho}}{\bar{T}}T', \tag{B.11}$$

or equivalently, after inserting the modal decomposition

$$\widetilde{\rho} = F\frac{\bar{\rho}}{\bar{p}}\widetilde{p} - G\frac{\bar{\rho}}{\bar{T}}\widetilde{T}. \tag{B.12}$$

Appendix C

Numerical results of the ICP CooLFluiD simulations and their dependency on electric power

C.1 Mean Profiles

In Sec. 4.2.5, new CFD profiles are needed for better accuracy of the results of the uncertainty quantification. The new profiles are computed for the values of the electric power at the 17 Clenshaw-Curtis abscissa defined on the domain $P_{fl} \in [75, 95]$ [kW]. The ICP CooLFluiD solver is used for each numerical simulations.

We first look at the dependence of the centerline velocity and centerline temperature values on P_{fl} in Figs. C.1a and C.1b. It can be noticed that the temperature increase significantly with the electric power. At low electric power values, T_{cl} is near 7100 [K]. This value for the temperature corresponds to a low degree of ionization in the gas. By comparison, for $P_{fl} = 95$ [kW], $T_{cl} = 8248$ [kW], which corresponds to a greater degree of ionization of the gas. We can also note the linear relation between the mean streamwise centerline velocity with the electric power.

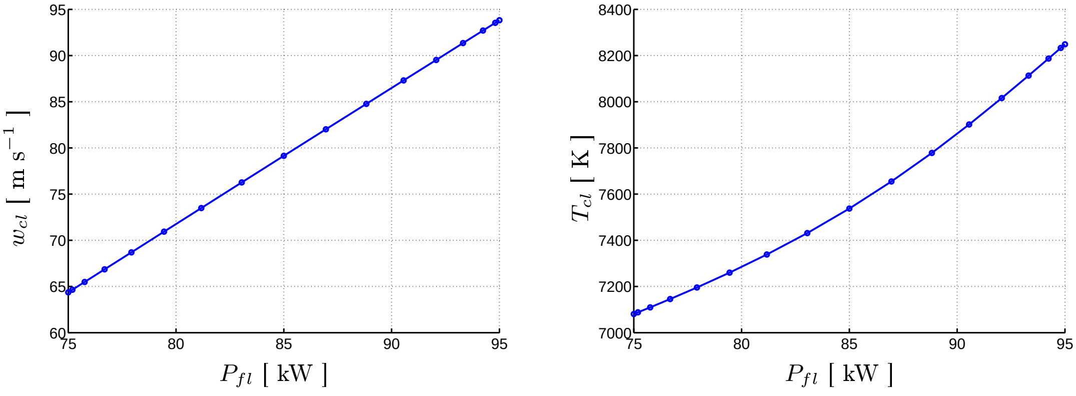

(a) Mean streamwise centerline velocity.

(b) Mean centerline temperature.

Figure C.1: Dependence of the mean streamwise centerline velocity and mean centerline temperature on the electric power P_{fl}.

Mean adimensional streamwise velocity and temperature profiles are represented in Figs. C.2a and C.3b. It can be noticed that the values of the electric power at endpoints are quite closed to each other. It was the first time that such closed conditions were used and there were no guarantee that the algorithm would converge towards distinguishable solutions. Results proved that the ICP solver was accurate enough to allow small ΔP_{fl}

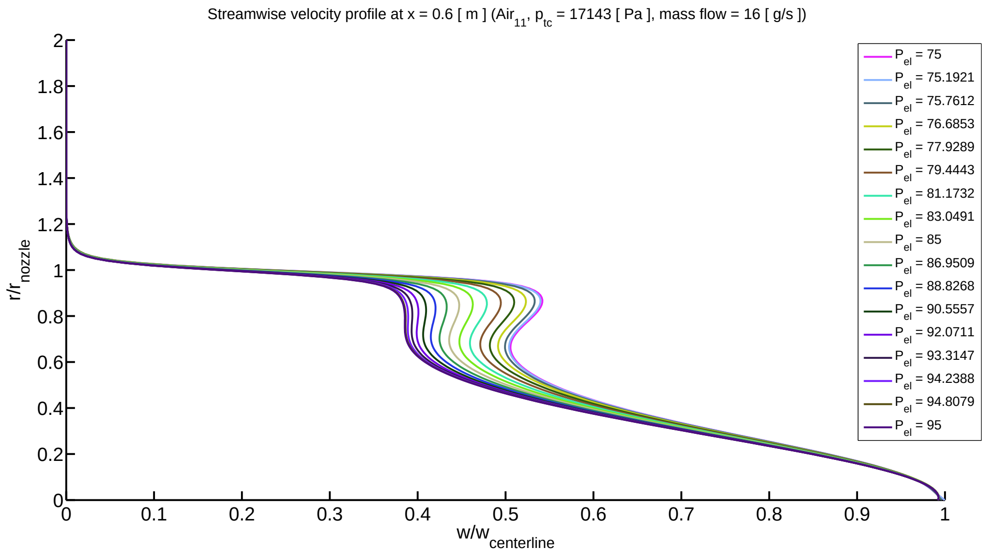

(a) Mean streamwise velocity

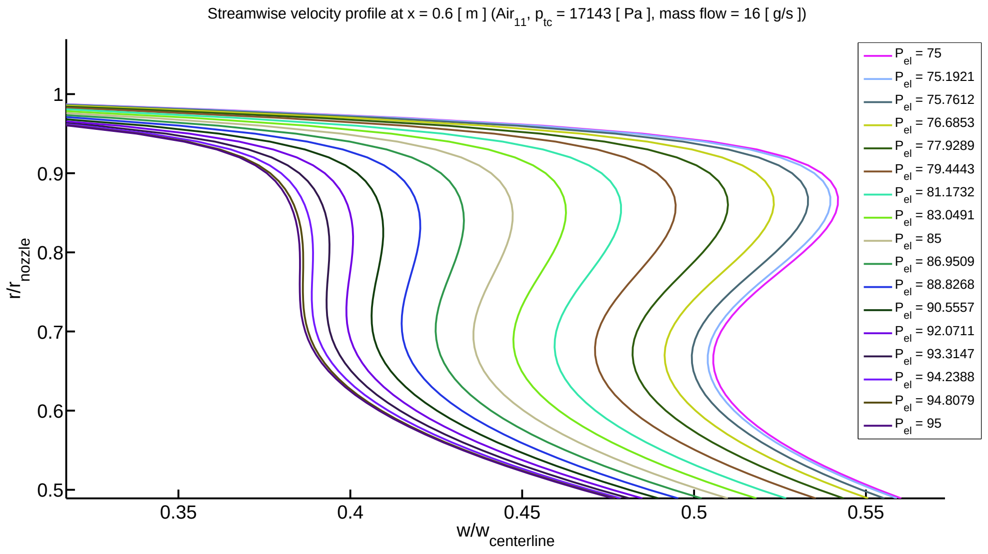

(b) Zoom on the bending zone

Figure C.2: Mean streamwise velocity profiles obtained from the ICP CooLFluiD solver at the 17 CC abscissa defined on $P_{fl} \in [75, 85]$ [kW]

between two profiles. In Figs. C.2a and C.3a, a zoom on the part where the adimensional profiles are the most dependent on P_{fl} is provided. As it can be observed, an increase in the electric power reduces the amplitude of the velocity in the bending zone (Fig. C.2b). Thus, a low value for the electric power will probably increase the instability of the flow due to the shape of the velocity profile.

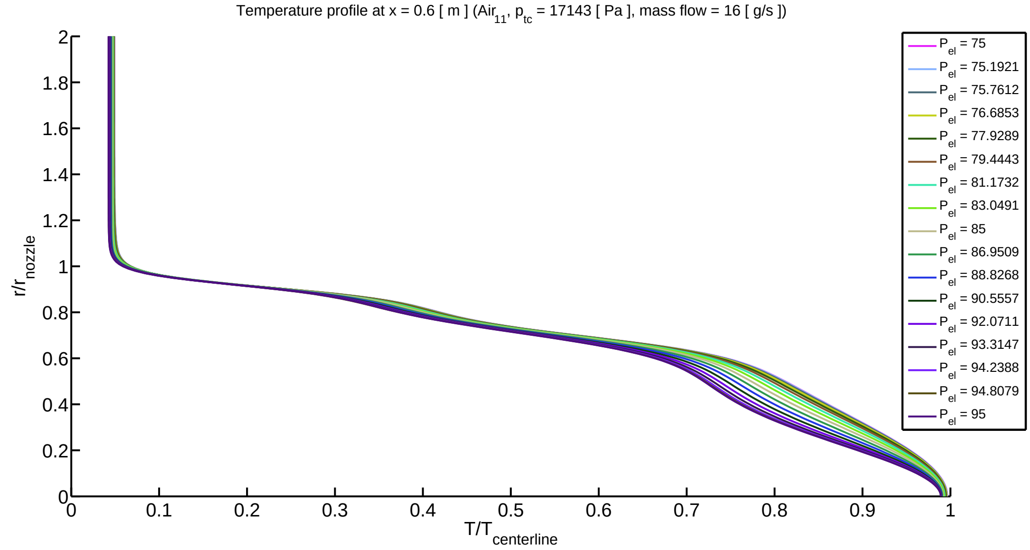

(a) Mean temperature

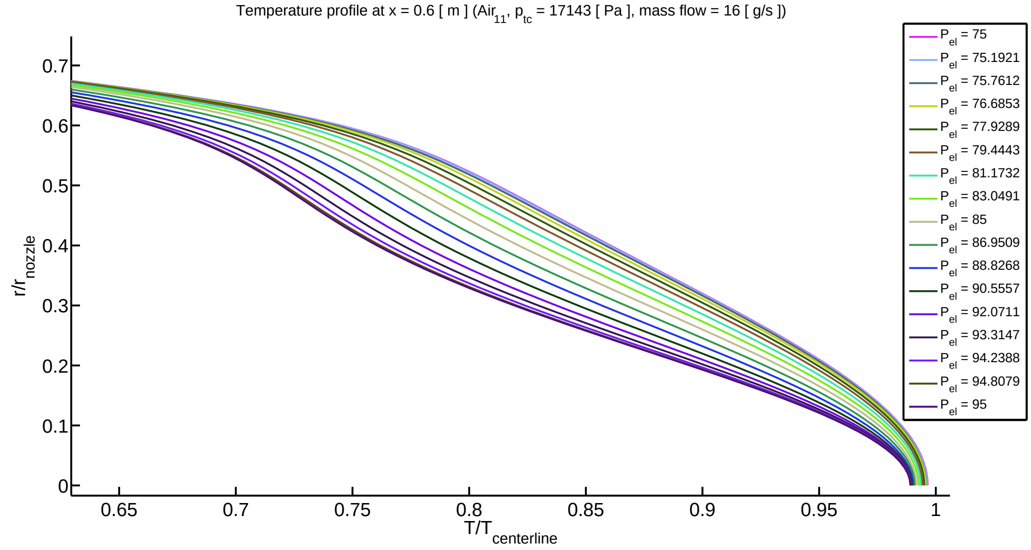

(b) Zoom on the near centerline region

Figure C.3: Mean temperature profiles obtained from the ICP CooLFluiD solver at the 17 CC abscissa defined on $P_{fl} \in [75, 85]$ [kW].